A Dissertation

Entitled

Application of the Space – Time Conservation Element and Solution Element Numerical Method to Flows in Fluid Films

by

Sorin Cioc

Submitted as partial fulfillment of the requirements for

the Doctor of Philosophy Degree in Engineering

Theo G. Keith Jr.

Adviser: Dr. Theo G. Keith, Jr.

Graduate School

The University of Toledo

August 2004

The University of Toledo

College of Engineering

_____

Date

I hereby recommend that the thesis prepared under my supervision by *Sorin Cioc* entitled *Application of the Space – Time Conservation Element and Solution Element Numerical Method to Flows in Fluid Films* be accepted in partial fulfillment of the requirements for the degree of *Doctor of Philosophy in Engineering*

_____

Dissertation Adviser: Theo G. Keith, Jr.

Recommendation concurred by:

_____

A. A. Afjeh

_____

T. T. Ng

Committee on

Final Examination

_____

D. P. Fleming

_____

F. Dimofte

_____

Dean, College of Engineering

Copyright © 2004

This document is copyrighted material. Under copyright law, no parts of this document may be reproduced without the expressed permission of the author.

An Abstract of

Application of the Space – Time Conservation Element and Solution Element Numerical Method to Flows in Fluid Films

by

Sorin Cioc

Submitted as partial fulfillment of the requirements for the Doctor of Philosophy Degree in Engineering

The University of Toledo

August 2004

This work, situated at the confluence between CFD and tribology, is the first application of a relatively new numerical method, the space-time conservation element and solution element (CE/SE) method, to flows in thin films.

The general features of the numerical method are highlighted, and also the concept of fluid film bearings is presented. The formulations of the governing equations and boundary conditions for four main cases are shown: 1-D and 2-D cavitated bearings using Elrod's formulation, hybrid gas bearings, and gas bearings including inertial effects.

The numerical formulations applied on both uniform and non-uniform grids are presented, with emphasis on the important features of the method when used to solve these specific problems, including the formulation of the boundary conditions.

Based on the described formulations, numerical codes have been developed. The results obtained are compared with experimental values, theoretical results, and numerical results obtained by using other algorithms. In the case of cavitated bearings, because the algorithm developed is capable of capturing potential discontinuities, the differences between the results obtained with the CE/SE method and with previous methods are significant when the position of the full film reformation point is not imposed through the supply system (boundary conditions). Important differences have also been noted in the case of gas bearings including inertia effects. Results demonstrate that the inclusion of inertial effects becomes necessary when the bearing speed is very high and/or the film clearance is large. Flow discontinuities are shown to occur in a manner similar to that of shock waves in supersonic flows.

Comparisons prove that the space-time CE/SE method, when contrasted to previous numerical algorithms, can successfully predict the pressure distribution within bearings, including cases with discontinuities in the lubricant film. Moreover, the method accomplishes this without any special treatment and without introducing distortion and/or excessive dissipation into the solution. The method is thus a strong candidate in applications that require more precise results, such as accurate, robust computation of the cavitation boundaries, as well as to solve transient problems. The method is also a perfect candidate in more complex problems, such as flows at very high speeds with inertia effects.

For my loving wife, Carmen, our dear son, Alexandru,

and parents, Zinca and Gheorghe

… again. More than ever.

Toledo, Ohio, 2004

Acknowledgments

I cannot fully express my gratitude to Dr. Theo G. Keith, Jr. He is an exceptional academic adviser, helpful and supportive, extraordinary leader, and ready anytime to devote his time and energy to help his students. In the same time he set an example for me by being just, open and honest, kind and gentle person, devoted and caring, constant source of wisdom and experience.

I thank the defense committee, Dr. Abdollah Afjeh, Dr. Terry Ng, Dr. David P. Fleming and Dr. Florin Dimofte for their time, energy and expertise brought to this thesis. Special thanks go to Dr. Dimofte for the support and invaluable advice. His experience and proficiency have been continuous source of knowledge during my research.

My gratitude also goes to Dr. Sin-Chung Chang and his workgroup at the NASA Glenn Research Center in Cleveland, Ohio, for providing the foundation, namely the space-time CE/SE numerical method, upon which this thesis is built. Their rigorousness and ingenuity are truly exceptional.

I thank the department of Mechanical, Industrial and Manufacturing Engineering, the Chairman, faculty, and staff for giving me this opportunity and providing financial support during my study.

Sorin Cioc

Table of Contents

Abstract	iv
Dedication	vi
Acknowledgements	vii
Table of Contents	viii
List of Tables	xi
List of Figures	xii
Nomenclature	xviii
Chapter 1 – Introduction, Motivation	1
Chapter 2 – Fluid Film Bearings and the Reynolds Equation	7
2. 1. The Reynolds equation	7
2. 2. Boundary conditions	17
2. 3. Cavitation in liquid-lubricated bearings	19
Chapter 3 – Application of the CE/SE Method to Cavitated Bearings	27
3. 1. Introduction: the CE/SE method	27
3. 2. One-Dimensional Problems	31

3. 2. 1. Equations 32

3. 2. 2. Uniform grid 34

3. 2. 3. Non-uniform grid 43

3. 2. 4. Applications involving slider bearings 50

3. 2. 5. Applications for journal bearings 59

3. 2. 6. Discontinuities at the fluid film reformation 66

3. 3. Two-dimensional problems 71

3. 3. 1. Numerical formulation 71

3. 3. 2. Applications for circular bearings 88

3. 3. 3. Applications for wave bearings 95

Chapter 4 – Application of the CE/SE Method to Pressurized Gas Bearings 113

4. 1. Introduction 113

4. 2. Equations 114

4. 3. Numerical formulation 115

4. 4. Applications 124

Chapter 5 – Inertial Effects in Gas Bearings 133

5. 1. Introduction 133

5. 2. Governing Equations 135

5. 3. Numerical formulation 139

5. 4. Applications 143

Chapter 6 – Conclusions 157

References 162

List of Tables

Table 3. 1 – Physical conditions for slider bearings 51

Table 3. 2 – Physical conditions for a grooved journal bearing 61

Table 3. 3 – Physical conditions for circular journal bearing 89

Table 3. 4 – Physical conditions for a wave bearing 99

Table 3. 5 – Physical Conditions for a Misaligned Wave Bearing 103

Table 4. 1 – Comparison between calculated data with CE/SE method and with finite difference method 126

Table 4. 2 – Pressurized gas bearing geometry and working conditions 128

List of Figures

Fig. 2. 1 – Coordinate system for two solid surfaces separated by a thin fluid film 7

Fig. 2. 2 – Control volume 13

Fig. 2. 3 – Couette flow in *x* direction 13

Fig. 2. 4 – Poiseuille flow in *x* direction 14

Fig. 2. 5 – Cavitation boundary 21

Fig. 3. 1 – Uniform space-time mesh 33

Fig. 3. 2 – Non-uniform space-time mesh 45

Fig. 3. 3 – Parabolic slider bearing configurations 51

Fig. 3. 4 – Conservation elements for the boundary condition at the exit 53

Fig. 3. 5 – Pressure distribution in a parabolic slider with flooded inlet 55

Fig. 3. 6 – Fractional film content distribution in a parabolic slider with flooded inlet 55

Fig. 3. 7 – Pressure distribution in a parabolic slider with starved inlet 57

Fig. 3. 8 – Fractional film content distribution in a parabolic slider with starved inlet 57

Fig. 3. 9 – Pressure distribution in a double parabolic slider with flooded inlet 59

Fig. 3. 10 – Journal bearing geometry 60

Fig. 3. 11 – Fractional film content distribution in a journal bearing with one groove 63

Fig. 3. 12 – Pressure distribution in a journal bearing with one groove 63

Fig. 3. 13 – Pressure distribution in a journal bearing without grooves 64

Fig. 3. 14 – Fractional film content in a journal bearing with two grooves 65

Fig. 3. 15 – Pressure distribution in a journal bearing with two grooves 66

Fig. 3. 16 – One-dimensional cavitated fluid film 67

Fig. 3. 17 – Triangular mesh element and its neighbors 74

Fig. 3. 18 – Conservation volume in the (x, z, t) space 75

Fig. 3. 19 – The (x, z, u) space considered for $a-\varepsilon$ and $a-\varepsilon-\alpha-\beta$ schemes 81

Fig. 3. 20 – Uniform triangular mesh 86

Fig. 3. 21 – Ghost elements for the boundary conditions 91

Fig. 3. 22 – Pressure distribution for a circular journal bearing with one inlet groove 94

Fig. 3. 23 – Fractional film content distribution for a circular journal bearing with one inlet 95

Fig. 3. 24a – Circular bearing sleeve 96

Fig. 3. 24b – Wave bearing sleeve 97

Fig. 3. 25 – Fluid film thickness distribution in a 3-wave bearing 98

Fig. 3. 26 – Pressure distribution in a wave bearing $\overline{\beta}' = 3.4$ 100

Fig. 3. 27 – Pressure distribution in a wave bearing $\overline{\beta}' = 40.0$ 101

Fig. 3. 28a – Aligned journal bearing 102

Fig. 3. 28b – Misaligned journal bearing 102

Fig. 3. 29 – Fluid film thickness domain in a misaligned 3-wave bearing 104

Fig. 3. 30a – Pressure distribution in a misaligned 3-wave bearing 105

Fig. 3. 31a – Pressure distribution in a misaligned 3-wave bearing at different axial sections 106

Fig. 3. 32a – Fractional film content distribution in a misaligned 3-wave bearing at different axial sections 107

Fig. 3. 33a – Cavitation map in a misaligned 3-wave bearing 108

Fig. 3.30b – Pressure distribution in an aligned 3-wave bearing 109

Fig. 3. 31b – Pressure distribution in an aligned 3-wave bearing at different axial sections 110

Fig. 3. 32b – Fractional film content distribution in an aligned 3-wave bearing at different axial sections 111

Fig. 3. 33b – Cavitation map in an aligned 3-wave bearing 112

Fig. 4. 1 – Feeding orifice geometry; orifice restrictor 121

Fig. 4. 2 – Feeding orifice geometry; inherent restrictor 121

Fig. 4. 3 – Comparison between numerical and experimental results for the pressure distribution in a gas journal bearing 125

Fig. 4. 4 – Load vs. attitude angle comparison between the present (CE/SE) and finite difference (FD) methods for a gas wave bearing 127

Fig. 4. 5a – Comparison between the calculated and experimental pressure distributions at jet position 129

Fig. 4. 5b – Comparison between the calculated and experimental pressure distributions at mid-jet position 129

Fig. 4. 6 – Pressure distribution for a circular bearing without eccentricity, with five supply planes 131

Fig. 4. 7 – Pressure distribution for a circular bearing with eccentricity, with five supply planes 132

Fig. 5. 1 – Comparison between numerical and experimental results for the pressure distribution in a gas journal bearing 144

$\Lambda = 0.45, \varepsilon_{\exp} = 0.41, \zeta_{\exp} = 0.1496, \theta_{\exp} = 65^0, \varepsilon_{comp} = 0.40, \zeta_{comp} = 0.1540, \theta_{comp} = 69^0$

Fig. 5. 2 – Comparison between numerical and experimental results for the pressure distribution in a gas journal bearing 145

$\Lambda = 1.569, \varepsilon_{\exp} = 0.51, \zeta_{\exp} = 0.545, \theta_{\exp} = 37.5^0, \varepsilon_{comp} = 0.51, \zeta_{comp} = 0.5676, \theta_{comp} = 38.0^0$

Fig. 5. 3 – Comparison between numerical and small perturbation theory results for a plane slider, $\Lambda = \dfrac{6\mu VL}{p_0 h_1^2} = 1.0$, $\alpha' M = \sqrt{\dfrac{2}{3}} \dfrac{V}{2\sqrt{p_0 / \rho_0}}$. 146

Fig. 5. 4 – Comparison between the non-dimensional loads vs. shaft speed with and without inertial effects for three radial clearances $\varepsilon = 0.8$ 148

Fig. 5. 5 – Comparison between the attitude angles vs. shaft speed with and without inertial effects for three radial clearances, $\varepsilon = 0.8$ 149

Fig. 5. 6 – Comparison between the relative difference of the loads with and without inertial effects vs. shaft speed for three radial clearances; $\varepsilon = 0.8$ 150

Fig. 5. 7 – Comparison between the loads with and without inertial effects vs. eccentricity ratio; $\Lambda = 1.223$ and $\mathrm{Re}^* = 24.4$, $C = 100\mu m$, $\dot{n} = 350{,}000\,\mathrm{rev/min} = 36{,}652\,\mathrm{s}^{-1}$ 151

Fig. 5. 8 – Comparison between the non-dimensional loads vs. bearing number with and without inertial effects for three radial clearances; $\varepsilon = 0.8$ 152

Fig. 5. 9 – Comparison between the pressure distributions with and without inertial effects vs. circumferential position for four axial positions; $\Lambda = 1.223$, $\mathrm{Re}^* = 24.4$, $C = 100\mu m$, $\varepsilon = 0.8$, $\dot{n} = 350{,}000\,\mathrm{rev/min} = 36{,}652\,\mathrm{s}^{-1}$ 154

Fig. 5. 10 – Surface plot of the steady-state pressure distribution $\Lambda = 1.223$, $\mathrm{Re}^* = 24.4$, $C = 100\mu m$, $\varepsilon = 0.8$, $\dot{n} = 350{,}000\,\mathrm{rev/min} = 36{,}652\,\mathrm{s}^{-1}$ 155

Fig. 5. 11 – Circumferential velocity distribution vs. circumferential coordinate; $C = 100\mu m$, $\varepsilon = 0.8$, $\dot{n} = 350{,}000\,\mathrm{rev/min} = 36{,}652\,\mathrm{s}^{-1}$ 156

Nomenclature

a	$\frac{U}{2}+g_c\frac{\beta' h}{12\mu}\frac{\partial h}{\partial x}$ For the dimensional form of the governing equation, m/s.
	$\frac{1}{4\pi}+g_c\frac{\overline{\beta'}\overline{h}}{48\pi^2}\frac{\partial \overline{h}}{\partial \overline{x}}$ For the non-dimensional form of the governing equation.
a_F, b_F, c_F	Coefficients in the Taylor series expression of the flux function f for gas bearings.
a_G, b_G, c_G	Coefficients in the Taylor series expression of the flux function g for gas bearings.
b	$g_c\frac{\beta' h^2}{12\mu}$ For the dimensional form of the governing equation, m/s.
	$g_c\frac{\overline{\beta'}\overline{h}^2}{48\pi^2}$ For the non-dimensional form of the governing equation.
c	$g_c\frac{\beta' h^2}{12\mu}\frac{\partial h}{\partial z}$ For the dimensional form of the governing equation, m/s.
	$g_c\frac{\overline{\beta'}\overline{h}}{48\pi^2}\frac{\partial \overline{h}}{\partial \overline{z}}$ For the non-dimensional form of the governing equation.
C	Radial clearance, m.
C_A, C_B	Coefficients, $C_A=\frac{4p_0}{\rho_0\omega^2R^2}$, $C_B=\frac{48\pi\mu}{\omega\rho_0C^2}$, non-dim.

d	$g_c \dfrac{\beta' h^2}{12\mu}$ For the dimensional form of the governing equation for cavitated bearings, m/s.
	$g_c \dfrac{\overline{\beta}' \overline{h}^2}{48\pi^2}$ For the non-dimensional form of the governing equation for cavitated bearings.
e	Radial eccentricity, m.
f	$a\,u - b\dfrac{\partial u}{\partial x}$ Flux term in x direction for cavitated bearings.
	$\dfrac{u\overline{V}}{2} - \dfrac{ku^k}{48\pi^2 \overline{h}^{k-1}}\left(u_x \overline{h} - u\overline{h}_x\right)$ Flux term in x direction for gas bearings.
$\vec{\mathbf{F}}$	$f\,\vec{i} + g\,\vec{k}$ or $F\,\vec{i} + G\,\vec{k}$ Vector flux term.
F, G	Multidimensional flux terms in x and z directions, see Eqs. (5. 10) and (5. 11).
g	$c\,u - d\dfrac{\partial u}{\partial z}$ Flux term in z direction for cavitated bearings.
	$-\dfrac{ku^k}{48\pi^2 \overline{h}^{k-1}}\left(u_z \overline{h} - u\overline{h}_z\right)$ Flux term in z direction for gas bearings.
g_c	Switch function, non-dim.
h	Film thickness, m.
$\overline{h}$	h/C Non-dimensional film thickness, non-dim.
$H_{\max}$, $H_{\min}$	Maximum and minimum values of the film thickness, m.
k	Polytropic exponent, non-dim.
$\vec{\mathbf{i}}, \vec{\mathbf{k}}$	Unit vectors in circumferential and in axial directions, respectively.

L	Length of the slider bearing, m.
	Length of the journal bearing (in axial direction), m.
n_w	Number of waves on the circumference, non-dim.
ns	Number of feeding holes, non-dim.
$\vec{\mathbf{n}}$	Unit vector normal on the contour line, oriented outwards.
$\dot{n}$	Shaft speed, rev/min.
p	Fluid pressure, Pa.
$\bar{p}$	$\bar{p} = p / p_0$, non-dim.
p_c	Cavitation pressure, Pa.
p_s	Supply pressure, Pa.
Q	Vector of the unknowns, see Eq. (5. 9).
Q_m	Mass flow rate, kg/s.
$\overline{Q}_m$	Non-dimensional mass flow rate through one feeding hole, see Eq. (4.21)
r	Radius of the supply orifice for inherent restricted supply systems, m.
r_{orif}, r_p	Radius of the supply orifice, and supply pocket, respectively, for orifice restricted supply systems, m.
R	Journal or wave bearing radius, m.
Re^*	Modified Reynolds number, $\mathrm{Re}^* = \rho_0 \omega C^2 / \mu$, non-dim.
S	Surface area, m^2.
t	Time, s.
$\bar{t}$	$\bar{t} = t\omega$ Non-dimensional time for cavitated bearings.

	$\bar{t} = t\dfrac{p_0}{\mu}\left(\dfrac{C}{R}\right)^2$ Non-dimensional time for gas bearings.
u	$h\theta$ For the dimensional form of the governing equation.
	$\bar{h}\theta$ For the non-dimensional form of the governing equation.
U	Velocity of the slider bearing, m/s.
	Velocity in circumferential direction (ωR) for journal bearings, m/s.
V	Tangential bearing velocity, m/s, $V = \omega R$, m/s.
$\bar{V}$	$\bar{V} = \dfrac{\mu\omega}{2\pi p_0}\left(\dfrac{R}{C}\right)^2$ Non-dim. tangential bearing velocity.
W	Average velocity component in z direction, m/s.
$\bar{U},\bar{W}$	$\bar{U},\bar{W} = 2(U,W)/V$, non-dim.
x	Longitudinal coordinate for slider bearing, m.
	Circumferential coordinate for journal bearings, m.
$\bar{x}$	x/L Non-dimensional longitudinal coordinate for slider bearings.
	$x/(2\pi R)$ Non-dimensional circumferential coordinate for journal bearings.
y	Coordinate in radial (film thickness) direction, m.
z	Axial coordinate, m.
$\bar{z}$	$z/(2\pi R)$ Non-dimensional axial coordinate.
t	Time, s.
$\bar{t}$	$\bar{t} = \omega t/(4\pi)$, non-dim.
α	Exponent used in the second form of artificial dissipation.

β	Weight parameter characterizing the second form of artificial dissipation.
β'	Bulk modulus, Pa.
$\overline{\beta'}$	$\frac{\beta'}{\mu\omega}\left(\frac{C}{R}\right)^2$ Non-dimensional bulk modulus.
γ	Isentropic exponent; $\gamma = 1.405$ for air.
Δt	Time step, s.
Δx	Grid spacing in longitudinal direction for one-dimensional bearings.
ε	Weight parameter characterizing the first form of artificial dissipation.
	e/C Radial eccentricity ratio.
	Slider slope for plane sliders, non-dim.
ε_w	Non-dimensional wave amplitude (for wave bearings).
Λ	Bearing number $\Lambda = (6\mu\omega R^2)/(p_0 C^2)$, non-dim.
μ	Dynamic viscosity, Pa·s.
ρ	Fluid density, kg/m^3.
$\overline{\rho}$	$\overline{\rho} = \rho/\rho_0$, $\rho_0 = 1.85\times10^{-5}$ kg/m^3.
ρ_c	Fluid density at cavitation pressure, kg/m^3.
θ	ρ/ρ_c Non-dimensional density in the full film region.
	Fractional film content in the cavitated region.
ζ	Non-dimensional load, $\zeta = Load/(p_0 2LR)$.
ω	Angular velocity of the journal bearing,s^{-1}.

Subscripts and superscripts

$(\ )_0$	Value of the variable in the point O.
$(\ )_{est}$	Estimated value obtained without use of the governing equation.
$(\ )_j$	Node in longitudinal direction for one-dimensional bearings.
$(\ )_x, (\ )_z, (\ )_t$	Partial derivative with respect to *x*, *z*, and *t*, respectively.
$(\ )^{\pm}$	Derivative calculated with left or right difference formulae.
$(\ )^{a}$	Value obtained in the scheme without artificial dissipation.
$(\ )^{c}$	Derivative calculated using a central difference formula.
$(\ )^{a-\varepsilon}$	Derivative calculated using the $a-\varepsilon$ scheme.
$(\ )^{a-\varepsilon-\alpha-\beta}$	Derivative calculated using the $a-\varepsilon-\alpha-\beta$ scheme.
$(\ )^{n}$	Time step *n*.
$(\ )^{w}$	Derivative calculated using non-linear weighted averaging.

Chapter One

Introduction, Motivation

Computational fluid dynamics (CFD), represents the methodology to numerically solve the equations governing physical phenomena of fluid mechanics and heat transfer. Many fundamental ideas from CFD are relatively old. However, using the extraordinary increases of computational speed and capacity during the last 30 years, CFD has evolved as a full science field, simultaneously mature and extremely dynamic.

Tribology was created as a word in 1968 to identify the science that investigates friction. Even though it is part of tribology, fluid-film lubrication has a much longer history. The first scientific paper in this area is considered to be "First Report of Friction Experiments" by Beauchamp Tower, published by the Institution of Mechanical Engineers in London, in 1883. While applications of fluid-film lubrication date back thousands of years, this field has been founded as a science by Osborne Reynolds through his work on lubrication theory [Reynolds, 1886]. Most modern industries, including power generation, aerospace, transportation, manufacturing, and computer technology, are dependent on progresses in this field, and could not be even imagined without using concepts of fluid lubrication.

This thesis places itself at the confluence between CFD and tribology. On one hand, the present work uses CFD methods. These schemes are applied to solve equations that are derived from the governing equations of fluid mechanics and heat transfer. On the other hand, the engineering applications solved are from the field of fluid-film bearing lubrication. This feature imposes some particular characteristics on the governing equations and boundary conditions used.

There are many research studies involving numerical methods applied to fluid-film bearing problems, and those relevant to this thesis will be referenced herein. This fact attests the importance of the subject, but also suggests the continuous need to improve the numerical predictions for these applications. Theoretical modeling simplifications, associated with extensive experimental work, allowed for significant advancements in the fluid-film lubrication even before the development of modern computers. However, today's increase in computational power, as well as the important progress in numerical methods, provide a different environment. Because numerical solutions that can be used in practice are more powerful and accurate than ever, many theoretical simplifications used to model the problem begin to reach their usefulness. This is one aspect that will be shown in this work. Modeling simplifications are still needed in order to solve real problems. However, some "classical" simplifications, still universally used in engineering practice, have started to become superseded by today's progresses in numerical (and also experimental) techniques.

This work is part of an ongoing research effort within the Department of Mechanical Engineering at the University of Toledo to develop numerical models for the solution of fluid film lubrication problems. On one hand, the significant achievements

obtained during the past several years, for example, [Vijayaraghavan and Keith, 1989], [Vaidyanathan and Keith, 1991], [Yu and Keith, 1995] , [Dimofte, 1995], [Yang and Keith, 1996 - 1 and 2], [Vijayaraghavan, Keith, and Brewe, 1996], [Dimofte, Proctor, Fleming, and Keith, 2000], [Wang, Keith, and Vaidyanathan, 2001, 2002] , [Moraru et. al., 2003], have been important catalysts to improve the quality of the present research. On the other hand, the experience accrued by the computational and experimental thermal sciences focus group also allowed identifying problems that remained unsolved. One of these problems is related to the numerical prediction of discontinuities in the flow.

A theoretical analysis of the governing equations for flows with cavitation leads to the conclusion that the fluid film reformation front can include flow discontinuities. This aspect is a consequence of the character change of the governing partial differential equation from hyperbolic in the cavitated region to elliptic in the full film region [Vijayaraghavan, Keith, and Brewe, 1990]. However, previous numerical methods applied could not capture discontinuities, except for the cases when the location of the reformation front is known a priori. An example of such a case is when the reformation front is imposed by the presence of the supply system. This situation is known in the CFD literature as shock fitting. Obviously, when the location is not known, a shock capturing method [Tannehill, Anderson, and Pletcher, 1997] must be used.

Another situation for which a shock capturing numerical scheme must be used is the case involving gas bearings including the effects of the inertial forces. The classic treatment of gas bearings is to neglect the inertia terms in the governing equations, since a dimensional analysis shows that these terms are small. However, when the bearing speed is very high, the magnitude of these terms can increase, so that they become more

important, and therefore must be included in the equations. In these conditions, the character of the governing equations can change from one region to another, and therefore discontinuities may occur, very similar to the situation in which shock waves are present in a subsonic-supersonic flow.

During the same time, at the NASA Glenn Research Center in Cleveland, Ohio, a novel numerical method was developed. The method was called the space-time conservation element and solution element (CE/SE) method [S.C. Chang et. al., 1991]. It took a relatively long time (5+ years) for this method to start to be used by the scientific community outside of the workgroup where it has been developed. This is an indication of the fact that it is not easy to understand and therefore was not readily implemented. In recent years however, the CE/SE method has been successfully applied to flows both with small and large discontinuities (sound waves and shock waves) [Chang, Wang, and Chow, 1998], jets [Jorgenson and Loh, 2002], [Chang, 2002 - 1 and 2], viscous flows [Chang, Zhang, Yu, and Jorgenson, 2000], cavitation [Qin, Yu, Zhang, and Lai, 2001], detonation [Im and Yu, 2002], phase change [Ayasoufi and Keith, 2003], etc. These complex applications are a proof of the capability and value of the CE/SE method.

Considering the necessity to use a numerical method capable to accurately capture flow discontinuities, and considering the capabilities of the CE/SE scheme as described in the literature, it was decided that this method could be a good candidate to calculate the flow within cavitated bearings, gas bearings, and high-speed gas bearings including inertial effects.

This work is divided into five main parts. After this brief introduction, in the second chapter fluid film bearings concepts are presented, together with the formulation

of the governing equations and correspondent boundary conditions. Gaseous cavitation and Elrod's formulation are also shown there, as they will be used as a starting point (model) for the numerical formulation.

Chapter Three starts with a general presentation of the space-time conservation element and solution element method. Its main features, as shown in the literature by its original authors, are highlighted. The one-dimensional formulation of the method, as applied to cavitated fluid film bearings, is then presented in detail, both for uniform and non-uniform grids. The results obtained show the capability of the formulation to capture flow discontinuities. The two-dimensional formulation applied to cavitated bearings is also described in detail, followed by some representative results obtained for both aligned and misaligned journal and wave bearings.

Chapter Four is dedicated to gas bearings. After a short introduction to the particularities of gas bearings compared to liquid (oil) bearings, the numerical formulation is presented, with emphasis on the differences relative to the previous case. The applications concentrate on pressurized, or hybrid, bearings. These bearings are able to sustain a load with and/or without relative motion between the shaft and the bearing sleeve. Special consideration is given to the modeling of the supply system through the boundary conditions.

Chapter Five presents the application of a model to include the inertial forces in the governing equation of the flow in gas bearings. The Reynolds equation requires the solving of a single differential equation. The inclusion of the inertial effects, in the two-dimensional space, adds two more equations that need to be solved simultaneously with the continuity equation. This fact substantially increases the complexity of the problem,

including the possibility of the occurrence of flow discontinuities. The analytical and numerical formulations of the problem for this case are presented, followed by a comparison between the results obtained with and without inertial effects for a given geometry. The occurrence of flow discontinuities is also shown.

The last chapter is reserved for some conclusions regarding the application of the CE/SE method to flows in thin films. The advantages of the method as revealed throughout the work are restated in a unified way, together with some possible directions to continue this research.

Chapter Two

Fluid Film Bearings and the Reynolds equation

2. 1. The Reynolds Equation

Consider two solid surfaces separated by a thin fluid film, as shown in Fig. 2. 1.

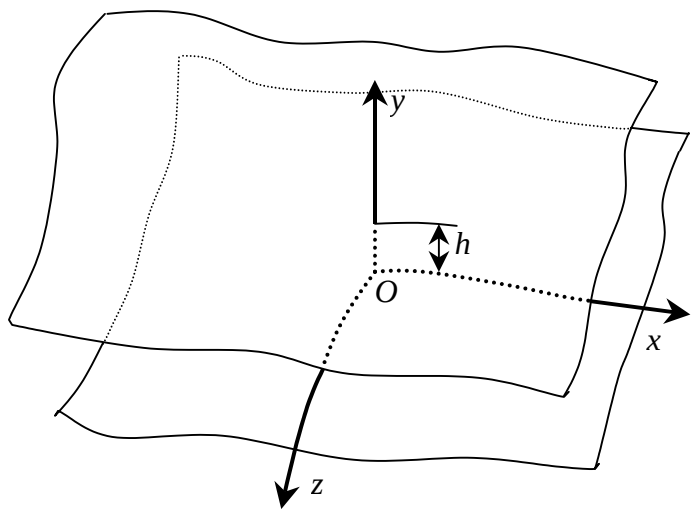

Fig. 2. 1 – Coordinate system for two solid surfaces separated by a thin fluid film

Consider also an orthogonal reference system, with the origin *O* located on one of the two solid surfaces, while axes *Ox* and *Oz* are contained in the same solid surface. Because the surfaces can be curved (as in the case of journal bearings), the axes can also be curved.

The film thickness, measured in the direction of axis *Oy*, is a function of two spatial coordinates and time

$$h = h(x, z, t). \tag{2. 1}$$

Thickness *h* is considered to be very small compared with the other dimensions of the lubricated surfaces

$$\frac{h}{l} \approx O(10^{-3}), \tag{2. 2}$$

where *l* is a characteristic length of the lubricated surfaces. For slider bearings *l* is usually the length of the bearing, whereas for journal bearings, according to various authors, the length *l* can be the bearing radius, diameter, or circumference. The hypothesis given by Eq. (2. 2) allows the introduction of an important simplifying assumption: the curvatures of the lubricated surfaces are negligible. Indeed, considering that the curvature radii of the solid surfaces are at least of the order of magnitude *l* (for curved surfaces, a characteristic length can be considered as the minimum radius of curvature), the ratio $h/l \approx O(10^{-3})$ is an indication of the error introduced when neglecting the curvature. This error is acceptable for all practical cases.

The two surfaces are considered to have a general instantaneous translation motion given by (U_1, V_1, W_1) and (U_2, V_2, W_2), where *U*, *V*, and *W* are the velocity components in directions *x*, *y*, and *z*, respectively, and indices 1 and 2 refer to the two solid surfaces. Consider that surface 1, which contains the axis origin *O*, has a motion tangent in all points to this surface. This is the normal case for bearing lubrication problems. This assumption is equivalent to the condition

$$V_1 = 0. \tag{2. 3}$$

The boundary conditions for the fluid are then:

On boundary 1: at $y = 0 \rightarrow u = U_1, v = V_1 = 0, w = W_1$. (2. 4)

On boundary 2: at $y = h \rightarrow u = U_2, v = V_2, w = W_2$. (2. 5)

The following assumptions are made:

a) *The medium is a continuum*. This assumption is valid as long as the film thickness is larger than the mean free path of the fluid molecules. For instance, the free path of gas molecules is about 65 nm in normal operating conditions, while the minimum film thickness in gas journal bearings has the order of magnitude of one μm. However, in applications like the hard disk drive slider, the film thickness can attain values on the order of 10 nm. Thus, in this case the assumption is no longer valid [Wu and Bogy, 2001].

b) *There is no slip at the boundaries*. This assumption has been included in Eqs. (2.4) and (2.5). Again, in cases like the gas rarefaction that occur when the film thickness is extremely small, this assumption is not valid. Also, special kinds of fluids do not follow this assumption [Tipei, 1980].

c) *The fluid is Newtonian*. This assumption is considered to be accurate for gas bearings, but the physics involving oils can be significantly different from the Newtonian model, especially in cases that involve high pressures. A non-Newtonian model must be considered in such applications, as in [Wang, Keith, and Vaidyanathan, 2001], or [Cioc et. al., 2002].

d) *The flow is laminar*. This assumption is based on the idea that the film thickness is very small, and therefore the Reynolds number is also very small. Hence viscous forces prevent the initiation of turbulence. However, some practical applications

that include high-speed bearings with film thickness discontinuities can develop turbulence. A turbulence model must then be included [Ng and Pan, 1965], [Elrod and Ng, 1967], [Hirs, 1974], [Constantinescu and Galetuse, 1982].

e) *The external body forces are negligible*. Body forces, like gravity or centripetal forces, are usually small compared with the pressure forces or the shear forces. What is more, in normal applications these forces do not contribute to the fluid flow [Bird, Stuart, and Lightfoot, 1960].

f) *The inertia forces are negligible*. Again, these forces are usually small compared with the pressure or with the shear forces. This assumption has profound implications in the simplification of the flow governing equations. However, when the flow has discontinuities or steep variations, these forces can have significant influence, [Constantinescu, 1995], [Szeri, 1998].

g) *The surfaces curvature is neglected*. This assumption has been discussed earlier. In certain cases, as when the film thickness has steep variations, the surface curvature can have an influence, and it should be considered, [Szeri, 1998].

h) *The surfaces are smooth*. All surfaces have irregularities, resulting from the manufacturing processes. When the fluid film thickness is much larger than the surface irregularities, the influence of the roughness can be considered negligible compared with other factors. This assumption is not valid for very thin films (for example boundary lubrication), [Wang, Keith, and Vaidyanathan, 2002].

i) *The surfaces are rigid*. The pressure developed in the fluid film contributes to the surface elastic, and possibly even plastic, deformation. This influence is negligible for most fluid film lubrication applications. However, when film

pressures are very large, surface deformation must be considered. Because this deformation affects the film thickness, it will also affect the pressure distribution, so that the surface deformation equations must be solved simultaneously with the fluid film equation(s) [Cioc et. al., 2003].

j) *The film thickness is small compared with the other dimensions*. This is called the fundamental hypothesis of lubrication, and is implicitly included in many of the above model assumptions, [Frêne et. al., 1997].

k) *Fluid density and fluid viscosity are constant across the film thickness, i.e.,* $\rho, \mu = \rho, \mu(x, z, t)$. This assumption enables very important simplifications when the governing equations are integrated across the film thickness. When the temperature change across the film is important, the assumption of constant density and viscosity across the fluid film may become a source of errors, [Frêne et. al., 1997].

l) *Pressure is constant across the film thickness,* $p = p(x, z, t)$. More than an assumption, this is a consequence of the fundamental hypothesis of lubrication applied to the momentum conservation equation, using dimensional analysis [Frêne et. al., 1997].

m) *The velocity components in x and z directions are*

$$u = \frac{1}{2\mu}\frac{\partial p}{\partial x} y(y-h) + U_1 \frac{h-y}{h} + U_2 \frac{y}{h}, \tag{2. 6}$$

$$w = \frac{1}{2\mu}\frac{\partial p}{\partial z} y(y-h) + W_1 \frac{h-y}{h} + W_2 \frac{y}{h}. \tag{2. 7}$$

These equations are a result of assumptions a)-l).

Based on conditions a) to m), the Reynolds equation [Frêne et. al., 1997] is

$$\frac{\partial}{\partial x}\left(\frac{\rho h^3}{\mu}\frac{\partial p}{\partial x}\right)+\frac{\partial}{\partial z}\left(\frac{\rho h^3}{\mu}\frac{\partial p}{\partial z}\right)=6\rho(U_1-U_2)\frac{\partial h}{\partial x}+6\rho(W_1-W_2)\frac{\partial h}{\partial z}$$
$$+6h\frac{\partial}{\partial x}[\rho(U_1+U_2)]+6h\frac{\partial}{\partial z}[\rho(W_1+W_2)]+12\rho V_2+12h\frac{\partial \rho}{\partial t}. \tag{2. 8}$$

Equation (2.8) can further be simplified when surface 2 has only a velocity normal to the fluid film, i.e., in *y* direction. In that case,

$$U_2=W_2=0\,,\quad V_2=\frac{\partial h}{\partial t}. \tag{2. 9}$$

Also, the *x*-axis coincides with the tangential velocity *U* of surface 1,

$$U=\sqrt{U_1^2+W_1^2}\ . \tag{2. 10}$$

Considering Eqs. (2.9) and (2.10), Eq. (2.8) becomes

$$\frac{\partial}{\partial t}(\rho h)+\frac{\partial}{\partial x}\left(\frac{\rho hU}{2}-\frac{\rho h^3}{12\mu}\frac{\partial p}{\partial x}\right)+\frac{\partial}{\partial z}\left(-\frac{\rho h^3}{12\mu}\frac{\partial p}{\partial z}\right)=0\,. \tag{2. 11}$$

This simplified form of the Reynolds equation can also be easily developed in the following manner. Consider an infinitesimally small control volume full of fluid as shown in Fig. 2.2, where coordinates *x* and *z*, as well as time *t*, can have any value in the domain considered. The upper and lower boundaries of the control volume are situated on the solid surfaces, considered to be impermeable, while the lateral boundary surfaces are fixed and permeable. The total volume of the control volume is thus

$$Vol=h(x,z,t)\Delta x\Delta z\ . \tag{2. 12}$$

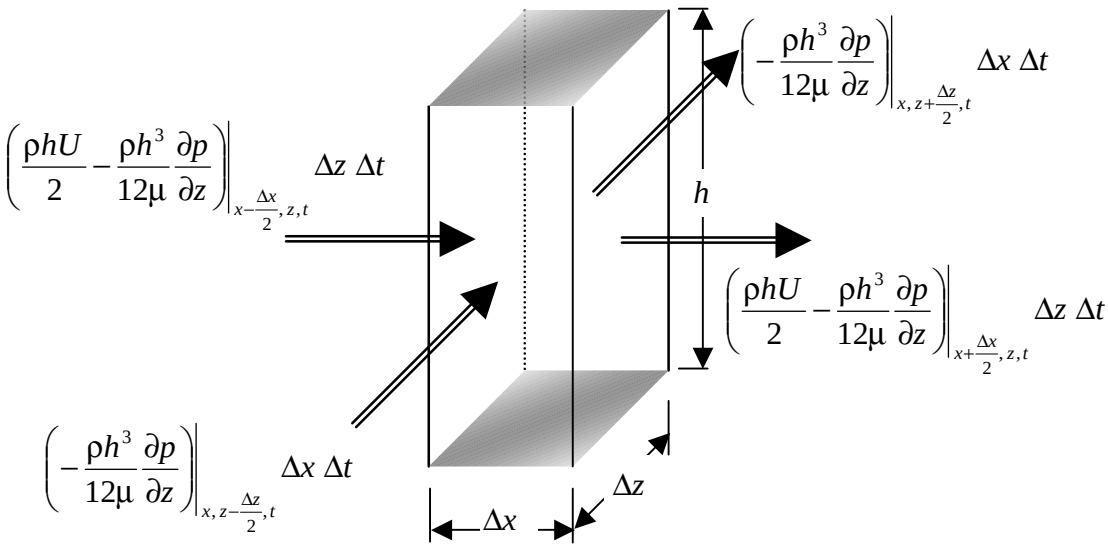

Fig. 2. 2 – Control volume

The mass conservation principle states that the fluid mass accumulation in the control volume must be equal with the sum of the mass flow rates that enter and exit the volume through its boundaries.

The flow in the thin fluid film is, according to assumptions a)-i), the sum (superposition) of a one-dimensional Couette flow (in direction *x*) and a two-dimensional Poiseuille flow (in directions *x* and *z*). Consider first the Couette flow (Fig. 2.3).

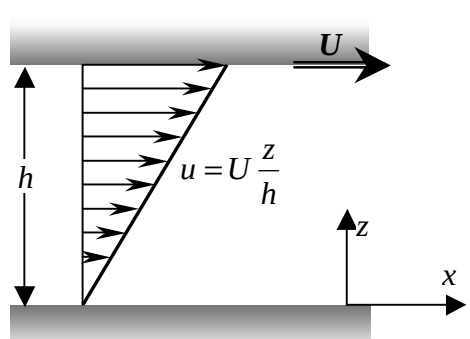

Fig. 2. 3 – Couette flow in *x* direction

The mass flow rate in direction x for a unit width in the z direction is

$$\dot{m}_{Couette} = \frac{1}{2}\rho h U \ . \tag{2. 13}$$

Consider the Poiseuille flow in the x direction (Fig. 2.4).

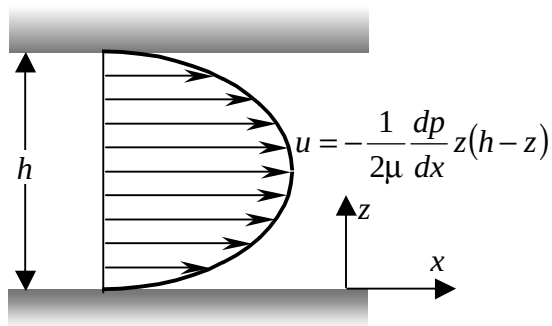

Fig. 2. 4 – Poiseuille flow in x direction

The mass flow rate for a unit width in z direction is

$$(\dot{m}_x)_{Poiseuille} = -\frac{\rho h^3}{12\mu}\frac{\partial p}{\partial x} \ . \tag{2. 14}$$

Similarly, in the z direction, the Poiseuille or pressure driven mass flow rate is

$$(\dot{m}_z)_{Poiseuille} = -\frac{\rho h^3}{12\mu}\frac{\partial p}{\partial z} \ . \tag{2. 15}$$

Consider the time interval $\left[t - \frac{\Delta t}{2}, t + \frac{\Delta t}{2}\right]$ of length Δt. The fluid mass accumulation in the control volume for this time interval is

$$(\rho h \Delta x \Delta z)_{x,x,t+\frac{\Delta t}{2}} - (\rho h \Delta x \Delta z)_{x,x,t-\frac{\Delta t}{2}} \ . \tag{2. 16}$$

The mass flow balance for the same control volume, in the same time interval is:

- x direction: $\left[\left(\dot{m}_{Couette}+\left(\dot{m}_x\right)_{Poiseuille}\right)\Big|_{x-\frac{\Delta x}{2},z,t}-\left(\dot{m}_{Couette}+\left(\dot{m}_x\right)_{Poiseuille}\right)\Big|_{x+\frac{\Delta x}{2},z,t}\right]\Delta z\Delta t$.

- z direction: $\left[\left(\dot{m}_z\right)_{Poiseuille}\Big|_{x,z-\frac{\Delta z}{2},t}-\left(\dot{m}_z\right)_{Poiseuille}\Big|_{x,z+\frac{\Delta z}{2},t}\right]\Delta x\Delta t$.

The mass conservation principle is therefore,

$$\begin{aligned}\left(\rho h\Delta x\Delta z\right)_{x,x,t+\frac{\Delta t}{2}}-\left(\rho h\Delta x\Delta z\right)_{x,x,t-\frac{\Delta t}{2}}&=\Delta z\Delta t\Bigg[\left(\dot{m}_{Couette}+\left(\dot{m}_x\right)_{Poiseuille}\right)\Big|_{x-\frac{\Delta x}{2},z,t}\\&-\left(\dot{m}_{Couette}+\left(\dot{m}_x\right)_{Poiseuille}\right)\Big|_{x+\frac{\Delta x}{2},z,t}\Bigg]+\Delta x\Delta t\Bigg[\left(\dot{m}_z\right)_{Poiseuille}\Big|_{x,z-\frac{\Delta z}{2},t}-\left(\dot{m}_z\right)_{Poiseuille}\Big|_{x,z+\frac{\Delta z}{2},t}\Bigg].\end{aligned}\tag{2. 17}$$

Substituting the expressions for the mass flow rates per unit width, Eqs. (2.13) and (2.15), into Eq. (2.17) yields,

$$\begin{aligned}\left(\rho h\Delta x\Delta z\right)_{x,x,t+\frac{\Delta t}{2}}-\left(\rho h\Delta x\Delta z\right)_{x,x,t-\frac{\Delta t}{2}}&=\Delta t\Bigg[\Delta z\left(\frac{1}{2}\rho hU-\frac{\rho h^3}{12\mu}\frac{\partial p}{\partial x}\right)_{x-\frac{\Delta x}{2},z,t}\\&-\Delta z\left(\frac{1}{2}\rho hU-\frac{\rho h^3}{12\mu}\frac{\partial p}{\partial x}\right)_{x+\frac{\Delta x}{2},z,t}+\Delta x\left(-\frac{\rho h^3}{12\mu}\frac{\partial p}{\partial z}\right)_{x,z-\frac{\Delta z}{2},t}-\Delta x\left(-\frac{\rho h^3}{12\mu}\frac{\partial p}{\partial z}\right)_{x,z+\frac{\Delta z}{2},t}\Bigg].\end{aligned}\tag{2. 18}$$

Equation (2.18) is now divided by $\Delta x\Delta z\Delta t$ to get

$$\begin{aligned}\frac{\left(\rho h\right)_{x,x,t+\frac{\Delta t}{2}}-\left(\rho h\right)_{x,x,t-\frac{\Delta t}{2}}}{\Delta t}&=-\frac{\left(\frac{1}{2}\rho hU-\frac{\rho h^3}{12\mu}\frac{\partial p}{\partial x}\right)_{x+\frac{\Delta x}{2},z,t}-\left(\frac{1}{2}\rho hU-\frac{\rho h^3}{12\mu}\frac{\partial p}{\partial x}\right)_{x-\frac{\Delta x}{2},z,t}}{\Delta x}\\&+\frac{\left(\frac{\rho h^3}{12\mu}\frac{\partial p}{\partial z}\right)_{x,z+\frac{\Delta z}{2},t}-\left(\frac{\rho h^3}{12\mu}\frac{\partial p}{\partial z}\right)_{x,z-\frac{\Delta z}{2},t}}{\Delta z}.\end{aligned}\tag{2. 19}$$

Taking the limits as $\Delta x\to 0$, $\Delta z\to 0$, and $\Delta t\to 0$, Eq. (2.19) becomes,

$$\frac{\partial}{\partial t}\left(\rho h\right)=-\frac{\partial}{\partial x}\left(\frac{\rho hU}{2}-\frac{\rho h^3}{12\mu}\frac{\partial p}{\partial x}\right)+\frac{\partial}{\partial z}\left(\frac{\rho h^3}{12\mu}\frac{\partial p}{\partial z}\right),\tag{2. 20}$$

which is the same as Eq. (2.11).

This shows again that the Reynolds equation is a particular form of the mass conservation principle. The particular form assumes that the velocity profile across the film thickness is the sum of the Couette and Poiseuille velocity profiles. This assumption practically includes all assumptions a)-l) written for the simplified case given by Eqs. (2.9) and (2.10), and it also includes the boundary conditions at the walls.

The unknowns in the any of the forms Eq. (2.8) or Eq. (2.11) of the Reynolds equation are the fluid density ρ and the pressure *p* at each point (x, z, t), while the film thickness *h* and fluid viscosity μ are usually known. In cases in which they depend on the density and pressure distributions, then $h, \mu = h, \mu(\rho, p)$; therefore, iterative procedures are used where at each new iteration *k* they are expressed as functions of the old iteration $(k-1)$ value, i.e. $h, \mu|^{k} = h, \mu\left(\rho|^{k-1}, p|^{k-1}\right)$. Examples of applications where this technique is utilized include: rotor dynamics, where the rotor position in the bearing depends on the pressure distribution [Childs, 1993], or elasto-hydrodynamic lubrication, where the pressures are very high, and the viscosity can no longer be considered constant [Cioc et. al., 2002]. In this work, when no other specifications are made, the film thickness *h* and fluid viscosity μ are considered known.

Because there are two unknown field variables, in order to close the problem, at least one other equation is needed. The closure is completed in many different ways, depending on the type of fluid used, or on the model considered.

a) The fluid is perfectly incompressible. In this case the density is constant, and the pressure is the only unknown:

$$\rho = const. \tag{2. 21}$$

In this particular case the Reynolds equation is linear. Almost all analytical results have been obtained for incompressible fluids, and of course most numerical methods can be used to solve this problem.

b) The fluid is compressible, but there exists a direct relationship between the fluid density and fluid pressure,

$$\rho = \rho(p). \tag{2. 22}$$

In this case the Reynolds equation is non-linear, and complex pressure and density distributions can occur. The case of compressible fluids will be generally considered in this thesis. One special situation in this study is that of cavitated bearings.

c) Additional equation(s) and variables are considered. One example is the introduction of one additional variable (fluid temperature), one additional differential equation, (the energy equation), and one ore more additional equation(s) to determine the density and/or viscosity as functions of pressure and temperature [Arghir and Frêne, 2002].

2. 2. Boundary conditions

Boundary conditions must be individually prescribed for each problem solved. Since Reynolds equation is essentially the same, the individuality of each problem is therefore determined mainly by the boundary conditions. However, there are some situations that occur frequently, which can be presented as general boundary conditions for journal bearings.

a) *Conditions at the bearing lateral ends*.

At the bearing lateral ends the pressure can be either atmospheric pressure, or a prescribed constant value for submerged bearings. For cavitated bearings, an additional boundary condition referring to the fractional film content must be imposed when the cavitation region reaches the bearing ends, since the pressure is not the defining parameter for these regions.

b) *Conditions at the bearing supply system*.

Many bearings use a supply system that brings pressurized fluid into the bearing clearance. Two choices occur in this case:

b-1) The supply holes are considered part of the bearing computational domain, i.e. the supply holes areas inside the bearing are covered with grid points/elements. This is the most common choice, and it is treated by imposing a supply pressure value on the grid points/elements that are inside the supply holes. Since this value is not determined from the governing equation, and since the Reynolds equation is a mass conservation equation, this condition is equivalent to imposing a mass flow rate into or out of these grid points/elements (the mass conservation is not satisfied at these locations). The same argument is also valid at the bearing ends. More details will be included in subsequent chapters of this work.

b-2) The supply holes are considered outside the computational domain. This choice may be used mostly for supply systems with relative large pockets. For this case, the pressure must be imposed on the contours of the supply holes, while the shape of the computational domain becomes more complicated than in the previous case.

c) *Conditions at the bearing center-plane*.

When the bearing has a symmetry plane, the computational domain can be halved to reduce the computation time. In this case, symmetry boundary conditions must be imposed at the section plane.

d) *Conditions at the cavitation region boundaries*.

Cavitation is discussed in the following paragraph.

2. 3. Cavitation in liquid-lubricated bearings

Cavitation is a physical phenomenon that occurs when the pressure inside a liquid is small enough so that pockets of vapors and gases form. In journal bearings for example, the pressure tends to be smaller than the exterior pressure in relatively large regions. In this case, there are three possible processes [Frêne et. al., 1997]:

i) Air, or more generally, gas from the atmosphere, enters into the low-pressure region until the pressure becomes equal to the ambient pressure.

ii) Gas dissolved in the liquid is expelled from it until the pressure reaches the saturation value.

iii) The pressure is smaller than the saturation pressure of the liquid, so that the liquid vaporizes at the ambient pressure under low pressure. The vapor bubbles can later implode, contributing to the surface deterioration. This case is the only one strictly meeting the definition of cavitation, but nonetheless the first two processes, which are the most frequent in fluid film bearings, are also considered part of this phenomenon.

Historically, the effects of cavitation on the performance of bearings were disregarded in numerical calculations. The common practice, known as Gümbel (or half-

Sommerfeld) boundary conditions, was to modify full film results by setting negative relative pressures (relative to the cavitation pressure) to zero. Although the load carrying predictions were reasonably accurate, especially for short bearings, the results violated the mass conservation principle. Consequently, several other procedures have been proposed. Jakobsson and Floberg (1957) and later Olsson (1965) introduced a set of self-consistent boundary conditions for cavitation to be applied to Reynolds equation. This procedure is valid for moderately to heavy loaded bearings and is generally called JFO theory. This methodology is commonly incorporated into modern computational algorithms for bearings, and is also implicitly included in the present work, as shown later. However, it must be mentioned that the modeling of the cavitation in fluid film bearings is still being researched [Groper and Etsion, 2001].

When cavitation occurs, the fluid film bearing domain is divided into two sub-domains: the full film region and the cavitated region. While in the full film region the classic Reynolds equation holds, in the cavitation region the pressure is considered to be equal with the cavitation pressure p_c, which is a constant over the surface of the bearing. In this region it is considered that only one fraction θ of the film thickness is filled with liquid, and this liquid adheres to both the bearing and shaft surfaces. The gas is considered to have negligible density compared to the density of the liquid, so that the density of the fluid in the cavitation region is $(\theta \cdot \rho)$. In these conditions, the Reynolds equation [Frêne et. al., 1997] divided by $(6h)$ becomes

$$\frac{\partial}{\partial x}\left[\theta\rho(U_1+U_2)h\right]+\frac{\partial}{\partial z}\left[\theta\rho(W_1+W_2)h\right]=2\theta\rho\left[U_2\frac{\partial h}{\partial x}+W_2\frac{\partial h}{\partial z}-2V_2\right]+2h\frac{\partial(\theta\rho)}{\partial t}, \quad (2.\ 23)$$

or, considering, as in Eq. (2.9), that surface 2 has only a normal to the fluid film velocity, Eq. (2.23) becomes

$$\frac{\partial}{\partial x}\left[\theta\rho\left(U_1+U_2\right)h\right]+\frac{\partial}{\partial z}\left[\theta\rho\left(W_1+W_2\right)h\right]=2\frac{\partial\left(\theta\rho h\right)}{\partial t}. \tag{2. 24}$$

Because different equations govern the fluid flow in the full film and in the cavitated film regions, boundary conditions must be used at the interface between the two regions. These conditions must reflect the mass flow rate continuity across the cavitation boundary. Consider a cross section through the cavitation boundary, as shown in Fig. 2.5 for the fluid film rupture boundary (the cross-section is normal to the boundary, in direction *n*).

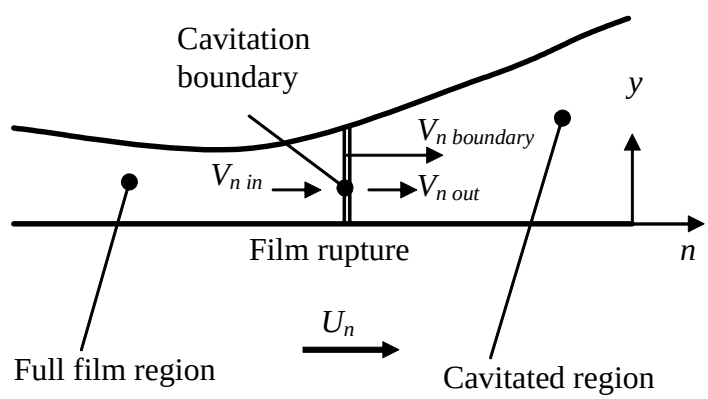

Fig. 2. 5 – Cavitation boundary

In the full film region, the mass flow rate of fluid entering through the boundary per unit length is

$$\dot{m}_{in}=\int_0^h \rho\left(V_{n\ in}-V_{n\ boundary}\right)\mathrm{d}y=\rho h\left(\frac{U_n}{2}-\frac{h^2}{12\mu}\frac{\partial p}{\partial n}-V_{n\ boundary}\right), \tag{2. 25}$$

where $V_{n\ in}$ is the velocity component of the fluid normal to the cavitation boundary, and the boundary is considered to have the velocity $V_{n\ boundary}$ in direction *n*. The fluid velocity is due to the Couette and Poiseuille components, as previously shown in Eq. (2.20), calculated in the direction normal to the boundary direction, *n*.

In the cavitated film region, the pressure is constant, and in agreement with the cavitation model that considers a fraction θ of liquid component that adheres to both upper and lower surfaces, the mass flow rate is

$$\dot{m}_{in} = \int_0^h \rho\left(V_{n\ out} + V_{n\ boundary}\right)\mathrm{d}y = \theta\rho h\left(\frac{U_n}{2} + V_{n\ boundary}\right) \tag{2. 26}$$

The boundary condition thus becomes

$$\dot{m}_{in} = \dot{m}_{out}\,, \tag{2. 27}$$

or,

$$\rho h\left(\frac{U_n}{2} - \frac{h^2}{12\mu}\frac{\partial p}{\partial n} - V_{n\ boundary}\right) = \theta\rho h\left(\frac{U_n}{2} + V_{n\ boundary}\right). \tag{2. 28}$$

Note that the same condition holds for the reformation boundary, since in this case all the signs of the mass flow rates will change. Equation (2.28) can also be written as

$$(1-\theta)\left(\frac{U_n}{2} - V_{n\ boundary}\right) - \frac{h^2}{12\mu}\frac{\partial p}{\partial n} = 0\,. \tag{2. 29}$$

For the steady state case, in which the cavitation boundary is fixed, $\left(V_{n\ boundary} = 0\right)$, Eq. (2.29) becomes

$$(1-\theta)\frac{U_n}{2} - \frac{h^2}{12\mu}\frac{\partial p}{\partial n} = 0\,. \tag{2. 30}$$

Note that the value of the fractional film content is calculated at the boundary inside the cavitated region, while the pressure derivative normal to the boundary is calculated inside the full film region.

Consider the case of the film rupture. Immediately before the rupture, the pressure can only decrease $\frac{\partial p}{\partial n} \leq 0$, because the minimum pressure occurs inside the cavitation region $p = p_c = p_{\min}$. Since the fractional film content can only be smaller than unity, $\theta \leq 1$, the only possibility for the boundary condition, Eq. (2.30), to hold is

$$\theta = 1, \tag{2. 31}$$

and

$$\frac{\partial p}{\partial n} = 0. \tag{2. 32}$$

These conditions show that across the film rupture the pressure, pressure gradient, and fractional film are continuous functions.

Consider the case of the film reformation. Using the same analysis as before, the pressure after the reformation can only increase $\frac{\partial p}{\partial n} \geq 0$. When the pressure gradient is strictly positive, $\frac{\partial p}{\partial n} > 0$, the fractional film content before the reformation must strictly be smaller than unity, i.e., $\theta < 1$. This shows that at the reformation boundary the fractional film content, and also the pressure gradient, can have discontinuities. Later, in the next chapter, it will be shown that in this case the pressure must be a discontinuous function as well.

The location of the cavitation boundary is not known, and it must be determined during the solution. The JFO theory includes equations for the cavitation boundary. Using a different approach, as shown next, these equations have not been used in this work.

An alternative approach to considering two different kinds of domains (full film and cavitated) with boundary conditions at the interface between them is to use Elrod's formulation [Elrod, 1981]. In this case the governing equation is written in a unified way for both regions using the definition of the bulk modulus β'

$$\beta' = \rho \frac{\partial p}{\partial \rho} \tag{2. 33}$$

In order to work in terms of density, a non-dimensional density variable, θ, is introduced

$$\theta = \frac{\rho}{\rho_c}, \tag{2. 34}$$

where ρ_c is the density of the lubricant at the cavitation pressure, considered constant. The bulk modulus definition becomes in this case

$$\beta' = \theta \frac{\partial p}{\partial \theta} \ . \tag{2. 35}$$

The Reynolds equation yields, in terms of the non-dimensional density

$$\frac{\partial \rho_c h \theta}{\partial t} + \frac{\partial}{\partial x}\left(\frac{\rho_c h \theta U}{2} - \frac{\rho_c \beta' h^3}{12\mu} \frac{\partial \theta}{\partial x} \right) + \frac{\partial}{\partial z}\left(-\frac{\rho_c \beta' h^3}{12\mu} \frac{\partial \theta}{\partial z} \right) = 0 \ . \tag{2. 36}$$

Considering that in the cavitation region the flow induced by the pressure is negligible, i.e.,

$$\begin{aligned} \frac{\partial}{\partial x}\left(\frac{\rho h^3}{12\mu} \frac{\partial p}{\partial x} \right) &= \frac{\partial}{\partial x}\left(\frac{\rho_c \beta' h^3}{12\mu} \frac{\partial \theta}{\partial x} \right) \cong 0, \\ \frac{\partial}{\partial z}\left(\frac{\rho h^3}{12\mu} \frac{\partial p}{\partial z} \right) &= \frac{\partial}{\partial z}\left(\frac{\rho_c \beta' h^3}{12\mu} \frac{\partial \theta}{\partial z} \right) \cong 0, \end{aligned} \tag{2. 37}$$

a switch function, g_c,

$$g_c = \begin{cases} 1 - full\ \ film\ region, \theta \geq 1 \\ 0\ \ - cavitated\ \ region, 0 < \theta < 1 \end{cases}$$

(2. 38)

is introduced into the pressure-density relation,

$$g_c \beta' = \rho \frac{\partial p}{\partial \rho}\ , \tag{2. 39}$$

so that the Reynolds equation can be written as,

$$\frac{\partial h\theta}{\partial t} + \frac{\partial}{\partial x}\left(\frac{h\theta U}{2} - g_c \frac{\beta' h^3}{12\mu}\frac{\partial \theta}{\partial x}\right) - \frac{\partial}{\partial z}\left(g_c \frac{\beta' h^3}{12\mu}\frac{\partial \theta}{\partial z}\right) = 0\ . \tag{2. 40}$$

The pressure-density relation yields, by direct integration,

$$p = p_c + g_c \beta' \ln \theta\ , \tag{2. 41}$$

where the cavitation pressure p_c is a constant as a result of the switch function assumption.

Using one single field variable for both regions, and one single form for the governing equations in both regions, this formulation is not only an elegant approach for the modeling of the flow in cavitated bearings, but it also simplifies the numerical solver because it allows the use of a single numerical method for both regions. However, because the governing equation has different characters in the two regions, and because field discontinuities can occur at the reformation fronts, the numerical scheme must be able to handle in an accurate way these potential problems.

A potential drawback of the method is related to the value of the bulk modulus, β'. This coefficient accounts for the compressibility of the lubricant in the liquid state,

and it must be determined experimentally. Ideal liquids (incompressible) have $\beta' \to \infty$. Real liquids are compressible, and thus $\beta' = \mathit{finite}$. However, the bulk modulus has high values, with the order of magnitude being 7-8 or higher in the international (metric) system of units. When an explicit numerical method is used to solve the governing equations the time step is bounded by the CFL condition. Therefore, higher values for the bulk modulus will reduce the maximum allowed time step. Smaller time steps will determine an increase of the computational effort and also an increase of the dissipation in the cavitated regions, where the bulk modulus does not appear, and thus the Courant number becomes much smaller than 1.0. This feature will also be discussed in the following chapters.

Chapter Three

Application of the CE/SE Method to Cavitated Bearings

3. 1. Introduction: the CE/SE method.

The space-time conservation element and solution element (CE/SE) method was proposed for the first time at the NASA Glenn Research Center, in Cleveland, Ohio, [Chang and To, 1991]. Over the past several years it has been utilized in a number of computational fluid dynamics applications; for example jet and fan noise prediction [Jorgenson and Loh, 2002], flows with shock/acoustic wave interactions [Wang, Chang, and Jorgenson, 2000], and shock tube problems [Chang, Wang, and Chow, 1998]. It has also been applied to problems involving chemical reactions [Yu and Chang, 1997 - 2], detonation, [Im and Yu, 2002], and phase change, [Ayasoufi and Keith, 2003]. One of its main features is that it can simultaneously capture small and large discontinuities (such as sound waves and shock waves) without introducing numerical oscillations in the solution [Wang, Chang, Jorgenson, 2000], [Chang, Wang, Chow, 1999], [Qin, Yu, Zhang, Lai, 2001], et al. Accordingly, this new method is an excellent candidate to be applied to the flow in cavitated bearings.

The general principles of the method are explained in [Chang, Wang, and Chow, 1998], and they show that “the method has been built from the fundamentals, and not as a

modification of any previous existing method”. As a general feature, the CE/SE method has been developed to solve conservation laws in continuum mechanics. The following provides some features and advantages of the method, which are based on the guidelines of the original authors of the method. These features will be illustrated in the applications for the fluid film bearing flows.

1. Perhaps the most important characteristic of the CE/SE method is that space and time are treated in a unified fashion. While most numerical methods (FD, FEM, FV) handle space and time differenced terms in the governing equations separately, this scheme treats them in a unified way. The solution is approximated with simple (linear) functions within the “solution elements” (SE), and the conservation law is imposed, on each "conservation element" CE, in the space-time hyperspace. This results in very good accuracy even though the unknowns are approximated locally in a simple fashion (linear for example) and even when a relatively coarse grid is used.

2. The CE/SE method emphasizes the integral form of the conservation laws. This characteristic is also common for the FE and FV methods. However, as shown below, for each CE, the CE/SE scheme enforces the conservation of the flux in the combined space-time hyperspace. Some important advantages occur from this feature:

2a. Even when the differential form of the governing equation is second order, linear local approximations can be used in the discretization process.

2b. Even when linear local approximations are used, the solution will be second order accurate, i.e., the integral form of the governing equation will be satisfied with second order accuracy.

2c. The accuracy of the method has the same order both in space and time when the same order functions of space and time are used. Traditional methods address flux conservation for the space component only.

3. The CE/SE method can be very simply described in terms of the geometry of the discretization. No knowledge of the properties of the solution is necessary. In other words, unlike most numerical schemes, no special treatment is necessary for discontinuities, or for different characteristic regions, providing that the governing equations are written in strong conservative form. This property radically contributes to the generality of the scheme and to the codes built on it. The method itself is not trivial to describe and to understand. This is proven also by the fact that it took more than 5 years from the first publication of the method to its application by researchers not directly working with the original authors. However, a computer code based on the method can be structured in a relatively simple way, while maintaining its general character.

4. Fluxes are calculated at the conservation elements boundaries without interpolation or extrapolation. In particular, no Riemann solver is needed in calculating interfacial fluxes, as in traditional FV methods. This feature is insured by the way the numerical solution is constructed on the SE domain.

5. The gradients of the solution are not calculated through a reconstruction procedure, as in upwind methods. These gradients are considered as unknown independent variables, and determined as part of the solution. Also, for hyperbolic problems, the gradients are thus not influenced by the solution at the same time level, which is in full compliance with the physics of the hyperbolic initial value problem. Note however that both of these characteristics of the method have been relaxed in order to

simplify the solution procedure. When preserving the first property (gradients considered as independent unknowns), the method is locally implicit. Therefore, a simplified procedure is used in practice, which renders the fully explicit character of the method. In that case however the gradients are calculated not from the conservation condition, but from the solution, as in traditional methods. As for the second characteristic (gradients not influenced by the solution at the same time level), there is a variation of the method that does not comply with it, again for the sake of simplicity.

6. For simulation of isentropic, inviscid flow, the explicit solvers used following the CE/SE scheme are neutrally stable for all Courant numbers smaller than unity. This characteristic follows the most recent developments of the method, which include a Courant insensitive scheme, [Chang, 2002-3], [Chang and Wang, 2003].

7. For non-isentropic flows, some artificial dissipation is used, but the amount is completely controlled by adjustable parameters. Thus, artificial dissipation can be made zero, for a case in which the scheme reduces to a non-dissipative version. This feature becomes important in thin boundary layers and acoustic waves problems, since excessive damping can smear the numerical solution.

8. In the case of one-dimensional convection-diffusion problems, the amplification factor determined by a von Neumann stability analysis is the same as for some classical schemes, i.e., Leapfrog, Lax, Crank-Nicholson, and DuFort-Frankel. However, the CE/SE method is completely distinct from these methods.

9. Systems of conservation laws are treated in the same way as single conservation laws. The discretized equations for single laws can be transformed directly into those for

systems by replacing scalars with matrices. This property shows the conceptual simplicity of the method.

10. Non-reflective boundary conditions, which can be complicated when utilizing classical methods (using characterics), are very simple to program when using the CE/SE method. This feature is preserved even for problems involving flow discontinuities (shocks).

11. The CE/SE method does not use any directional splitting in the case of multi-dimensional problems. Again, one-dimensional and multi-dimensional problems are treated in the same manner.

12. The method does not require any coordinate mapping. The mesh is built starting from triangles and tetrahedrons, which can be used in both structured and unstructured grids.

13. The conceptual simplicity of the codes developed by using the CE/SE method makes them easy to vectorize and parallelize. Thus, the codes can be adapted to advanced computer systems with little programming effort. In this work, this feature has not been used.

Note that the method is limited to time-dependent equations. Steady state results, such as those discussed in this work, can be obtained only after the stabilization of the unsteady solution starting from initial conditions.

3. 2. One-dimensional problems

First, the method is applied to one-dimensional (1D) problems. The Reynolds equation is two-dimensional (2D), however the simplified 1D case can be a good approximation for long bearings. In these cases variations along the bearing axial

direction are taken to be small compared to property variations in circumferential direction, and thus considered negligible.

3. 2. 1. Equations

The one dimensional, transient Reynolds equation, written for a Newtonian compressible fluid in laminar flow, is

$$\frac{\partial \rho h}{\partial t} + \frac{\partial}{\partial x}\left(\frac{\rho h V}{2} - \frac{\rho h^3}{12\mu}\frac{\partial p}{\partial x} \right) = 0 \ . \tag{3. 1}$$

Using Elrod's formulation [Elrod, 1981], Eq. (3.1) can be written in terms of the non-dimensional density, θ, as

$$\frac{\partial h\theta}{\partial t} + \frac{\partial}{\partial x}\left(\frac{h\theta V}{2} - g_c \frac{\beta' h^3}{12\mu}\frac{\partial \theta}{\partial x} \right) = 0 \, . \tag{3. 2}$$

Equation (3. 2) is the one-dimensional form of Eq. (2.40).

A more suitable form of Eq. (3. 2) for the numerical formulation can be obtained using a new variable *u*, which is the product of the fluid film thickness and the non-dimensional density, i.e.,

$$u = h\theta \, . \tag{3. 3}$$

In terms of *u*, the Reynolds equation can be written as

$$\frac{\partial u}{\partial t} + \frac{\partial f}{\partial x} = 0 \, , \tag{3. 4}$$

where the flux *f* is

$$f = a u - b\frac{\partial u}{\partial x} \, , \tag{3. 5}$$

and the coefficients *a* and *b* are

$$a = \frac{V}{2} + g_c \frac{\beta h}{12\mu} \frac{\partial h}{\partial x}, \tag{3. 6}$$

$$b = g_c \frac{\beta h^2}{12\mu}.$$

Both coefficients *a* and *b* are functions of space variable *x*. If the geometry is time dependent, $h = h(x,t)$, then coefficients *a* and *b* are also time dependent. These coefficients are considered constants on the surface of a grid conservation element *CE*-, *CE*+ (see Fig. 3. 1), but they change when passing from one element to another, and from on time step to the next.

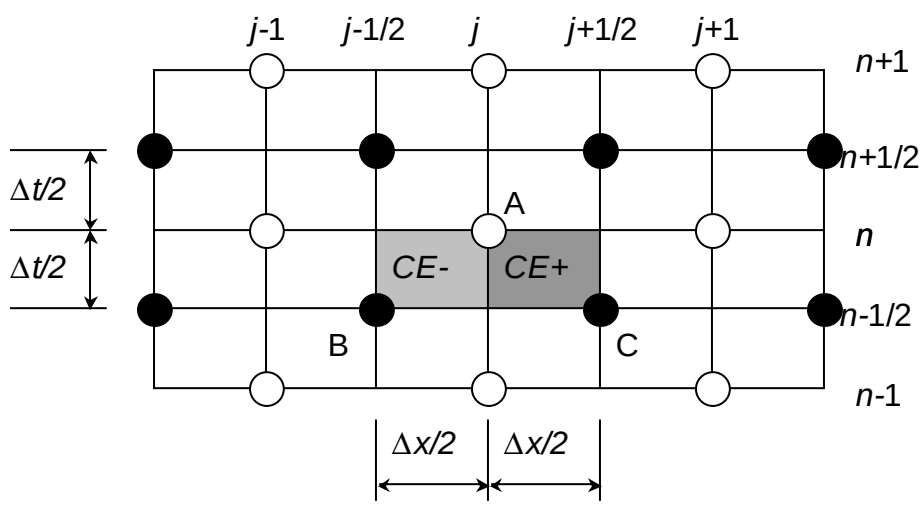

Fig. 3. 1 – Uniform space-time mesh

A first order Taylor series for the unknown function *u* about a generic expansion point $O(x_0, t_0)$ is

$$u \cong u_0 + (u_x)_0 (x - x_0) + (u_t)_0 (t - t_0), \tag{3. 7}$$

where the time derivative can be written using Eq. (3.4), as

$$(u_t)_0 = -\left(\frac{\partial f}{\partial x}\right)_0 . \tag{3. 8}$$

The flux, *f*, can be written as a function of the unknown functions *u* and u_x, i.e., $f = f(u, u_x)$. Preserving the first order accuracy for the approximation, we may write that,

$$\frac{\partial f}{\partial x} \cong \frac{\partial f}{\partial u} u_x = a\, u_x . \tag{3. 9}$$

Accordingly, Eq. (3. 7) becomes

$$u \cong u_0 + (u_x)_0 (x - x_0) - a_0 (u_x)_0 (t - t_0) . \tag{3. 10}$$

Using the same procedure, function *f* is approximated as

$$f \cong \left(\frac{\partial f}{\partial u}\right)_0 u + \left(\frac{\partial f}{\partial u_x}\right)_0 u_x = a_0 u - b_0 u_x . \tag{3. 11}$$

Considering, as part of the first order approximation, that in the vicinity of the expansion point $O(x_0, t_0)$, $u_x \cong const. = (u_x)_0$, and substituting Eq. (3. 10) into Eq. (3. 11), yields

$$f \cong \underbrace{a_0 u_0 - b_0 (u_x)_0}_{f_0} + a_0 (u_x)_0 (x - x_0) - a_0^2 (u_x)_0 (t - t_0) . \tag{3. 12}$$

3. 2. 2. Uniform grid

Consider a uniform grid at the time steps $n-1$, n, $n+1$ and a uniform grid having the same step length, but shifted a half space step length and a half time step, as shown in Fig. 3. 1. In this figure solid points represent the nodal points at half-time steps and the hollow points represent the nodal points at integer time steps. The method considers that

there are two unknowns for each nodal point: u and u_x. Therefore two equations are derived for each nodal point at the new time step.

The first equation is derived by integrating the governing equation, Eq. (3. 4), over the conservation element *CE*-, i.e.,

$$\int_{x_{j-\frac{1}{2}}}^{x_j} \int_{t^{n-\frac{1}{2}}}^{t^n} \left(\frac{\partial u(x,t)}{\partial t} + \frac{\partial f(x,t)}{\partial x} \right) \mathrm{d}t\mathrm{d}x = 0 . \tag{3. 13}$$

Performing the time integration of the first term, and the space integration of the second term (this is equivalent with applying the divergence theorem to transform the surface integral into a contour integral) yields,

$$\int_{x_{j-\frac{1}{2}}}^{x_j} \left(u^n(x) - u^{n-\frac{1}{2}}(x) \right) \mathrm{d}x + \int_{t^{n-\frac{1}{2}}}^{t^n} \left(f_j(t) - f_{j-\frac{1}{2}}(t) \right) \mathrm{d}t = 0 . \tag{3. 14}$$

Functions u and f can be expressed in linear forms as shown in Eqs. (3. 10) and (3. 12), respectively. For $u^{n-\frac{1}{2}}(x)$ and $f_{j-\frac{1}{2}}(t)$, the expansion point is $\mathrm{B}\left(j-\frac{1}{2}, n-\frac{1}{2} \right)$, while for $u^n(x)$ and $f_j(t)$ the expansion point is $\mathrm{A}(j, n)$. This yields the first equation for the point $\mathrm{A}(j, n)$

$$\begin{aligned} & u_j^n \left(1 + \frac{\Delta t}{\Delta x} a_j^n \right) + (u_x)_j^n \left[-\frac{\Delta x}{4} - b_j^n \frac{\Delta t}{\Delta x} + \left(a_j^n \right)^2 \frac{\Delta t^2}{4\Delta x} \right] = \\ & u_{j-\frac{1}{2}}^{n-\frac{1}{2}} \left(1 + \frac{\Delta t}{\Delta x} a_{j-\frac{1}{2}}^{n-\frac{1}{2}} \right) + (u_x)_{j-\frac{1}{2}}^{n-\frac{1}{2}} \left[\frac{\Delta x}{4} - b_{j-\frac{1}{2}}^{n-\frac{1}{2}} \frac{\Delta t}{\Delta x} - \left(a_{j-\frac{1}{2}}^{n-\frac{1}{2}} \right)^2 \frac{\Delta t^2}{4\Delta x} \right]. \end{aligned} \tag{3. 15}$$

The second equation is derived by integrating the governing equation over the conservation element *CE*+, i.e.,

$$\int_{x_j}^{x_{j+\frac{1}{2}}} \int_{t^{n-\frac{1}{2}}}^{t^n} \left(\frac{\partial u(x,t)}{\partial t} + \frac{\partial f(x,t)}{\partial x} \right) \mathrm{d}t\mathrm{d}x = 0 \,. \tag{3. 16}$$

Again performing the time integration of the first term and the space integration of the second term yields,

$$\int_{x_j}^{x_{j+\frac{1}{2}}} \left(u^n(x) - u^{n-\frac{1}{2}}(x) \right) \mathrm{d}x + \int_{t^{n-\frac{1}{2}}}^{t^n} \left(f_{j+\frac{1}{2}}(t) - f_j(t) \right) \mathrm{d}t = 0 \,. \tag{3. 17}$$

Writing functions *u* and *f* in the linear forms with the expansion points $\mathrm{B}\left(j+\frac{1}{2},\, n-\frac{1}{2} \right)$ for $u^{n-\frac{1}{2}}(x)$ and $f_{j+\frac{1}{2}}(t)$, and $\mathrm{A}(j,\, n)$ for $u^n(x)$ and $f_j(t)$, yields the second equation for the point $\mathrm{A}(j,\, n)$

$$\begin{gathered} u_j^n \left(1 - \frac{\Delta t}{\Delta x} a_j^n \right) + (u_x)_j^n \left[\frac{\Delta x}{4} + b_j^n \frac{\Delta t}{\Delta x} - \left(a_j^n \right)^2 \frac{\Delta t^2}{4\Delta x} \right] = \\ u_{j+\frac{1}{2}}^{n-\frac{1}{2}} \left(1 - \frac{\Delta t}{\Delta x} a_{j+\frac{1}{2}}^{n-\frac{1}{2}} \right) + (u_x)_{j+\frac{1}{2}}^{n-\frac{1}{2}} \left[-\frac{\Delta x}{4} + b_{j+\frac{1}{2}}^{n-\frac{1}{2}} \frac{\Delta t}{\Delta x} + \left(a_{j+\frac{1}{2}}^{n-\frac{1}{2}} \right)^2 \frac{\Delta t^2}{4\Delta x} \right]. \end{gathered} \tag{3. 18}$$

It should be noted here, as a general rule for the one-dimensional case, that when writing the discrete equations for the two unknowns at the new time step, *n*, three expansion points are considered. These points are: the grid point at the new time step (where the unknowns are calculated), and the two grid points at the old time step that flank the grid point at the new time step. Thus, each segment for which the line integration is performed (as part of the conservation element boundary) uses one and only one of the three expansion points. Each line integral (flux component) is calculated using the linear approximations starting from the respective unique expansion points. This rule

also insures that for a neighboring *CE*, (having a common boundary with the discussed *CE*) the same expansion point is used for the common segment. Therefore, the approximate flux calculated through a boundary segment has the same value when it is calculated using any of the *CE*'s that contain the respective segment.

Adding Eqs. (3. 15) and (3. 18) yields a new equation where the only unknown is u_j^n, i.e.,

$$2u_j^n = u_{j+\frac{1}{2}}^{n-\frac{1}{2}}\left(1-\frac{\Delta t}{\Delta x}a_{j+\frac{1}{2}}^{n-\frac{1}{2}}\right)+u_{j-\frac{1}{2}}^{n-\frac{1}{2}}\left(1+\frac{\Delta t}{\Delta x}a_{j-\frac{1}{2}}^{n-\frac{1}{2}}\right)+$$
$$+\left(u_x\right)_{j+\frac{1}{2}}^{n-\frac{1}{2}}\left[-\frac{\Delta x}{4}+b_{j+\frac{1}{2}}^{n-\frac{1}{2}}\frac{\Delta t}{\Delta x}+\left(a_{j+\frac{1}{2}}^{n-\frac{1}{2}}\right)^2\frac{\Delta t^2}{4\Delta x}\right]+\left(u_x\right)_{j-\frac{1}{2}}^{n-\frac{1}{2}}\left[\frac{\Delta x}{4}-b_{j-\frac{1}{2}}^{n-\frac{1}{2}}\frac{\Delta t}{\Delta x}-\left(a_{j-\frac{1}{2}}^{n-\frac{1}{2}}\right)^2\frac{\Delta t^2}{4\Delta x}\right]. \quad (3.\ 19)$$

The space derivative at the new time step, $\left(u_x\right)_j^n$, does not appear in Eq. (3. 19) because point $\mathrm{A}\left(x_j, t^n\right)$ is the centroid of the segment $\left(x_{j-\frac{1}{2}}^n, x_{j+\frac{1}{2}}^n\right)$, and the unknown function *u* and the flux *f* are considered linear on this segment.

Another way to obtain Eq. (3.19) is to integrate the governing equation, Eq. (3. 4), over the union of the two conservation elements *CE*- and *CE*+, and then follow the same procedure used to determine Eqs. (3. 15) and (3. 16). This shows that the union of the two conservation elements is also a conservation element. Also, this shows again that the flux through the surface of separation between the two conservation elements *CE*- and *CE*+ is the same when it is calculated using either of the two *CE*'s, since the conservation property is preserved by uniting conservation elements.

For the calculation of the second unknown at the new time step, $\left(u_x\right)_j^n$, either Eq. (3. 15) or Eq. (3. 18) can be used, after the calculation of the coefficients a_j^n and b_j^n.

These coefficients can be determined using Eq. (3. 6) once the switch function $(g_c)_j^n$ is determined from Eq. (2. 38). More specifically,

$$(g_c)_j^n = \begin{cases} 1 & \text{when } \theta_j^n \geq 1 \\ 0 & \text{when } \theta_j^n < 1 \end{cases} \tag{3. 20}$$

The explicit character of the algorithm becomes self evident.

In the original form, also known as the "*a*" scheme, the algorithm has no significant damping; hence, it has been found that it can become unstable (after a large number of steps) even for a small time increment. In order to avoid this, the method must have at least some form of artificial dissipation. The authors of the method have proposed two forms: the $a-\varepsilon$ scheme and the $a-\varepsilon-\alpha-\beta$ scheme. Both schemes differ from the original method (also called the *a* form) only in the way the derivatives $(u_x)_j^n$ are calculated.

Let $(u_x^a)_j^n$ be the value of the derivative $(u_x)_j^n$ calculated according to the original (no damping) method. In the $a-\varepsilon$ scheme the values $u^n_{j-\frac{1}{2}}$ and $u^n_{j+\frac{1}{2}}$ are estimated by a Taylor series using the values of the dependent variables at the previous (old) half time step, i.e., $u^{n-\frac{1}{2}}_{j\pm\frac{1}{2}}$ and $(u_x)^{n-\frac{1}{2}}_{j-\frac{1}{2}}$. Let $\left(u^n_{j\pm\frac{1}{2}}\right)_{est}$ be these estimated values. They are calculated according to the following relations,

$$\left(u^n_{j\pm\frac{1}{2}}\right)_{est} = u^{n-\frac{1}{2}}_{j\pm\frac{1}{2}} + \frac{\Delta t}{2}(u_t)^{n-\frac{1}{2}}_{j\pm\frac{1}{2}} = u^{n-\frac{1}{2}}_{j\pm\frac{1}{2}} - \frac{\Delta t}{2} a^{n-\frac{1}{2}}_{j\pm\frac{1}{2}}(u_x)^{n-\frac{1}{2}}_{j\pm\frac{1}{2}}. \tag{3. 21}$$

These expressions are in agreement with the linear approximation in time of the function u. Using these values, a new value for the derivative $(u_x)_j^n$ can be calculated. Let $(u_x^c)_j^n$ be this value. Thus, a second order approximation for the derivative may be written as,

$$(u_x^c)_j^n = \frac{\left(u^n_{j+\frac{1}{2}}\right)_{est} - \left(u^n_{j-\frac{1}{2}}\right)_{est}}{\Delta x}. \tag{3. 22}$$

Finally, in the $a-\varepsilon$ scheme, the new value of the derivative $(u_x)_j^n$ is calculated as a weighted average value of the original method value $(u_x^a)_j^n$ and the estimated value $(u_x^c)_j^n$, i.e.,

$$(u_x^{a-\varepsilon})_j^n = (1-2\varepsilon)(u_x^a)_j^n + 2\varepsilon(u_x^c)_j^n. \tag{3. 23}$$

For $\varepsilon = 0$ the $a-\varepsilon$ scheme reduces to the original method, while for $\varepsilon = 0.5$ the $a-\varepsilon$ scheme does not take into account the values of the derivatives calculated from the original method (that is, from the conservation equations). In order to insure the stability of the method, the values for ε should be within the range $0 < \varepsilon < 1$. Another necessary condition for the stability of the numerical solution, as indicated by the authors of the method, is to insure that the Courant number is less than one for all the grid points and time steps, i.e.,

$$\left(a\frac{\Delta t}{\Delta x}\right)_j^n < 1. \tag{3. 24}$$

This condition was established for one dimensional advection-diffusion problems by means of a von Neumann's stability analysis. The result is common to all explicit methods [Tannehill, Anderson, and Pletcher, 1997]. Because the governing equation, Eq. (3. 4), is highly non-linear, a heuristic stability criterion has been used instead.

Accordingly, a smaller time step than indicated by the condition of Eq. (3. 24) has been used.

In the $a-\varepsilon-\alpha-\beta$ scheme, two new values for the derivative $(u_x)_j^n$ are calculated, using the estimated values $\left(u^n_{j\pm\frac{1}{2}}\right)_{est}$ and also the value u_j^n (calculated as in the *a* scheme)

$$\left(u_x^{\pm}\right)_j^n = \pm 2\frac{\left(u^n_{j\pm\frac{1}{2}}\right)_{est} - u_j^n}{\Delta x}. \tag{3. 25}$$

Using these two values, a nonlinear weighted average is computed

$$\left(u_x^{w}\right)_j^n = \frac{\left|\left(u_x^{+}\right)_j^n\right|^{\alpha}\left(u_x^{-}\right)_j^n + \left|\left(u_x^{-}\right)_j^n\right|^{\alpha}\left(u_x^{+}\right)_j^n}{\left|\left(u_x^{+}\right)_j^n\right|^{\alpha} + \left|\left(u_x^{-}\right)_j^n\right|^{\alpha}}, \tag{3. 26}$$

where the exponent α is a positive value, usually an integer. Finally, the $a-\varepsilon-\alpha-\beta$ scheme calculates the new value of the derivative $(u_x)_j^n$ as a weighted average value between the original method value $\left(u_x^a\right)_j^n$, the estimated value from the $a-\varepsilon$ scheme $\left(u_x^c\right)_j^n$ and the value from the $\alpha-\beta$ scheme $\left(u_x^w\right)_j^n$, i.e.,

$$\left(u_x^{a-\varepsilon-\alpha-\beta}\right)_j^n = (1-2\varepsilon)\left(u_x^a\right)_j^n + (2\varepsilon-\beta)\left(u_x^c\right)_j^n + \beta\left(u_x^w\right)_j^n. \tag{3. 27}$$

Note that for $\beta = 0$ the scheme reduces to the $a-\varepsilon$ scheme, while for $\varepsilon = 0$ or for $2\varepsilon = \beta$ the scheme has no ε type dissipation.

The two forms of artificial dissipation manifest different behavior: the ε type dissipation acts like general, overall damping, effective mainly in the relatively smooth

regions, where the gradients are small, while the $\alpha-\beta$ dissipation suppresses mainly the numerical oscillations that can appear in the vicinity of the high gradient regions.

Consider first the ε type dissipation. Equation (3. 22) can also be written as

$$\left(u_x^c\right)_j^n = \frac{1}{2}\frac{2\left[\left(u^n_{j+\frac{1}{2}}\right)_{est} - u_j^n\right] - 2\left[\left(u^n_{j-\frac{1}{2}}\right)_{est} - u_j^n\right]}{\Delta x} = \frac{\left(u_x^+\right)_j^n + \left(u_x^-\right)_j^n}{2}. \tag{3. 28}$$

This form shows that $\left(u_x^c\right)_j^n$ is in fact the arithmetic average between the left side and right side numerical derivatives at the point (j,n), and hence is diffusive. Note that the left and right side derivatives are not calculated using values of function *u* at grid points at the time step *n*, since $\left(j-\frac{1}{2},n\right)$ and $\left(j+\frac{1}{2},n\right)$ are not grid points (see Fig. 3. 1).

Consider the $\alpha-\beta$ dissipation, given by Eq. (3. 26), with $\alpha=1$. Suppose that the solution tends to have oscillations (wiggles) with a wave length close to the space grid step. In this case the left and right derivatives will have opposite signs, i.e.,

$$\left(u_x^+\right)_j^n\left(u_x^-\right)_j^n < 0 \tag{3. 29}$$

Obviously, using Eq. (3. 26),

$$\left(u_x^w\right)_j^n = 0, \tag{3. 30}$$

which shows that the $\alpha-\beta$ dissipation tends to suppress the oscillations. On the other hand, assume that a discontinuity is present in the field. Without reducing the generality, assume that the discontinuity is in the space interval $\left(j, j+\frac{1}{2}\right)$ and that the function *u* increases through the discontinuity, i.e., $\left(u_j^+\right)_j^n > 0$ and has a large value, while $\left(u_j^-\right)_j^n$ has

a much smaller value. If $\left(u_x^-\right)_j^n < 0$, then $\left(u_x^w\right)_j^n = 0$, which indicates again the tendency to flatten the oscillations (characterized by the change of sign for the gradients). If $\left(u_x^-\right)_j^n > 0$, then the calculated value for the derivative $\left(u_x^w\right)_j^n$ is a positive value between $\left(u_j^-\right)_j^n$ and $2\left(u_j^-\right)_j^n$. Thus, the gradient cannot have more than double the value of the derivative calculated on the side opposite the discontinuity (the left side in this example). This way the gradient is kept at small values, even when discontinuities are present.

For $\alpha > 1$ the same principles apply, only the averaging has a different weighting. Therefore, when Eq. (3. 29) holds, the derivative $\left(u_x^w\right)_j^n$ is not zero, but has a value between $\left(u_x^-\right)_j^n$ and $\left(u_x^+\right)_j^n$. This shows that the nature of the diffusion (through averaging) remains. Also, when $\left(u_x^-\right)_j^n$ and $\left(u_x^+\right)_j^n$ have the same sign but disproportionate values, the amplification power α increases this disproportionality. In this case $\left(u_x^w\right)_j^n$ has a value closer to the derivative on the smaller side than in the $\alpha = 1$ case.

For the one-dimensional problems considered, assuming that artificial dissipation must be the smallest value possible, good convergence and “smooth” solutions have been obtained using relatively small values: $\varepsilon = \beta = 0.1$, $\alpha = 1.0$. For cases in which no discontinuities in the pressure distribution are present, the choice of the artificial damping parameters does not affect in any practical way the results (no significant differences have been observed as long as at least some dissipation is present $\varepsilon \geq 0.01, \beta \geq 0$). For the cases in which the dependent variables have discontinuities, the above-indicated values have been found, through numerical experimentation, to be satisfactory in most cases. Small oscillations of the dependent variables have been observed for different values in

some cases, though the general aspect of the solution has been preserved even for those situations.

Equations (3. 19) and (3. 27) are used to calculate the unknowns u and u_x at the time step n for all integer values of j (shown as hollow points in Fig. 3. 1) starting from the values at the time step $n-\frac{1}{2}$ and non-integer values of j (shown as dark points in Fig. 3. 1). At the next time step, $n+\frac{1}{2}$, the unknowns are calculated at the solid points of the figure, starting from the values at the hollow points and time step n. Therefore, two half time steps are needed in order to return to the initial space grid. This is a characteristic of the CE/SE method. With the price of doubling the computational effort, the unknowns can be calculated at every half time step for all grid points, both solid and hollow. No increase of the accuracy of the solution is obtained in this case, but the final results have better resolution. Also this is a good way to check that the boundary conditions are imposed correctly, since otherwise two different solutions can develop, corresponding to the two sets of grids used.

3. 2. 3. Non-uniform grid

When the grid is not uniform, the equations are different when moving from time step $n-1$ to $n-\frac{1}{2}$ than from time step $n-\frac{1}{2}$ to n. This is the reason that the algorithm is more complex in this case. The algorithm is similar with the one presented for the uniform grid, but some concepts must be applied in a more general manner.

Probably the most comprehensible way to present this case is to consider that the computational domain (segment) is covered by elements, as shown in Fig. 3.2. At the time steps $t^{n-\frac{1}{2}}$ and t^n, the boundaries of the elements are represented by grey points. Next, consider the centroids of these elements, marked with stars (hollow or grey) and letters A, B, …, F. The conservation elements are defined by these points. In Fig. 3. 2 two *CE*'s are shown: *CE*- is defined by the points B and C at the time step $t^{n-\frac{1}{2}}$, and the same points at the time step t^n; *CE*+ is defined by the points C and D at the time step $t^{n-\frac{1}{2}}$, and the same points at the time step t^n. As in the previous case, these two *CE*'s will be used to write the two conservation equations corresponding to the element centered at point C. Consider now the midpoint (centroid) of the segment AC, marked with a black dot and letter B' in Fig. 3. 2. Similarly, C', D', E' can be defined as the midpoints of the segments BD, CE, and DF, respectively. These points will be the expansion, or characteristic points, for the elements which are centered at C, D, and E, respectively. They can coincide with the elements centroids (for example in Fig. 3. 2 point D' is shown to be the same as point D), but in the general case they have different locations. In the uniform grid case, the characteristic points have the same location as the center-points, so that the distinction between them is not necessary (see Fig. 3. 1). The location of the characteristic points can be easily calculated for any grid element (segment), except for the boundary elements. In this case the characteristic points are taken to coincide with the centroids. For example, in Fig. 3. 2, point A' is the same as point A, since the respective element is on the boundary.

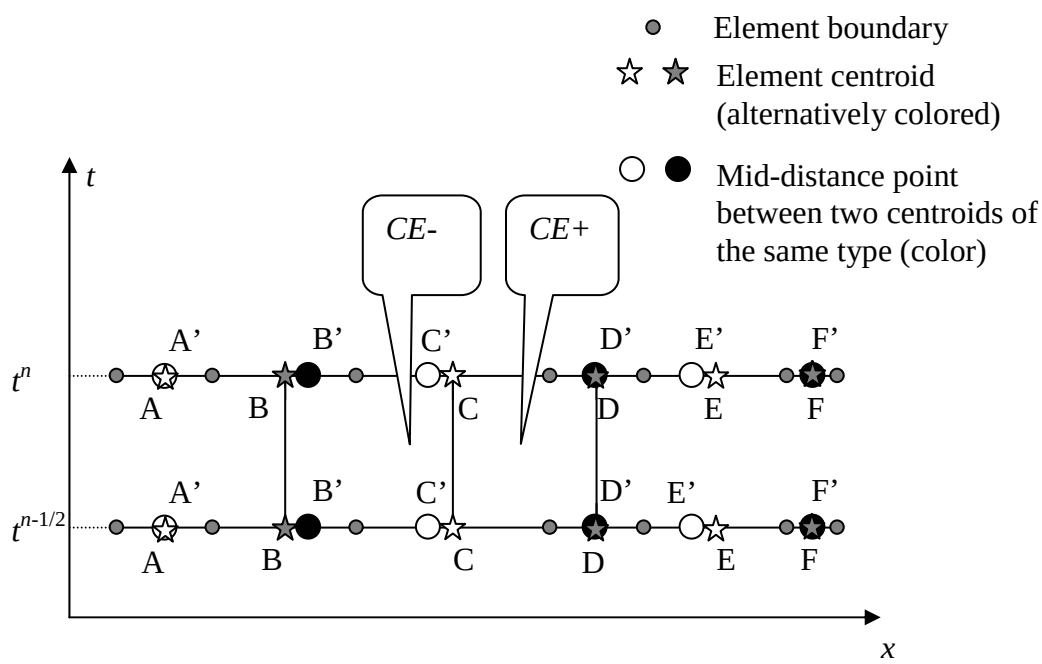

Fig. 3. 2 – Non-uniform space-time mesh

Similarly with the uniform grid case, for each grid point at the new time step t^n, two unknowns must be calculated, i.e., u and u_x. Therefore two equations must be derived. Consider the element centered at point C of Fig. 3. 2. This element has point C' as the representative point, which means that the two unknown values, u and u_x are calculated in point C'.

The first equation is derived by integrating the governing equation Eq. (3. 4) over the conservation element *CE*-, i.e.,

$$\iint_{CE-}\left(\frac{\partial u(x,t)}{\partial t}+\frac{\partial f(x,t)}{\partial x}\right)\mathrm{d}t\mathrm{d}x=0 \tag{3. 31}$$

The surface integral can be transformed into a contour integral using the divergence theorem,

$$\int_{x_B}^{x_C}\left(u^n(x)-u^{n-\frac{1}{2}}(x)\right)\mathrm{d}x+\int_{t^{n-\frac{1}{2}}}^{t^n}\left(f_C(t)-f_B(t)\right)\mathrm{d}t=0 \tag{3. 32}$$

where

$$f_C(t)=f(x,t)\big|_{x=x_C}\text{, and } f_B(t)=f(x,t)\big|_{x=x_B}. \tag{3. 33}$$

Functions *u* and *f* are then expressed in linear forms as in Eqs. (3. 10) and (3. 12), and the integrations are performed. The expansion points are $\mathrm{B}'\left(x_{B'},\, n-\frac{1}{2}\right)$ for the functions $u^{n-\frac{1}{2}}(x)$ and $f_B(t)$, and $\mathrm{C}'(x_{C'},\, n)$ for functions $u^n(x)$ and $f_C(t)$. Therefore, in Eq. (3. 33), the function *u* and *f* are approximated as

$$u^n(x)=u_{C'}^n+(u_x)_{C'}^n(x-x_{C'}) \tag{3. 34}$$

$$u^{n-\frac{1}{2}}(x)=u_{B'}^{n-\frac{1}{2}}+(u_x)_{B'}^{n-\frac{1}{2}}(x-x_{B'}) \tag{3. 35}$$

$$f_C(t)\cong a_{C'}^n u_{C'}^n-b_{C'}^n(u_x)_{C'}^n+a_{C'}^n(u_x)_{C'}^n(x_C-x_{C'})-\left(a_{C'}^n\right)^2(u_x)_{C'}^n(t-t_n) \tag{3. 36}$$

$$f_B(t)\cong a_{B'}^{n-\frac{1}{2}}u_{B'}^{n-\frac{1}{2}}-b_{B'}^{n-\frac{1}{2}}(u_x)_{B'}^{n-\frac{1}{2}}+a_{B'}^{n-\frac{1}{2}}(u_x)_{B'}^{n-\frac{1}{2}}(x_B-x_{B'})-\left(a_{B'}^{n-\frac{1}{2}}\right)^2(u_x)_{B'}^{n-\frac{1}{2}}\left(t-t_{n-\frac{1}{2}}\right) \tag{3. 37}$$

The line (segment) integrals in Eq. (3. 32) can be calculated. Since the functions are linear, each segment integral can be calculated as the product between the value of the function at the mid-point of the segment and the length of the segment. The equation that results is too long to be shown. Nevertheless the character of the equation remains unchanged compared to Eq. (3. 15). Moreover, parts of the equation can be calculated separately when writing the code, so that the long form is not actually necessary.

The second equation is derived by integrating the governing equation over the conservation element *CE*+. Changing the surface integral into a contour integral using the divergence theorem yields,

$$\int_{x_C}^{x_D}\left(u^n(x)-u^{n-\frac{1}{2}}(x)\right)\mathrm{d}x+\int_{t^{n-\frac{1}{2}}}^{t^n}\left(f_D(t)-f_C(t)\right)\mathrm{d}t=0 \tag{3. 38}$$

where

$$f_D(t)=f(x,t)\big|_{x=x_D}\,. \tag{3. 39}$$

As in the previous case, functions *u* and *f* are then expressed in linear forms using Eqs. (3. 10) and (3. 12), and the integrals are taken. The expansion points are $\mathrm{D}'\left(x_{D'},\,n-\frac{1}{2}\right)$ for the functions $u^{n-\frac{1}{2}}(x)$ and $f_D(t)$, and $\mathrm{C}'(x_{C'},\,n)$ for functions $u^n(x)$ and $f_C(t)$ (the last two functions are the same as in the *CE*- case). Consequently,

$$u^{n-\frac{1}{2}}(x)=u_{D'}^{n-\frac{1}{2}}+(u_x)_{D'}^{n-\frac{1}{2}}(x-x_{D'}) \tag{3. 40}$$

$$f_D(t)\cong a_{D'}^{n-\frac{1}{2}}u_{D'}^{n-\frac{1}{2}}-b_{D'}^{n-\frac{1}{2}}(u_x)_{D'}^{n-\frac{1}{2}}+a_{D'}^{n-\frac{1}{2}}(u_x)_{D'}^{n-\frac{1}{2}}(x_D-x_{D'})-\left(a_{D'}^{n-\frac{1}{2}}\right)^2(u_x)_{D'}^{n-\frac{1}{2}}\left(t-t_{n-\frac{1}{2}}\right). \tag{3. 41}$$

Approximations for functions $u^n(x)$ and $f_C(t)$ are given by Eqs. (3. 34) and (3. 36).

The two discrete conservation equations obtained corresponding to the conservation elements *CE*- and *CE*+ form a system with two unknowns: $u_{C'}^n$ and $(u_x)_{C'}^n$. Coefficients $a_{C'}^n$ and $b_{C'}^n$, which appear in Eq. (3. 36), are dependent on the unknown $u_{C'}^n$ through the switch function g_C, so that they cannot be calculated yet. An iterative procedure can be used, starting from the values of the switch function at the old time step,

solving the system for $u_{C'}^{n}$ and $(u_x)_{C'}^{n}$, and then recalculating the value of *g*. Thus, as in the uniform mesh case, the formulation is locally implicit.

The above inconvenience can be easily surpassed imposing the conservation condition over the surface of the reunion of the combined elements *CE*- and *CE*+, i.e.,

$$\iint_{(CE-)\cup(CE+)} \left(\frac{\partial u(x,t)}{\partial t} + \frac{\partial f(x,t)}{\partial x} \right) \mathrm{d}t\mathrm{d}x = 0 \tag{3. 42}$$

Using the divergence theorem yields,

$$\int_{x_B}^{x_D} u^n(x)\mathrm{d}x - \int_{x_B}^{x_C} u^{n-\frac{1}{2}}(x)\mathrm{d}x - \int_{x_C}^{x_D} u^{n-\frac{1}{2}}(x)\mathrm{d}x + \int_{t^{n-\frac{1}{2}}}^{t^n} \left(f_D(t) - f_B(t) \right)\mathrm{d}t = 0 \tag{3. 43}$$

The time and space functions are approximated using the same linear forms and the same expansion points as before. Since at the time step t^n, the same expansion point C' is used for both segments BC and CD, the two segments have been combined into segment BD. However, function $u^{n-\frac{1}{2}}(x)$ is approximated differently for the interval BC, where the expansion point is $\mathrm{B}'\left(x_{B'}, n-\frac{1}{2} \right)$, and for the interval CD, where the expansion point is $\mathrm{D}'\left(x_{D'}, n-\frac{1}{2} \right)$. Therefore, Eq. (3. 35) is used for BC and Eq. (3. 40) is used for CD.

It is readily observed that the unknowns $u_{C'}^{n}$ and $(u_x)_{C'}^{n}$ appear only in the first term of Eq. (3.43). All the other terms are expressed only as functions of the old time step, $t-\frac{1}{2}$, since they are calculated using points $\mathrm{B}'\left(x_{B'}, n-\frac{1}{2} \right)$ and $\mathrm{D}'\left(x_{D'}, n-\frac{1}{2} \right)$ as the expansion points. Because function *u* is approximated using a linear expression, and point C' is the centroid (mid-point) of the segment BD, the first term can be written as

$$\int_{x_B}^{x_D} u^n(x)\mathrm{d}x = u_{C'}^n\left(x_D - x_B\right) \tag{3. 44}$$

Therefore Eq. (3. 43) contains only one unknown, and is purely explicit. After calculating the value for $u_{C'}^n$ from this equation, the switch function g_c can be determined at the new time step. Finally, the gradient at the new time step can be calculated using any of the two conservation equations written for *CE*- or *CE*+. Thus, the *a* form of the algorithm for non-uniform grids is completed.

The $a-\varepsilon$ and the $a-\varepsilon-\alpha-\beta$ schemes are constructed in a manner similar to that of the uniform grid case, but with a difference. The distinction appears because in the general case point C', where the unknowns are calculated, is not the centroid of the segment B'D'. Therefore, a new set of points is considered, B'' and D'' (and of course their corresponding points for the other elements as well), such that C' is the centroid of segment B''D''. The coordinates of points B'' and D'' are calculated translating points B' and D' with a distance equal to the distance between the centroid of segment B'D' and point C'. Therefore,

$$x_{B'',D''} = x_{B',D''} + \left(x_{C'} - \frac{x_{B'} + x_{D'}}{2}\right) \tag{3. 45}$$

It can be easily verified that the centroid of segment B''D'' is point C'.

Similarly with the uniform grid case, Eq. (3. 21), $\left(u^n_{j\pm\frac{1}{2}}\right)_{est}$ must be calculated at the new time step using the correspondent values and derivatives from the old time step. The points where these two values are estimated are B'' and D''. For example,

$$\left(u^{n}_{j-\frac{1}{2}}\right)_{est} = \left(u^{n}_{B''}\right)_{est} = u^{n-\frac{1}{2}}_{B'} + \frac{\Delta t}{2}\left(u_t\right)^{n-\frac{1}{2}}_{B'} + \left(x_{B''} - x_{B'}\right)\left(u_x\right)^{n-\frac{1}{2}}_{B'} =$$
$$= u^{n-\frac{1}{2}}_{B'} + \left(x_{B''} - x_{B'} - \frac{\Delta t}{2} a^{n-\frac{1}{2}}_{B'}\right)\left(u_x\right)^{n-\frac{1}{2}}_{B'} \tag{3. 46}$$

A similar equation can be written for the evaluation of $\left(u^{n}_{j+\frac{1}{2}}\right)_{est} = \left(u^{n}_{D''}\right)_{est}$.

Starting from these two estimated values, and using the procedure described by Eqs. (3. 22), (3. 23), and (3. 25) – (3. 27), yields the $a-\varepsilon$ and $a-\varepsilon-\alpha-\beta$ schemes respectively for non-uniform grids.

A very important feature of the $a-\varepsilon$ and $a-\varepsilon-\alpha-\beta$ schemes is that, as shown previously, the calculated value of the unknown *u* at the new time step still satisfies the conservation on the combined element $CE = (CE-) \cup (CE+)$, even though the gradient u_x is not calculated using this condition. This is probably the main reason that the CE/SE method remains accurate even when artificial dissipation is used. Because the conservation is satisfied over *CE*, a new division can be found,

$$CE = (CE'-) \cup (CE'+)$$

such that conservation is satisfied for each of the two new conservation elements $CE'-$ and $CE'+$.

3. 2. 4. Applications involving slider bearings

In order to determine the performance of the method, several numerical examples were attempted. The results were compared with the results obtained using the Elrod algorithm, as well as the type differencing method, both presented by Vijayaraghavan and

Keith (1989). Only the steady state solutions, obtained through asymptotic time integration, are considered.

Two slider bearing configurations were analyzed: parabolic and double parabolic. The geometry of these bearings is presented in Fig. 3. 3, while the physical conditions are shown in Table 3. 1.

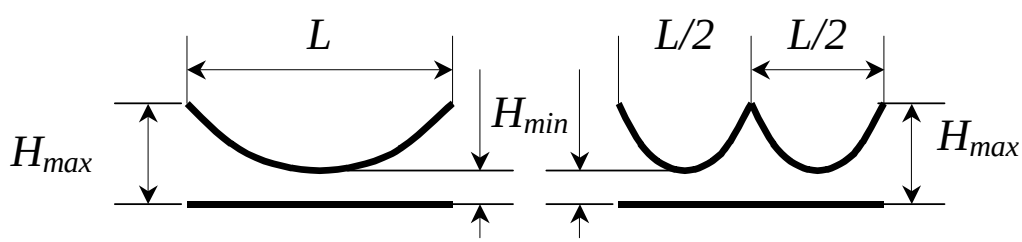

Fig. 3. 3 – Parabolic slider bearing configurations

Table 3. 1

Physical Conditions for Slider Bearings

Parameter	Value	Units
Length	$7.62 \cdot 10^{-2}$	m
Minimum Height	$2.54 \cdot 10^{-2}$	m
Maximum Height	$5.08 \cdot 10^{-2}$	m
Velocity	4.57	m/s
Viscosity	0.039	Pa s
Bulk Modulus (β')	$6.9 \cdot 10^{7}$	N/m^2
Cavitation Pressure (gage)	0	N/m^2

Two boundary conditions at the inlet were considered: the flooded inlet, with $\theta_B = 1.0001$, and the starved inlet, with $\theta_B = 0.55$. Still, these conditions are not sufficient. Two parameters are calculated for each interior element of the grid, the main state function *u*, and its spatial gradient, u_x. Therefore, both of these parameters must be specified or evaluated at the boundaries.

Since at the inlet the value of the main state function $u = h\theta$ is known, only the gradient must be evaluated. The condition used is,

$$(u_x)_1 = (u_x)_3, \tag{3. 47}$$

where the third point in the grid is the same kind as the point on the boundary (they are both “solid” or “hollow” points) [Chang, et. al., 1997].

At the exit, both the value of the main state function *u* and its derivative must be calculated from the field. The following conditions are used,

$$\begin{aligned} u_M &= u_{M-2}, \\ (u_x)_M &= (u_x)_{M-2} \end{aligned} \tag{3. 48}$$

where *M* is the number of the element on the exit boundary. Since these conditions are not evident, consider a uniform grid (or at least with the last three elements: *M*-2, *M*-1, and *M* separated by the same space step), as in Fig. 3. 4.

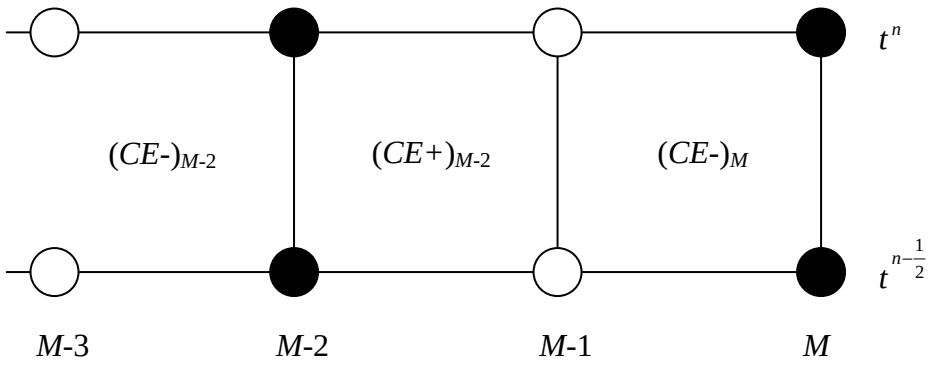

Fig. 3. 4 – Conservation elements for the boundary condition at the exit

Consider now the governing equation, Eq. (3. 4), integrated of the surfaces $(CE+)_{M\text{-}2}$ and $(CE\text{-})_M$. Over one half time step, from $t^{n-\frac{1}{2}}$ to t^n, the algorithm goes from hollow points to solid points. One equation obtained from $(CE\text{-})_M$ is not enough to calculate both unknowns u_M^n and $(u_x)_M^n$. However, since the values u_{M-2}^n and $(u_x)_{M-2}^n$ satisfy the equation obtained for $(CE\text{-})_{M\text{-}2}$, they will also satisfy the equation for $(CE\text{-})_M$. The reason for this is that, because Eq. (3. 48) is imposed, it is easily seen that the equations obtained for the above conservation elements become identical. Therefore, the values obtained using Eq. (3. 48) are valid, i.e., satisfy the conservation condition. The same reasoning can be used when the grid is not uniform, but then element M is added outside the domain (added as a ghost element) with the same size as element M-1. An important fact is that, since at the exit of the slider bearings the flow is cavitated, and the governing equation is hyperbolic, the value at the exit boundary does not influence the rest of the computational domain (as long as the cavitation condition holds).

As for the initial condition, the constant fractional film content (and implicitly a constant pressure) distribution has been considered,

$$\theta_j^0 = \theta_B = const. \tag{3. 49}$$

Consequently, at the initial time

$$u_j^0 = \theta_j^0 h_j \ , \ (u_x)_j^0 = \theta_j^0 (h_x)_j \ . \tag{3. 50}$$

In order to shorten the computational time for finer grids when the same case had already been solved for a coarser grid, an interpolation using the results obtained for the coarser grid was used.

Figures 3. 5 and 3. 6 show the pressure distribution and the fractional film content distribution obtained for the parabolic slider with a flooded inlet compared with the results obtained from Elrod's algorithm and from the type-differencing algorithm developed by Vijayaraghavan and Keith, 1989. Figure 3. 5 shows that the pressure distribution obtained with CE/SE method is situated between the pressures obtained with the type-differencing method and the pressures obtained with Elrod’s algorithm. For the type difference method compressibility effects were included in the full film shear flow term. It should be noted the results obtained with Elrod’s algorithm and the type-difference are the same when compressibility effects in the full film region are not included. Because the differences between the CE/SE method, Elrod’s algorithm and the type-differencing algorithm, respectively, are relatively small (under 3%), it may be concluded that the three methods are in good agreement for this test case. In Fig. 3. 6 the differences between the three methods are even smaller (because there are no practical differences between Elrod’s algorithm and type-differences, only one of them is presented in this figure).

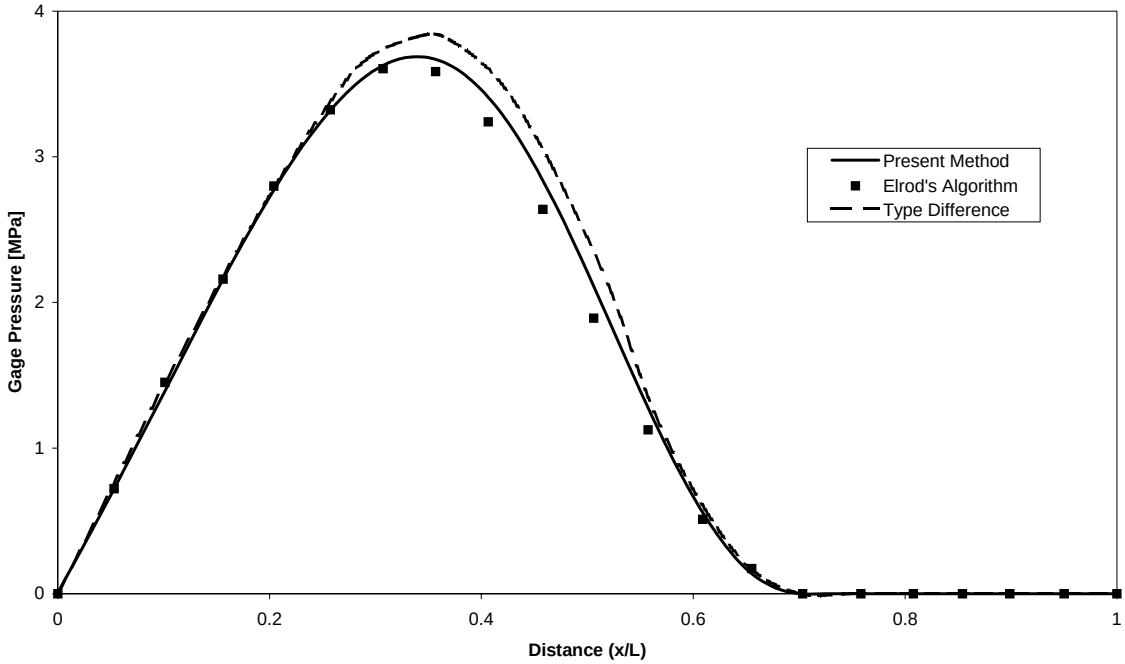

Fig. 3. 5 – Pressure distribution in a parabolic slider with flooded inlet

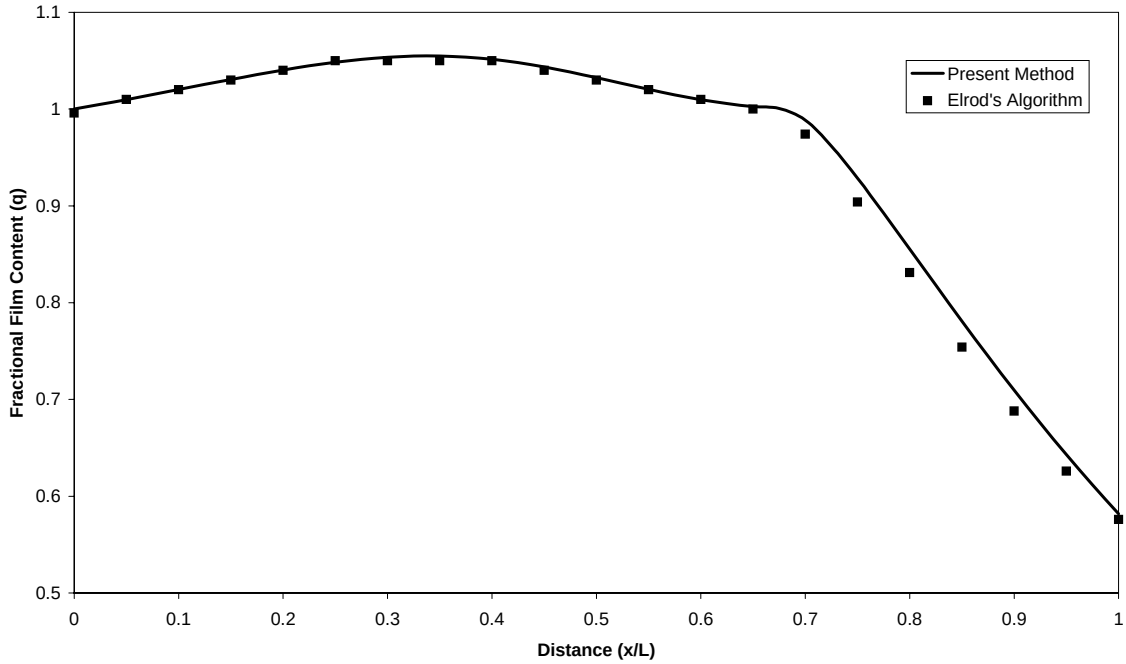

Fig. 3. 6 – Fractional film content distribution in a parabolic slider with flooded inlet

A more difficult case is that of the same parabolic slider with a starved inlet. The difficulty of this case resides in the fact that the reformation of the fluid film is more sensitive to numerical errors than the rupture of the film. Figures 3. 7 and 3. 8 show the results for the slider bearing with a starved inlet for different uniform grids compared with those found in the same work. Figure 3. 7 shows that the type-differencing method, compared with Elrod's algorithm, predicts the same cavitation boundaries, although the pressures are smaller (the maximum pressure is about 6% smaller). When the CE/SE method is used, the pressures are found to be even smaller (the maximum pressure is about 26% smaller). Furthermore, in this case the cavitation boundaries, especially the fluid film formation front, are quite different. However, probably the most important distinction between the results obtained with the present method and those obtained with previous methods resides in the pressure distribution in the vicinity of the fluid film formation front. As can be seen, the results obtained with the CE/SE method show a sharp discontinuity in the pressure (or θ) distribution at the fluid film reformation point. Fig. 5 also shows that there are no significant changes in the results when the grid has more than 161 points. This number may appear relatively large, but consider also that the algorithm actually calculates only half of the grid points at each time step. The differences between the results obtained with different grid steps are less evident for the fractional film content θ. This is the reason that Fig. 3. 8 shows data obtained with CE/SE method using 41, 81 and 1001 grid points.

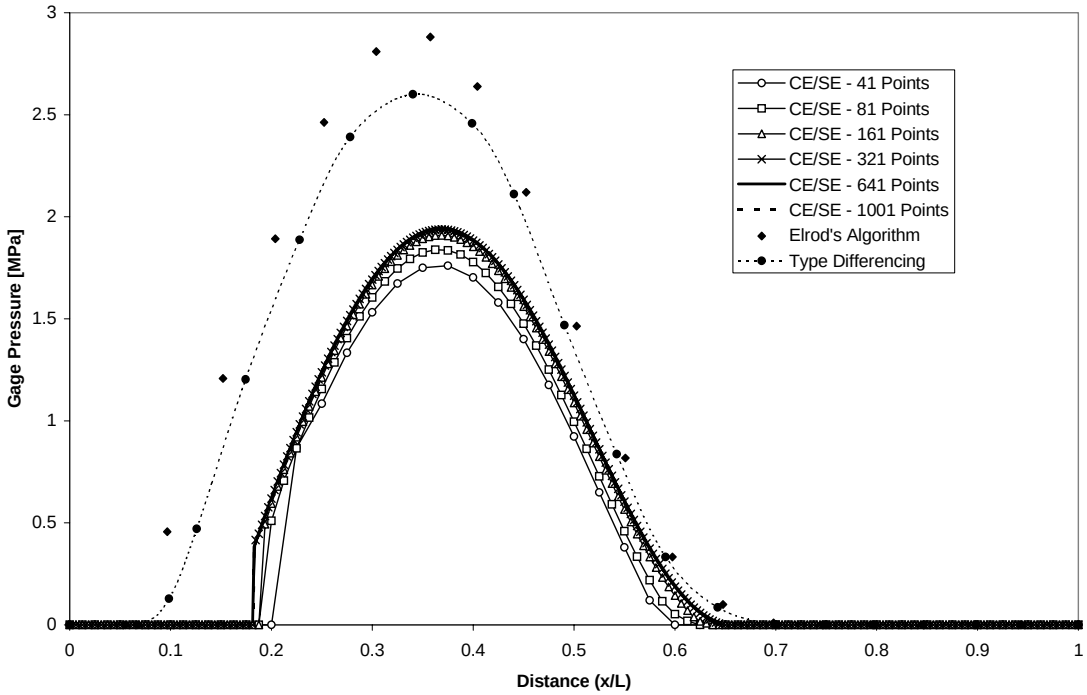

Fig. 3. 7 – Pressure distribution in a parabolic slider with starved inlet

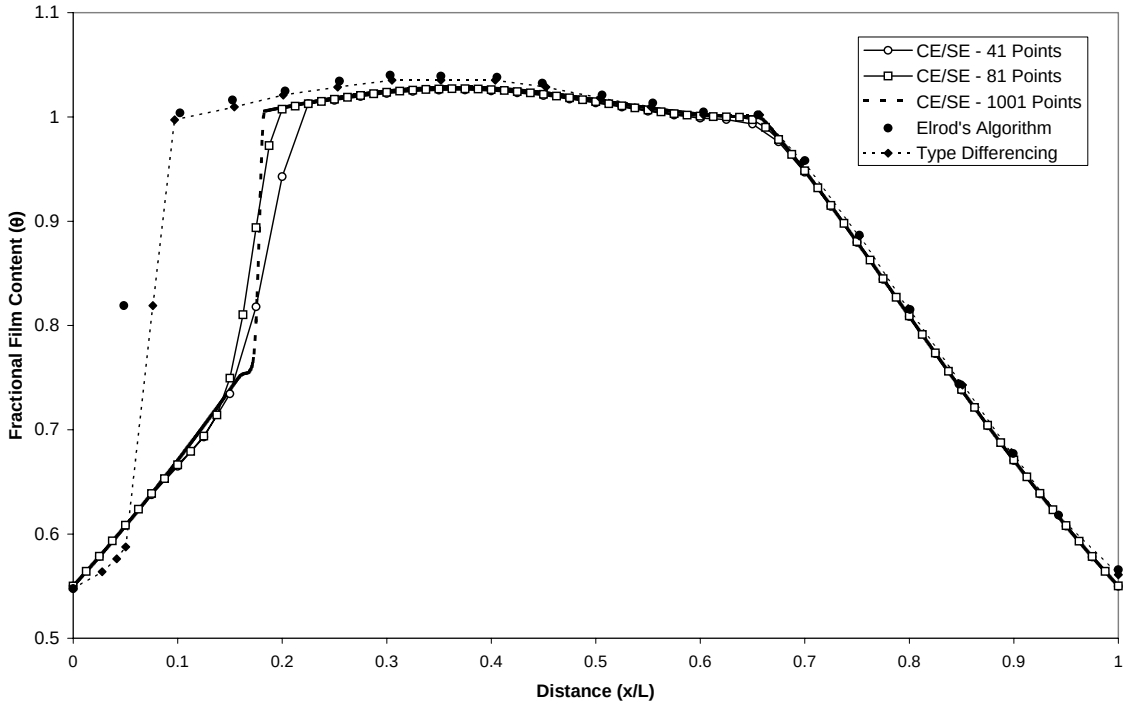

Fig. 3. 8 – Fractional film content distribution in a parabolic slider with starved inlet

As shown by Vijayaraghavan, Keith and Brewe (1990), a conceptual analogy between the transonic flow and the cavitated bearing exists. This analogy is due to the mathematical nature of the steady state forms of the governing equations within different regions. Either flow can be elliptic (full film region for the bearing, subsonic region for the transonic flow, respectively) or hyperbolic (cavitated region for the bearing, supersonic region for the transonic flow, respectively). Thus, the sonic line is analogous to the film rupture, while the shock wave and the film reformation are also similar to each other.

It is well known, as shown by Tannehill, Anderson and Pletcher (1997), that the position of the shock wave (supersonic-subsonic transition) is more difficult to predict numerically than the sonic line position (subsonic-supersonic transition). Previous numerical methods used to calculate cavitated bearings could not capture in a proper way the film reformation because, as for the shock wave, the pressure (and also the fractional film content θ) has a discontinuity at that location. Therefore, a numerical algorithm that can capture this discontinuity without dissipation or dispersion is necessary; the CE/SE is such an algorithm. This method, in the way it has been applied here, uses equations derived by integrating Reynolds equation in space and time, equations written in conservative form. For that reason CE/SE is able to capture discontinuities, while standard methods that use finite differences cannot, even if they start from the same equation and even if the space step is extremely small.

For the double parabolic slider bearing with a flooded inlet the results show similar characteristics at the fluid film reformation point as before, as can be seen in Fig. 3. 9. However, because the pressure gradients are higher (due to the higher slope of the

geometric configuration) compared to the previous configuration, the fluid film reformation front is less visible in this case. The same effect seen before, i.e., a reduced maximum pressure after the fluid film reformation, is observed for this configuration as well. The difference between the second peak pressures calculated with the two different methods is about 10%. Note that with the type-differencing method, the second maximum pressure is 12% larger than the first peak pressure. Physically this does not seem possible to obtain larger pressures with the same geometry repeated in cascade form (the mass flow is the same in both parabolic stages). For the same case, the code using the CE/SE method predicted that the second peak pressure is about 0.1% smaller than the first peak pressure. The difference between the two peak pressures obtained with the CE/SE method indicates that a there is dissipation in the numerical system, but this dissipation is small.

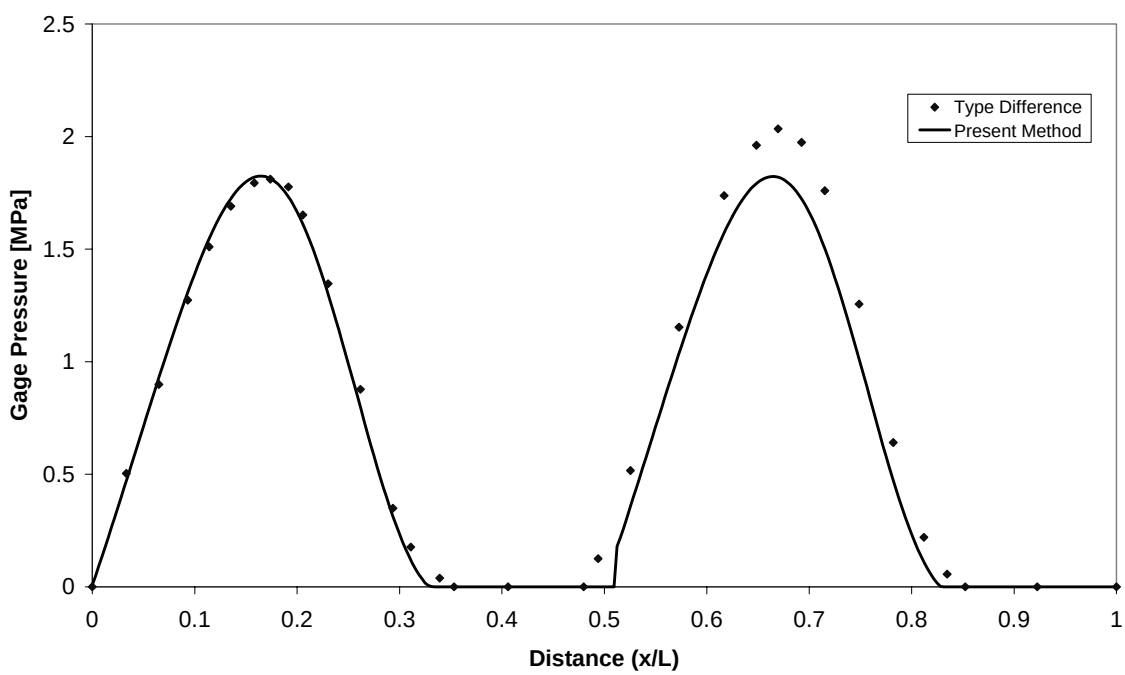

Fig. 3. 9 – Pressure distribution in a double parabolic slider with flooded inlet

3. 2. 5. Applications for Journal Bearings

A journal bearing geometry, as shown in Fig. 3. 10, was considered in order to further study the CE/SE method applied to one dimensional fluid film bearing problems. The non-dimensional form of the governing equation in this case is the same as in the previous cases, Eqs. (3. 4) and (3. 5), with

$$
\begin{aligned}
a &= \frac{1}{4\pi} + g\frac{\overline{\beta'}\overline{h}}{48\pi^2}\frac{\partial \overline{h}}{\partial \overline{x}}, \\
b &= g\frac{\overline{\beta'}\overline{h}^2}{48\pi^2}, \\
u &= \overline{h}\theta.
\end{aligned}
\tag{3. 51}
$$

where

$$
\begin{aligned}
\overline{h} &= \frac{h}{C} = 1 - \frac{e}{C}\cos\phi, \\
\overline{x} &= \frac{x}{2\pi R}, \\
\overline{\beta}' &= \beta'\frac{C^2}{R^2\mu\omega}.
\end{aligned}
\tag{3. 52}
$$

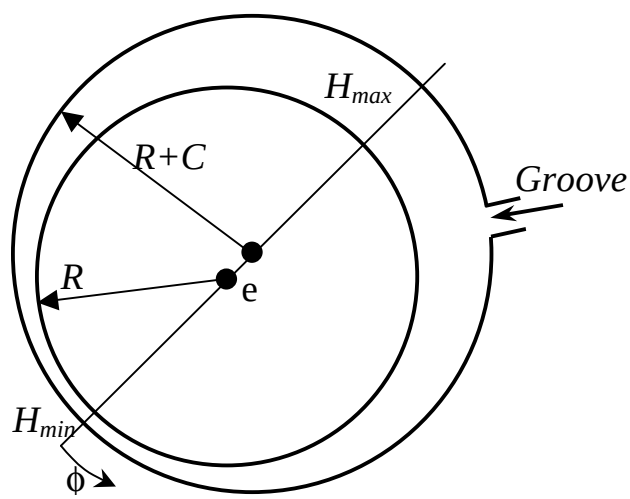

Fig. 3. 10 – Journal bearing geometry

The operating conditions are indicated in Table 3. 2. At the groove, the lubricant inlet is assumed to be flooded with $\theta = 1.0001$.

Table 3. 2 **Physical conditions for a grooved journal bearing**		
Parameter	Value	Units
Grooves	1, 2	-
$\overline{\beta'}$	40	-
Relative eccentricity ($\varepsilon = e/C$)	0.6	-
Cavitation pressure (gage)	0	N/m^2

Periodic boundary conditions are imposed at the two ends of the computational domain. They were considered using ghost elements at both ends, each ghost element being paired with the first interior element on the other side of the computational domain. The values for the unknowns, u and u_x, for these ghost elements were set so as to equal the values calculated at the same time step for the corresponding paired elements.

Figures 3. 11 and 3. 12 show the results obtained for a bearing with a single groove positioned at an angle $\phi = 100^0$ relative to the minimum thickness location. The results for the type-differencing method have been obtained by running the original code written by Vijayaraghavan [1989]. For this problem, the location of the fluid film reformation boundary, and implicitly the discontinuities in the pressure and fractional film content distributions, are imposed through a boundary condition (the presence of the

inlet groove). Therefore the differences between the type-differencing method and the present method for this case are not very significant. Both the fractional film content (Fig. 3. 11) and pressure distribution (Fig. 3. 12) follow the same trend and are almost identical over most of the circumference of the journal bearing. However, the type-differencing algorithm predicts a maximum pressure that is 12% smaller than the value predicted by the CE/SE method (this peak pressure difference corresponds to a difference of only 2.6% for the peak fractional film content θ). This difference has two probable causes. First, the CE/SE method has very small dissipation, especially when small values for the artificial dissipation parameters (ε, β) are used. Because the dissipation is low, larger values for the fractional film content (the main variable in the governing equation) and implicitly for the pressure are to be expected compared to those obtained using the type-differencing method. Indeed, for the case illustrated, the values $\varepsilon = 0.5$ and $\beta = 1.0$ were used, whereas when the values $\varepsilon = 0.02$ and $\beta = 0.1$ were used, the difference between the predicted peak pressures with the two methods increased to 15%. This consideration is valid only for the cases where no other causes, such as the presence of sharp discontinuities in the field, affect the problem. The second cause is the fact that the type-differencing code solves a two dimensional problem (a finite length bearing with large, but finite, length-diameter ratio), while the code based on the CE/SE method solves the pure one-dimensional problem.

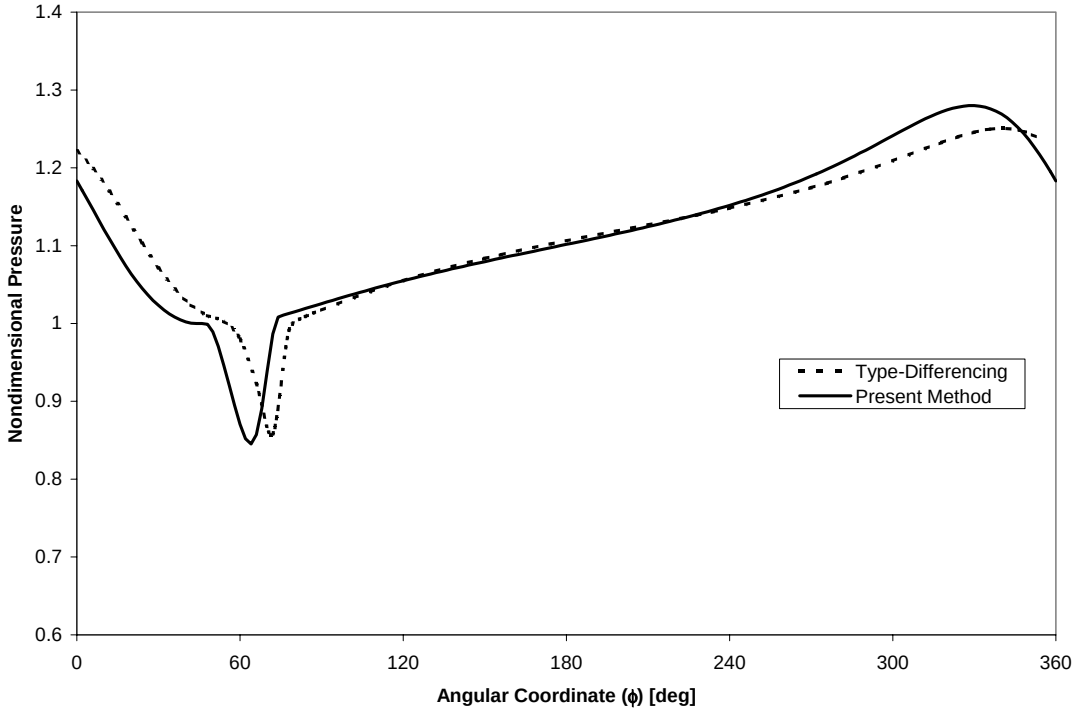

Fig. 3. 11 – Fractional film content distribution in a journal bearing with one groove

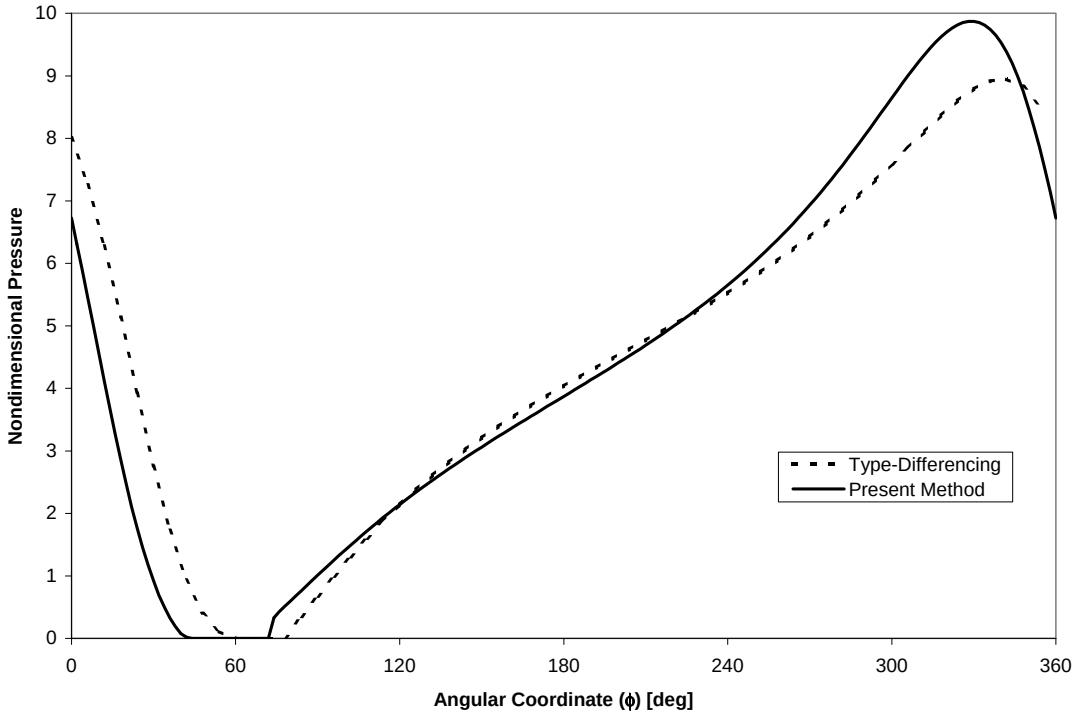

Fig. 3. 12 – Pressure distribution in a journal bearing with one groove

The pressure distribution in the same journal bearing without fluid supply is illustrated in Fig. (3. 13). At the initial instant in time, the bearing was considered to be flooded ($\theta = 1.0001$). Small values for the artificial dissipation parameters were used ($\varepsilon = 0.02$ and $\beta = 0.1$). The figure shows again that the method can naturally capture the discontinuity as a sharp front (full fluid film reformation).

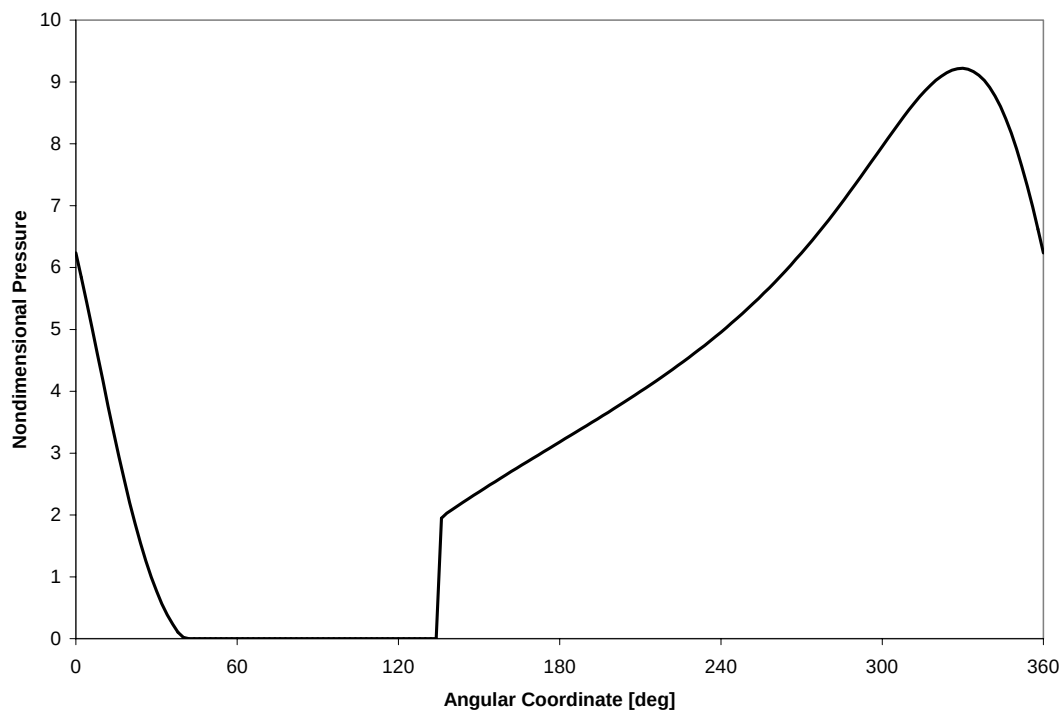

Fig. 3. 13 – Pressure distribution in a journal bearing without grooves

The code was run tested for a journal bearing with two grooves positioned at the angles $\phi_1 = 60^0$ and $\phi_2 = 240^0$ relative to the minimum thickness location. At the grooves the lubricant inlet is assumed to be flooded with $\theta = 1.0001$. The results are presented in Figs. (3. 14) and (3. 15). The presence of the second groove at $\phi_2 = 240^0$

imposes a low value for the pressure at that location, which in turn, compared with the previous cases, influences in a negative way the pressure distribution for a large circumferential region of the bearing.

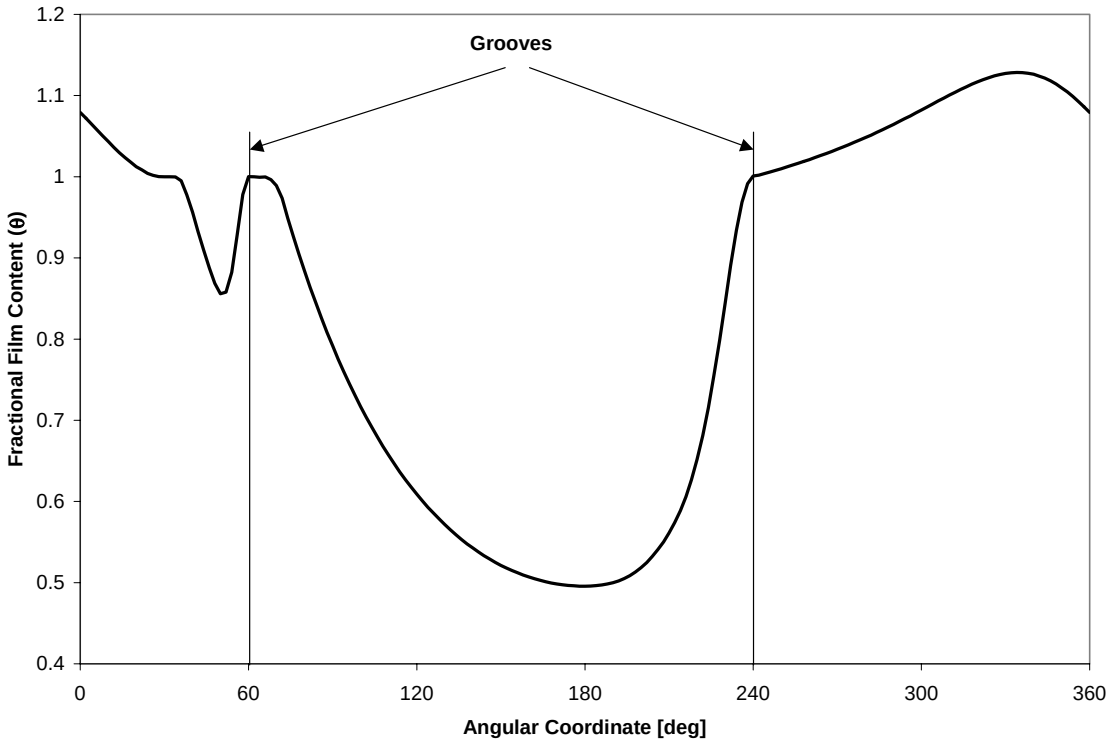

Fig. 3. 14 – Fractional film content in a journal bearing with two grooves

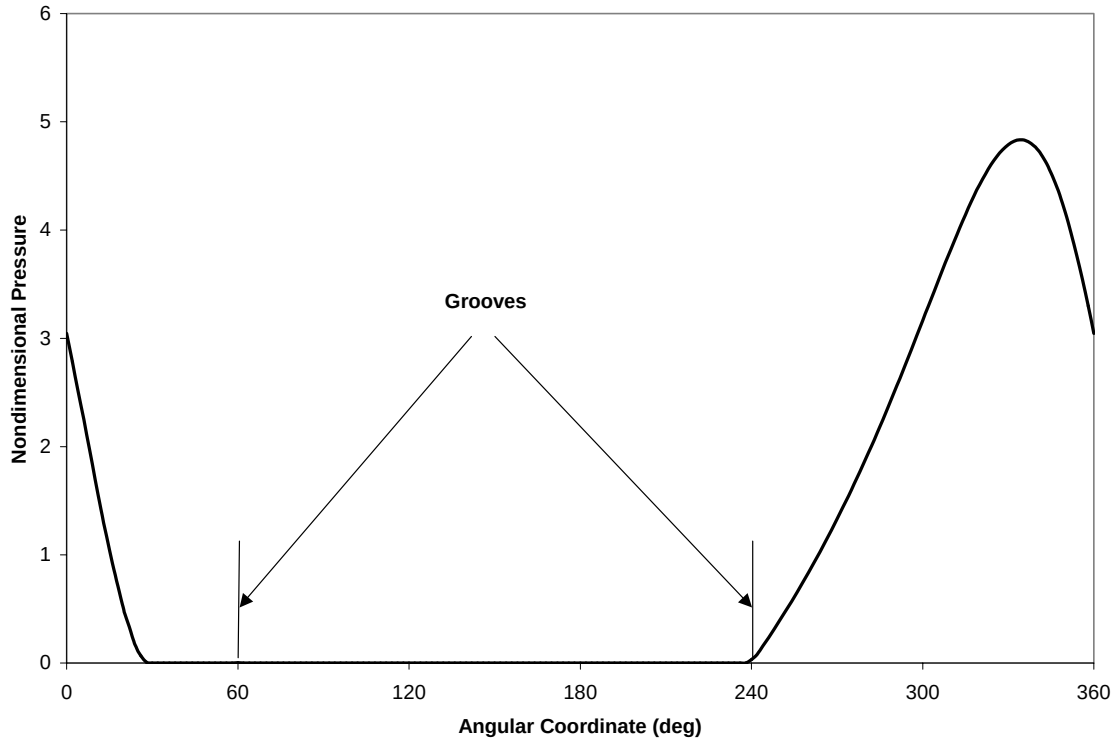

Fig. 3. 15 – Pressure distribution in a journal bearing with two grooves

3. 2. 6. Discontinuities at the fluid film reformation

Similar to the reasoning presented in Chapter 2, Eqs. (2. 25) – (2. 30), consider a stationary cavitated region in a one-dimensional bearing as in Fig. (3. 16). The cavitation region lies between surfaces 1 and 2 (or 3). Surfaces 2 and 3 are each on one side of the film reformation boundary, and they are infinitely close to each other (the distance between them is considered to be zero). Surface 1’ is a surface inside the cavitated region.

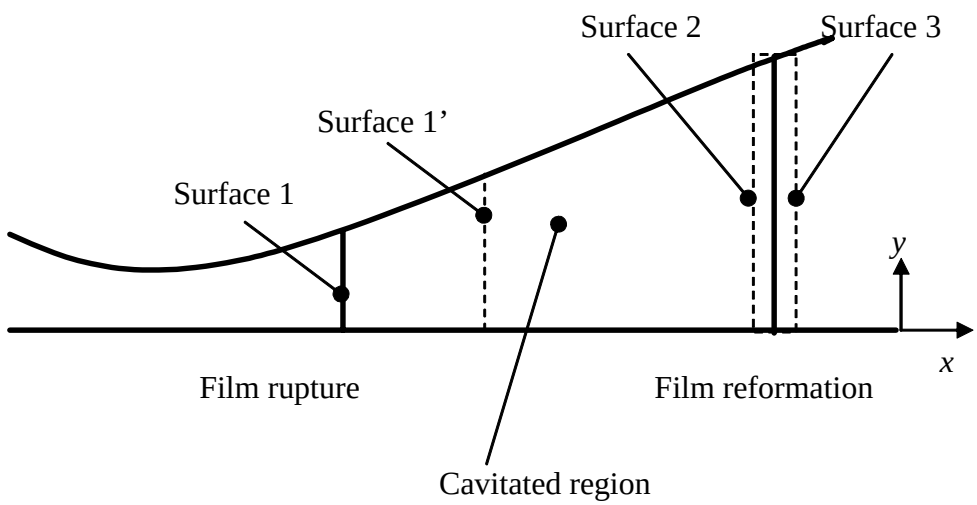

Fig. 3. 16 – One-dimensional cavitated fluid film

The mass conservation principle in the cavitated region is

$$\rho_c \theta_1 h_1 \frac{V}{2} = \rho_c \theta_2 h_2 \frac{V}{2}. \tag{3. 53}$$

At the film rupture point there are no discontinuities, i.e. $\theta_1 = 1.0$. Simplifying Eq. (3. 53) with the factor $\rho_c \frac{V}{2}$ yields,

$$\theta_2 = \frac{h_1}{h_2}. \tag{3. 54}$$

Considering surfaces 1' and 2, Eq. (3. 54) becomes

$$\theta_2 = \frac{\theta_1' h_1'}{h_2}. \tag{3. 55}$$

Equation (3. 55) is useful when the fractional film content is known at a location inside the cavitated region. The fractional film content θ has a value $\theta \geq 1$ in the full film regions and has a value $\theta < 1$ in the cavitated regions. Because surface 2 is on the interior side of the boundary of the cavitated region, $\theta_2 \leq 1$, it is required that:

- the reformation point must have a film thickness h_2 so that $h_2 \geq h_1$, or $h_2 \geq \theta_1' h_1'$
- when $h_2 > h_1$ or $h_2 > \theta_1' h_1'$ there is a discontinuity in the fractional film content distribution at the reformation point ($\theta_2 = \frac{h_1}{h_2} = \frac{\theta_1' h_1'}{h_2} < 1$ immediately before the film reformation and $\theta_3 = 1.0$ immediately after the reformation surface)

The continuity equation written for a control volume that contains the reformation surface and has a very small thickness (Fig. 3. 16, shows the volume between surfaces 2 and 3) is

$$\rho_c \theta_2 h_2 \frac{V}{2} = \rho_c \left[h_3 \frac{V}{2} - \frac{h_3^3}{12\mu} \left(\frac{\partial p}{\partial x} \right)_3 \right] \tag{3. 56}$$

Neglecting the film thickness variation across the control volume $h_2 = h_3$ (because the distance between surfaces 2 and 3 is considered zero), simplifying by canceling the product $\rho_c h_2$, and rearranging terms yields a condition similar to Eq. (2. 29),

$$\left(\frac{\partial p}{\partial x} \right)_3 = \frac{6\mu V (1 - \theta_2)}{h_2^2} \tag{3. 57}$$

In terms of the non-dimensional variables used for journal bearings,

$$\begin{aligned} \bar{p} &= p \frac{C^2}{R^2 \mu \omega}, \\ \bar{h} &= \frac{h}{C}, \\ \bar{x} &= \frac{x}{2\pi R}, \end{aligned} \tag{3. 58}$$

equation (3. 57) becomes,

$$\left(\frac{\partial \bar{p}}{\partial \bar{x}} \right)_3 = \frac{12\pi (1 - \theta_2)}{\bar{h}_2^2} \tag{3. 59}$$

This equation shows that the presence of a fractional film content discontinuity where $\theta_2 < 1$ determines the existence of a positive pressure gradient immediately after the reformation point

$$\left(\frac{\partial p}{\partial x}\right)_3 > 0 . \tag{3. 60}$$

Note that at the rupture point and throughout the entire cavitation region the pressure gradient is null.

Applying the momentum conservation equation to the same control volume (the momentum conservation is not included explicitly in the Reynolds equation) yields

$$\int_0^{h_2} \theta_2 \left(V \frac{y}{h_2}\right)^2 dy - \int_0^{h_2} \left[V \frac{y}{h_2} + \frac{1}{2\mu}\left(\frac{\partial p}{\partial x}\right)_3 y(y - h_2)\right]^2 dy = \frac{(p_2 - p_3)h_2}{\rho_c} \tag{3. 61}$$

Performing the integrations and considering the expression of the pressure gradient, Eq. (3. 57), yields

$$\Delta p = p_3 - p_2 = \frac{\rho_c V^2}{30}\left(4 - 3\theta_2 - \theta_2^2\right) = \frac{\rho_c V^2}{30}(1 - \theta_2)(4 + \theta_2). \tag{3. 62}$$

In non-dimensional variables, Eq. (3. 62) is

$$\Delta \overline{p} = \frac{\rho_c C^2 \omega}{\mu} \cdot \frac{(1 - \theta_2)(4 + \theta_2)}{30} \tag{3. 63}$$

When $\theta_2 < 1$ the last equation shows that there exists a pressure jump across the reformation surface $\Delta p > 0$. The pressure discontinuity is larger when the fluid film θ_2 content is smaller. The location of the reformation front cannot be predicted theoretically using the considerations shown above.

Using the above considerations, the one-dimensional results with discontinuities can now be reviewed in a different light. Consider first the results shown in Figs. (3. 7)

and (3. 8). At the inlet the fractional film content is in this case $\theta_{inlet} = 0.55$. The location of the reformation front with no discontinuities, $\theta_2 = 1$, can be calculated using Eq. (3. 55), i.e., for $\theta_{inlet} = \theta_1' = 0.55$,

$$h_{2\,\text{no discontinuity}} = \theta_{inlet} h_{inlet} = 0.55 h_{\max} . \tag{3. 64}$$

This value corresponds to a location

$$\frac{x_{2\,\text{no discontinuity}}}{L} = 0.342 . \tag{3. 65}$$

However, the reformation point is at a different location, with higher fluid film thickness, as determined using both numerical methods. As a consequence, discontinuities must be present at the reformation front, and they are predicted using the CE/SE method, while the more classical method fails to do so. Using the predicted location(s) of the reformation point, the values of the fractional film content after the reformation, Eq. (3. 55), pressure gradient, Eq. (3. 57), and pressure, Eq. (3. 62), have been checked against the values obtained from the code, and they agree with each other. Similar considerations are valid for all the other cases where discontinuities at the reformation front have been observed, except for the cases where the reformation is dictated by the presence of a supply system.

3. 3. Two-dimensional problems

The two-dimensional, transient Reynolds equation, written for a Newtonian fluid, in Elrod's formulation is given by Eq. (2. 40). Note that, from the point of view of the number of dimensions used, the Reynolds equation cannot be more than two-dimensional.

3. 3. 1. Numerical formulation

A more suitable form of Eq. (2. 40) for the numerical formulation is obtained using the same variable as for the one-dimensional case, Eq. (3. 3)

$$u = h\theta \tag{3. 3}$$

The governing equation can then be written as

$$\frac{\partial u}{\partial t} + \frac{\partial f}{\partial x} + \frac{\partial g}{\partial z} = 0 \tag{3. 66}$$

where the fluxes *f* and *g* are given by,

$$\begin{aligned} f &= a u - b \frac{\partial u}{\partial x}, \\ g &= c u - d \frac{\partial u}{\partial z} \end{aligned} \tag{3. 67}$$

The expressions for the coefficients *a*, *b*, *c* and *d* used in Eq. (3. 67) are

$$\begin{aligned} a &= \frac{V}{2} + g_c \frac{\beta h}{12\mu} \frac{\partial h}{\partial x}, \\ b &= d = g_c \frac{\beta h^2}{12\mu}, \\ c &= g_c \frac{\beta h}{12\mu} \frac{\partial h}{\partial z}. \end{aligned} \tag{3. 68}$$

In the case of journal bearings with radius R, radial clearance C, and angular velocity ω, the governing equation can be non-dimensionalized using the following transformations

$$\bar{x}, \bar{z} = \frac{\bar{x}, \bar{z}}{2\pi R}, \tag{3. 69}$$

$$\bar{t} = t\omega, \tag{3. 70}$$

$$\bar{h} = \frac{h}{C}, \tag{3. 71}$$

$$\bar{\beta}' = \frac{\beta'}{\mu\omega}\left(\frac{C}{R}\right)^2. \tag{3. 72}$$

The coefficients from Eq. (3. 67) are in this case

$$\begin{aligned} a &= \frac{1}{4\pi} + g_c \frac{\bar{\beta}'\bar{h}}{48\pi^2}\frac{\partial \bar{h}}{\partial \bar{x}} \\ b = d &= g_c \frac{\bar{\beta}'\bar{h}^2}{48\pi^2} \\ c &= g_c \frac{\bar{\beta}'\bar{h}}{48\pi^2}\frac{\partial \bar{h}}{\partial \bar{z}} \end{aligned} \tag{3. 73}$$

Since there are no conceptual differences between the dimensional and non-dimensional forms, in the following the more simple form, without bar, will be used.

All coefficients a, b, c and d are functions of space variables x and z. If the geometry is time dependent, then the film is expressed as $h = h(x, z, t)$, and these coefficients are also time dependent. However, when developing the numerical algorithm, these coefficients are considered to be locally constant, i.e., within the volume of each elementary conservation element.

A first order Taylor series for the unknown function *u*, starting from an expansion point $O(x_0, z_0, t_0)$ is

$$u \cong u_0 + (u_x)_0 (x - x_0) + (u_z)_0 (z - z_0) + (u_t)_0 (t - t_0), \tag{3. 74}$$

where the time derivative, in conformity with Eq. (3. 66), can be written as

$$(u_t)_0 = -\left(\frac{\partial f}{\partial x}\right)_0 - \left(\frac{\partial g}{\partial z}\right)_0 . \tag{3. 75}$$

Since the flux terms *f* and *g* can be considered as functions of the unknown *u* and its space derivatives $f = f(u, u_x, u_z)$, $g = g(u, u_x, u_z)$ using a first order approximation, we may write that

$$\begin{aligned} \frac{\partial f}{\partial x} &\cong \frac{\partial f}{\partial u} u_x = a u_x , \\ \frac{\partial g}{\partial z} &\cong \frac{\partial g}{\partial u} u_z = c u_z . \end{aligned} \tag{3. 76}$$

Accordingly, Eq. (3. 74) becomes

$$u \cong u_0 + (u_x)_0 (x - x_0) + (u_z)_0 (z - z_0) - \left[a_0 (u_x)_0 + c_0 (u_z)_0\right](t - t_0). \tag{3. 77}$$

In the same way functions *f* and *g* are approximated as

$$\begin{aligned} f &\cong \left(\frac{\partial f}{\partial u}\right)_0 u + \left(\frac{\partial f}{\partial u_x}\right)_0 u_x + \left(\frac{\partial f}{\partial u_z}\right)_0 u_z = a_0 u - b_0 u_x , \\ g &\cong \left(\frac{\partial g}{\partial u}\right)_0 u + \left(\frac{\partial g}{\partial u_x}\right)_0 u_x + \left(\frac{\partial g}{\partial u_z}\right)_0 u_z = c_0 u - d_0 u_z . \end{aligned} \tag{3. 78}$$

Alternately, considering that in the vicinity of the expansion point $O(x_0, z_0, t_0)$, $u_x \cong const. = (u_x)_0$, $u_z \cong const. = (u_z)_0$ and substituting the expression of *u* from Eq. (3. 77) into Eq. (3. 78) yields

$$
\begin{aligned}
f &\cong a_0 u_0 - b_0 (u_x)_0 + a_0 (u_x)_0 (x - x_0) + a_0 (u_z)_0 (z - z_0) - \left[a_0^2 (u_x)_0 + a_0 c_0 (u_z)_0 \right] (t - t_0), \\
g &\cong c_0 u_0 - d_0 (u_z)_0 + c_0 (u_x)_0 (x - x_0) + c_0 (u_z)_0 (z - z_0) - \left[a_0 c_0 (u_x)_0 + c_0^2 (u_z)_0 \right] (t - t_0).
\end{aligned}
\tag{3. 79}
$$

Consider a triangular mesh in the (x, z) plane. One triangle *BCD* and its three neighbor elements are shown in Fig. 3. 17. Point *A* is the centroid of the triangle *BCD*, while points *E*, *F* and *G* are the centroids of the neighbor triangles *BCH*, *CDI* and *BDJ*.

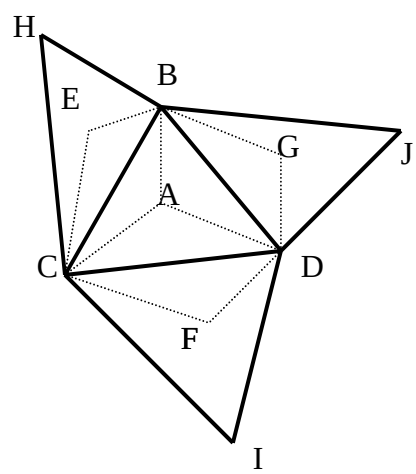

Fig. 3. 17 – Triangular mesh element and its neighbors

Similar to the 1-D case, in the 2-D formulation the CE/SE method calculates the values of the dependent variables u, u_x, u_z for a representative point of the triangular element centered at *A* for the time step $t = t^{n+\frac{1}{2}}$ using the corresponding values of the same variables for the elements centered in *E*, *F* and *G* at the time step $t = t^n$. In order to calculate the three unknowns at the new time step, a system of three equations will be derived. One equation can be obtained considering the quadrilateral *ABEC*. Integrating

simultaneously the governing equation, Eq. (3. 66), over the surface of this quadrilateral and in time, between time steps t^n and $t^{n+\frac{1}{2}}$ (see Fig. 3. 18), yields

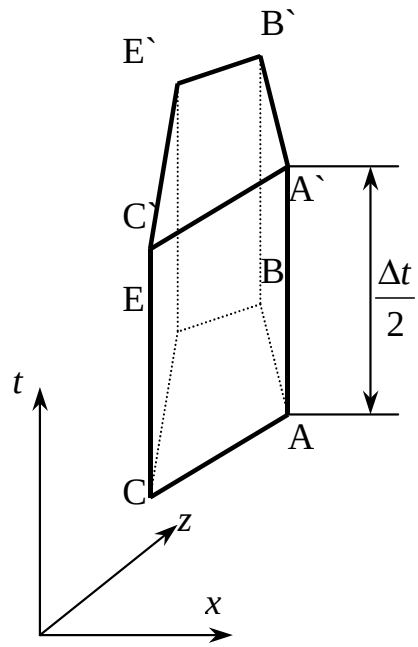

Fig. 3. 18 – Conservation volume in the (x,z,t) space

$$\iint_{ABEC} \int_{t^n}^{t^{n+\frac{1}{2}}} \frac{\partial u}{\partial t} \mathrm{d}t\,\mathrm{d}\sigma + \int_{t^n}^{t^{n+\frac{1}{2}}} \iint_{ABEC} \left[\frac{\partial}{\partial x}(a u - b u_x) + \frac{\partial}{\partial z}(c u - d u_z) \right] \mathrm{d}\sigma\,\mathrm{d}t = 0 . \qquad (3.\ 80)$$

Equation (3. 80) implies flux conservation in the three-dimensional space (x,z,t). Performing the time integration for the first term and transforming the surface integration into a contour integration for the second term (using the divergence theorem) yields,

$$\iint_{ABEC} \left(u^{n+\frac{1}{2}} - u^n \right) \mathrm{d}\sigma + \int_{t^n}^{t^{n+\frac{1}{2}}} \oint_{ABEC} \vec{\mathbf{F}} \cdot \vec{\mathbf{n}}\,\mathrm{d}s\,\mathrm{d}t = 0 , \qquad (3.\ 81)$$

where $\vec{\mathbf{n}}$ is the outward directed unit vector normal to the contour, and

$$\vec{\mathbf{F}} = f\,\vec{\mathbf{i}} + g\,\vec{\mathbf{k}} \tag{3. 82}$$

is a vector in the (x, z) plane characterized by the Cartesian unit vectors $(\vec{\mathbf{i}}, \vec{\mathbf{k}})$. Functions *f* and *g* are given by Eq. (3. 67).

Functions *u*, *f*, *g* are next substituted using the linear approximations, see Eqs. (3. 77) and (3. 79), so that Eq. (3. 81) can be written as

$$\left(u_{ABEC}^{n+\frac{1}{2}} - u_{ABEC}^{n}\right) A_{ABEC} + \frac{\Delta t}{2}\left(\oint_{ABEC} \vec{\mathbf{F}} \cdot \vec{\mathbf{n}}\, \mathrm{d}s\right)^{n+\frac{1}{4}} = 0\,, \tag{3. 83}$$

where $u_{ABEC}^{n+\frac{1}{2}}$ and u_{ABEC}^{n} designate the value of *u* in the center of the quadrilateral *ABEC* at the time steps $n + \frac{1}{2}$ and *n*, A_{ABEC} is the area of the quadrilateral *ABEC* and the contour integration is calculated at the time $t^{n+\frac{1}{4}} = t^{n} + \frac{\Delta t}{4}$. The values $u_{ABEC}^{n+\frac{1}{2}}$ and u_{ABEC}^{n} are evaluated from Eq. (3. 77) using as the Taylor expansion point $A'(x_{A'}, z_{A'})$ at the time step $t^{n+\frac{1}{2}}$ and $E'(x_{E'}, z_{E'})$ at the time step t^{n}, respectively. The expansion points *A'* and *E'*, which will be considered as representative points for elements *BCD* and *BHC*, can be chosen in any suitable way. The exact position of these points will be selected later. Equation (3. 77) becomes,

$$\begin{aligned} u_{ABEC}^{n+\frac{1}{2}} &= u_{A'}^{n+\frac{1}{2}} + (x_{ABEC} - x_{A'}) \left.\frac{\partial u}{\partial x}\right|_{A'}^{n+\frac{1}{2}} + (z_{ABEC} - z_{A'}) \left.\frac{\partial u}{\partial z}\right|_{A'}^{n+\frac{1}{2}}, \\ u_{ABEC}^{n} &= u_{E'}^{n} + (x_{ABEC} - x_{E'}) \left.\frac{\partial u}{\partial x}\right|_{E'}^{n} + (z_{ABEC} - z_{E'}) \left.\frac{\partial u}{\partial z}\right|_{E'}^{n}. \end{aligned} \tag{3. 84}$$

The contour integral from the second term in Eq. (3. 83) can be divided into four line integrals along the sides of the quadrilateral.

$$\oint_{ABEC} \vec{\mathbf{F}}^{n+\frac{1}{4}} \cdot \vec{\mathbf{n}}\,\mathrm{d}s = \int_{AB} \vec{\mathbf{F}}^{n+\frac{1}{4}} \cdot \vec{\mathbf{n}}_{AB}\,\mathrm{d}s + \int_{BE} \vec{\mathbf{F}}^{n+\frac{1}{4}} \cdot \vec{\mathbf{n}}_{BE}\,\mathrm{d}s + \int_{EC} \vec{\mathbf{F}}^{n+\frac{1}{4}} \cdot \vec{\mathbf{n}}_{EC}\,\mathrm{d}s + \int_{CA} \vec{\mathbf{F}}^{n+\frac{1}{4}} \cdot \vec{\mathbf{n}}_{CA}\,\mathrm{d}s. \tag{3. 85}$$

Each of these four line integrals, consistent with the previous approximations, is calculated considering that each integrand has a linear form. From the mean value theorem of calculus, the value of each line integral is equal to the value of the integrand at the midpoint of the line segment multiplied by the length of the segment. For the segment *AB*, considering $\left(A', t^{n+\frac{1}{2}}\right)$ as the Taylor series expansion point in Eq. (3. 79), we have,

$$\begin{aligned}
&\int_{AB} \vec{\mathbf{F}}^{n+\frac{1}{4}} \cdot \vec{\mathbf{n}}_{AB}\mathrm{d}s = \left[f\, n_{x\,AB} + g\, n_{z\,AB}\right]_{\frac{A+B}{2}}^{n+\frac{1}{4}} L_{AB} = \\
&= \left[\left(a u - b u_x\right)\Big|_{A'}^{n+\frac{1}{2}} + \left(a u_x\right)\Big|_{A'}^{n+\frac{1}{2}} \left(\frac{x_A + x_B}{2} - x_{A'}\right) + \left(a u_z\right)\Big|_{A'}^{n+\frac{1}{2}} \left(\frac{z_A + z_B}{2} - z_{A'}\right) \right. \\
&\left. + \left(a^2 u_x + a c u_z\right)_{A'}^{n+\frac{1}{2}} \frac{\Delta t}{4} \right] \left(z_B - z_A\right) - \left[\left(c u - d u_z\right)\Big|_{A'}^{n+\frac{1}{2}} + \left(c u_x\right)\Big|_{A'}^{n+\frac{1}{2}} \left(\frac{x_A + x_B}{2} - x_{A'}\right) \right. \\
&\left. + \left(c u_z\right)\Big|_{A'}^{n+\frac{1}{2}} \left(\frac{z_A + z_B}{2} - z_{A'}\right) + \left(a c u_x + c^2 u_z\right)_{A'}^{n+\frac{1}{2}} \frac{\Delta t}{4} \right] \left(x_B - x_A\right)
\end{aligned} \tag{3. 86}$$

In Eq. (3. 86) the exterior unit normal to the segment *AB* of length L_{AB} has been substituted with its expression,

$$\vec{\mathbf{n}}_{AB} = n_{x\,AB}\,\vec{\mathbf{i}} + n_{z\,AB}\,\vec{\mathbf{j}} = \frac{\left(z_B - z_A\right)\vec{\mathbf{i}} - \left(x_B - x_A\right)\vec{\mathbf{j}}}{L_{AB}} \tag{3. 87}$$

where n_x and n_z are the *x* and *z* components of the unit vector $\vec{\mathbf{n}}$.

Similar expressions can be written for the other three line integrals of Eq. (3. 85). Note that the Taylor expansions must be performed starting from point $\left(A', t^{n+\frac{1}{2}}\right)$ for the line integrals $\int_{AB} \vec{\mathbf{F}}^{n+\frac{1}{4}} \cdot \vec{\mathbf{n}}_{AB}\, \mathrm{d}s$ and $\int_{CA} \vec{\mathbf{F}}^{n+\frac{1}{4}} \cdot \vec{\mathbf{n}}_{CA}\, \mathrm{d}s$, while for the integrals $\int_{BE} \vec{\mathbf{F}}^{n+\frac{1}{4}} \cdot \vec{\mathbf{n}}_{BE}\, \mathrm{d}s$ and $\int_{EC} \vec{\mathbf{F}}^{n+\frac{1}{4}} \cdot \vec{\mathbf{n}}_{EC}\, \mathrm{d}s$ point $\left(E', t^{n}\right)$ must be used. Because the calculations can be relatively complicated for a generic grid, the symbolic mathematical code MAPLE was used. Performing all the calculations and substituting into Eq. (3. 83) yields the first equation for the considered triangular element

$$a_1 u_{A'}^{n+\frac{1}{2}} + b_1 \left(u_x\right)_{A'}^{n+\frac{1}{2}} + c_1 \left(u_z\right)_{A'}^{n+\frac{1}{2}} + d_1 u_{E'}^{n} + e_1 \left(u_x\right)_{E'}^{n} + f_1 \left(u_z\right)_{E'}^{n} = 0\,, \qquad \text{(3. 88 a)}$$

where $a_1, b_1, c_1, d_1, e_1, f_1$ are coefficients that depend on the geometry (coordinates of points A, A', E, E', B, C and the center of quadrilateral *ABEC*) and on the governing equation coefficients *a*, *b*, *c*, *d* given by Eq. (3. 68), evaluated at points A' and E' at the time steps $n+\frac{1}{2}$ and *n*, respectively.

Considering the quadrilaterals *ACFD* and *ADGB*, two additional equations similar to Eq. (3. 88-a) are developed

$$a_2 u_{A'}^{n+\frac{1}{2}} + b_2 \left(u_x\right)_{A'}^{n+\frac{1}{2}} + c_2 \left(u_z\right)_{A'}^{n+\frac{1}{2}} + d_2 u_{F'}^{n} + e_2 \left(u_x\right)_{F'}^{n} + f_2 \left(u_z\right)_{F'}^{n} = 0, \qquad \text{(3. 88 b)}$$

$$a_3 u_{A'}^{n+\frac{1}{2}} + b_3 \left(u_x\right)_{A'}^{n+\frac{1}{2}} + c_3 \left(u_z\right)_{A'}^{n+\frac{1}{2}} + d_3 u_{G'}^{n} + e_3 \left(u_x\right)_{G'}^{n} + f_3 \left(u_z\right)_{G'}^{n} = 0\ . \qquad \text{(3. 88 c)}$$

In Eqs. (3. 88 b) and (3. 88 c), F’ and G’ are the representative points for the triangular elements *CID* and *DJB*, respectively (see Fig. 3. 17).

All values at the time step *n* (previous half time step) are known, so that Eqs. (3. 88 a), (3. 88 b) and (3. 88 c) form a system of three equations with three unknowns, $u_{A'}^{n+\frac{1}{2}}, (u_x)_{A'}^{n+\frac{1}{2}}, (u_z)_{A'}^{n+\frac{1}{2}}$. Written in this form the method is locally implicit. Note that the coefficients of the system, being functions of the coefficients *a*, *b*, *c*, *d* given by Eq. (3. 68), depend also on the unknown $u_{A'}^{n+\frac{1}{2}}$ through the switch coefficient g_c. An iterative method to solve this system is thus necessary.

An alternate approach is to choose the Taylor series expansion point A' as the center of the hexagon *BECFDG* of Fig. 3. 17. The other three Taylor series expansion points E', F', G' can be chosen arbitrarily; however, in order to maintain consistency, they are chosen as the centers of the corresponding hexagons formed around the neighboring triangular elements. Note that the values of the dependent variables at time step *n*, i.e., u, u_x, u_z, must be known at these points. Note also that, as with the previous approximations, the values of the derivatives u_x, u_z at any given time step are considered constant on the surface of a triangular element (such as *BCD*), while the value of the variable *u* at the same time step can be calculated using the first order Taylor expansion, Eq. (3. 77).

Adding Eqs. (3. 88 a, b, c) yields a new equation that represents the flux conservation over the hexagon and over one half time step. When point A' is the center of the hexagon *BECFDG*, this equation has a simpler form given by

$$a_{sum} u_{A'}^{n+\frac{1}{2}} + d_1 u_{E'}^n + e_1 (u_x)_{E'}^n + f_1 (u_z)_{E'}^n + d_2 u_{F'}^n + e_2 (u_x)_{F'}^n + f_2 (u_z)_{F'}^n \\ d_3 u_{G'}^n + e_3 (u_x)_{G'}^n + f_3 (u_z)_{G'}^n = 0, \tag{3. 89}$$

where

$$a_{sum} = A_{ABEC} + A_{ACFD} + A_{ADGB} = A_{BECFDG} \,. \tag{3. 90}$$

This equation has only one unknown, $u_{A'}^{n+\frac{1}{2}}$, and can easily be solved explicitly. It is also important to note that all the coefficients in Eq. (3. 89) depend only on the geometry (coordinates of the points) and the values of the dependent variables at the previous half time step so that no iterative method is needed.

After calculating the value $u_{A'}^{n+\frac{1}{2}}$, the values of the other two dependent variables $(u_x)_{A'}^{n+\frac{1}{2}}$ and $(u_z)_{A'}^{n+\frac{1}{2}}$ can be calculated using any two of the equations in the set, Eqs. (3. 88 a, b, c). Because $u_{A'}^{n+\frac{1}{2}}$ is known at this stage of calculations, the value of g_c is also known, so that all coefficients in Eqs. (3. 88 a, b, c) are determined.

In order to insure stability (not only neutral stability), the method must have at least some form of artificial dissipation. Therefore, just as in the 1-D case, the $a-\varepsilon$ scheme and the $a-\varepsilon-\alpha-\beta$ scheme are introduced. Both schemes differ from the *a* scheme only in the way the derivatives $(u_x)_{A'}^{n+\frac{1}{2}}$ and $(u_z)_{A'}^{n+\frac{1}{2}}$ are calculated. Because the value $u_{A'}^{n+\frac{1}{2}}$ is computed from Eq. (3. 89), the flux conservation over the boundary of the hexagon *BECFDG* and in time is still insured. However, because the derivatives $(u_x)_{A'}^{n+\frac{1}{2}}$ and $(u_z)_{A'}^{n+\frac{1}{2}}$ are not calculated from the system, Eqs. (3. 88 a, b, c), the flux conservation is not insured in this case over each of the quadrilaterals *ABEC*, *ACFD* and *ADGB.*

The $a-\varepsilon$ scheme starts from the principle that central differencing computation of the derivatives provides numerical dissipation. In this scheme the values of the

dependent variable *u* at the new time step $n+\frac{1}{2}$ are evaluated at three new points E'', F'', G''. Let A'' be the center of the triangle $E'F'G'$ (refer to Fig. 3. 19) and let $\overrightarrow{A''A'}$ be the vector that displaces points E', F', G' into the three new points E'', F'', G'' respectively, i.e.

$$\overrightarrow{A''A'} = \overrightarrow{E'E''} = \overrightarrow{F'F''} = \overrightarrow{G'G''} \tag{3. 91}$$

This procedure insures that the center of the triangle $E''F''G''$ coincides with point A'.

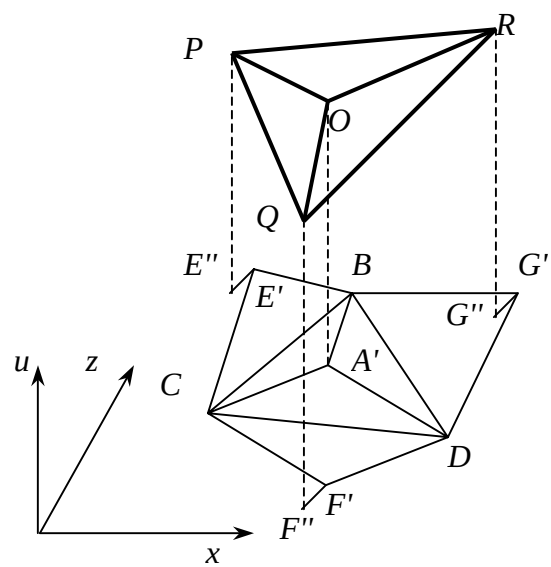

Fig. 3. 19 – The (x, z, u) space considered for $a-\varepsilon$ and $a-\varepsilon-\alpha-\beta$ schemes

The values $u_{E''}^{n+\frac{1}{2}}, u_{F''}^{n+\frac{1}{2}}$ and $u_{G''}^{n+\frac{1}{2}}$ can easily be computed using the Taylor expansion, Eq. (3. 77) with the expansion points E', F', G' respectively, and at the time step *n*. For instance,

$$u_{E''}^{n+\frac{1}{2}} = u_{E'}^{n} + (x_{E''} - x_{E'})(u_x)_{E'}^{n} + (z_{E''} - z_{E'})(u_z)_{E'}^{n} - \frac{\Delta t}{2}\left[a_{E'}^{n}(u_x)_{E'}^{n} + c_{E'}^{n}(u_z)_{E'}^{n}\right]. \tag{3. 92}$$

Similar expressions are used for the calculation of $u_{F''}^{n+\frac{1}{2}}$ and $u_{G''}^{n+\frac{1}{2}}$. Consider also the value $u_{A'}^{n+\frac{1}{2}}$ calculated from Eq. (3. 89). In the space (x,z,u), four points can be defined: $O\left(x_{A'},z_{A'},u_{A'}^{n+\frac{1}{2}}\right)$, $P\left(x_{E''},z_{E''},u_{E''}^{n+\frac{1}{2}}\right)$, $Q\left(x_{F''},z_{F''},u_{F''}^{n+\frac{1}{2}}\right)$ and $R\left(x_{G''},z_{G''},u_{G''}^{n+\frac{1}{2}}\right)$, as shown in Fig. (3. 19). Consider four planes, each defined by a set of three points: *OPQ*, *OQR*, *ORP* and *PQR*. In each of these planes function *u* is linear both in *x* and *z*, so that the values of its partial space derivatives can easily be calculated.

In order to illustrate this simple procedure, consider the plane *OPQ*. In this plane, function *u* has the expression

$$u(x,z)_{OPQ}=\left(\frac{\partial u}{\partial x}\right)_{OPQ}x+\left(\frac{\partial u}{\partial z}\right)_{OPQ}z+u_0 \tag{3. 93}$$

where u_0 is a constant, while $\left(\frac{\partial u}{\partial x}\right)_{OPQ}$ and $\left(\frac{\partial u}{\partial z}\right)_{OPQ}$ are the spatial partial derivatives corresponding to the triangle *OPQ*, derivatives that are to be determined. Imposing the conditions

$$\begin{aligned} &u(x_{A'},z_{A'})=u_{A'}^{n+\frac{1}{2}} \quad \text{(point } O\text{)},\\ &u(x_{E''},z_{E''})=u_{E''}^{n+\frac{1}{2}} \quad \text{(point } P\text{)},\\ &u(x_{F''},z_{F''})=u_{F''}^{n+\frac{1}{2}} \quad \text{(point } Q\text{)}, \end{aligned} \tag{3. 94}$$

and solving the linear system of three equations with three unknowns with Cramer's rule, the values of the spatial partial derivatives are

$$\left(\frac{\partial u}{\partial x}\right)_{OPQ} = \frac{\Delta_1}{\Delta},$$
$$\left(\frac{\partial u}{\partial z}\right)_{OPQ} = \frac{\Delta_2}{\Delta}, \tag{3. 95}$$

where Δ, Δ_1 and Δ_2 are the following determinants:

$$\Delta = \begin{vmatrix} x_{A'} & z_{A'} & 1 \\ x_{E''} & z_{E''} & 1 \\ x_{F''} & z_{F''} & 1 \end{vmatrix}, \ \Delta_1 = \begin{vmatrix} u_{A'}^{n+\frac{1}{2}} & z_{A'} & 1 \\ u_{E''}^{n+\frac{1}{2}} & z_{E''} & 1 \\ u_{F''}^{n+\frac{1}{2}} & z_{F''} & 1 \end{vmatrix}, \ \Delta_2 = \begin{vmatrix} x_{A'} & u_{A'}^{n+\frac{1}{2}} & 1 \\ x_{E''} & u_{E''}^{n+\frac{1}{2}} & 1 \\ x_{F''} & u_{F''}^{n+\frac{1}{2}} & 1 \end{vmatrix}. \tag{3. 96}$$

Similar expressions can easily be deduced for the partial derivatives expressed in the other three planes *OQR*, *ORP* and *PQR*. Finally, define the "central" derivatives at point A' as the average values of the derivatives obtained for the three triangles *OPQ*, *OQR* and *ORP*, i.e.,

$$\left(u_x^c\right)_{A'}^{n+\frac{1}{2}} = \frac{1}{3}\left[\left(\frac{\partial u}{\partial x}\right)_{OPQ} + \left(\frac{\partial u}{\partial x}\right)_{OQR} + \left(\frac{\partial u}{\partial x}\right)_{ORP}\right],$$
$$\left(u_z^c\right)_{A'}^{n+\frac{1}{2}} = \frac{1}{3}\left[\left(\frac{\partial u}{\partial z}\right)_{OPQ} + \left(\frac{\partial u}{\partial z}\right)_{OQR} + \left(\frac{\partial u}{\partial z}\right)_{ORP}\right]. \tag{3. 97}$$

Because, as previously shown, point A' is the center of the triangle $E''F''G''$, the values obtained with Eq. (3. 97) are the same as the values obtained for the plane *PQR*. Thus, $\left(u_x^c\right)_{A'}^{n+\frac{1}{2}}$ and $\left(u_z^c\right)_{A'}^{n+\frac{1}{2}}$ can be interpreted as central-difference estimates of the space derivatives at point A'. Note also that the computation of these derivatives is entirely explicit.

The $a-\varepsilon$ scheme considers a weighted average between the values of the derivatives calculated with the *a* scheme and the values obtained with Eqs. (3. 97), i.e.,

$$\left(u_x^{a-\varepsilon}\right)_{A'}^{n+\frac{1}{2}} = \left(u_x^{a}\right)_{A'}^{n+\frac{1}{2}} + 2\varepsilon\left[\left(u_x^{c}\right)_{A'}^{n+\frac{1}{2}} - \left(u_x^{a}\right)_{A'}^{n+\frac{1}{2}}\right],$$
$$\left(u_z^{a-\varepsilon}\right)_{A'}^{n+\frac{1}{2}} = \left(u_z^{a}\right)_{A'}^{n+\frac{1}{2}} + 2\varepsilon\left[\left(u_z^{c}\right)_{A'}^{n+\frac{1}{2}} - \left(u_z^{a}\right)_{A'}^{n+\frac{1}{2}}\right]. \tag{3. 98}$$

Note that for $\varepsilon = 0.5$,

$$\left(u_x^{a-\varepsilon}\right)_{A'}^{n+\frac{1}{2}} = \left(u_x^{c}\right)_{A'}^{n+\frac{1}{2}}\ ,\ \left(u_z^{a-\varepsilon}\right)_{A'}^{n+\frac{1}{2}} = \left(u_z^{c}\right)_{A'}^{n+\frac{1}{2}}.$$

Therefore the $a-\varepsilon$ scheme is completely explicit (the values calculated with the *a* scheme are not needed).

The $a-\varepsilon-\alpha-\beta$ scheme considers first the absolute values of the gradients of function *u* calculated in the three planes *OPQ*, *OQR* and *ORP*, i.e.,

$$\theta_{OPQ} = \sqrt{\left(u_x\right)_{OPQ}^2 + \left(u_z\right)_{OPQ}^2} \tag{3. 99}$$

where $\left(u_x\right)_{OPQ}$ and $\left(u_z\right)_{OPQ}$ are calculated with Eqs. (3. 95). Similarly,

$$\theta_{OQR} = \sqrt{\left(u_x\right)_{OQR}^2 + \left(u_z\right)_{OQR}^2},$$
$$\theta_{ORP} = \sqrt{\left(u_x\right)_{ORP}^2 + \left(u_z\right)_{ORP}^2}. \tag{3. 100}$$

Two new nonlinear weighted average values for the space derivatives can be computed

$$\left(u_x^{w}\right)_{A'}^{n+\frac{1}{2}} = \frac{\left(\theta_{OQR}\theta_{ORP}\right)^{\alpha}\left(u_x\right)_{OPQ} + \left(\theta_{ORP}\theta_{OPQ}\right)^{\alpha}\left(u_x\right)_{OQR} + \left(\theta_{OPQ}\theta_{OQR}\right)^{\alpha}\left(u_x\right)_{ORP}}{\left(\theta_{OQR}\theta_{ORP}\right)^{\alpha} + \left(\theta_{ORP}\theta_{OPQ}\right)^{\alpha} + \left(\theta_{OPQ}\theta_{OQR}\right)^{\alpha}},$$
$$\left(u_z^{w}\right)_{A'}^{n+\frac{1}{2}} = \frac{\left(\theta_{OQR}\theta_{ORP}\right)^{\alpha}\left(u_z\right)_{OPQ} + \left(\theta_{ORP}\theta_{OPQ}\right)^{\alpha}\left(u_z\right)_{OQR} + \left(\theta_{OPQ}\theta_{OQR}\right)^{\alpha}\left(u_z\right)_{ORP}}{\left(\theta_{OQR}\theta_{ORP}\right)^{\alpha} + \left(\theta_{ORP}\theta_{OPQ}\right)^{\alpha} + \left(\theta_{OPQ}\theta_{OQR}\right)^{\alpha}} \tag{3. 101}$$

where α is a parameter, usually with the value 1 or 2. Finally, the derivatives computed with the $a-\varepsilon-\alpha-\beta$ scheme are weighted averages between the values $\left(u_x^{a}\right)_{A'}^{n+\frac{1}{2}}$, $\left(u_z^{a}\right)_{A'}^{n+\frac{1}{2}}$

calculated from the system, Eqs. (3. 88 a-c), $\left(u_x^c\right)_{A'}^{n+\frac{1}{2}}$, $\left(u_z^c\right)_{A'}^{n+\frac{1}{2}}$ obtained with Eqs. (3. 97) and $\left(u_x^w\right)_{A'}^{n+\frac{1}{2}}$, $\left(u_z^w\right)_{A'}^{n+\frac{1}{2}}$ calculated with Eqs. (3. 101), i.e.

$$\begin{aligned}
\left(u_x^{a-\varepsilon-\alpha-\beta}\right)_{A'}^{n+\frac{1}{2}} &= \left(u_x^a\right)_{A'}^{n+\frac{1}{2}} + 2\varepsilon\left[\left(u_x^c\right)_{A'}^{n+\frac{1}{2}} - \left(u_x^a\right)_{A'}^{n+\frac{1}{2}}\right] + \beta\left[\left(u_x^w\right)_{A'}^{n+\frac{1}{2}} - \left(u_x^c\right)_{A'}^{n+\frac{1}{2}}\right], \\
\left(u_z^{a-\varepsilon-\alpha-\beta}\right)_{A'}^{n+\frac{1}{2}} &= \left(u_z^a\right)_{A'}^{n+\frac{1}{2}} + 2\varepsilon\left[\left(u_z^c\right)_{A'}^{n+\frac{1}{2}} - \left(u_z^a\right)_{A'}^{n+\frac{1}{2}}\right] + \beta\left[\left(u_z^w\right)_{A'}^{n+\frac{1}{2}} - \left(u_z^c\right)_{A'}^{n+\frac{1}{2}}\right].
\end{aligned} \tag{3. 102}$$

As in the 1-D cases, the numerical dissipation introduced by the ε term is effective in damping out numerical instabilities that occur in the smooth regions of the solution, while the $\alpha-\beta$ term is effective in damping out the wiggles that can occur in the vicinity of the solution discontinuities. Stability requires, besides the CFL condition, that the $a-\varepsilon-\alpha-\beta$ scheme must also satisfy the following conditions

$$\begin{aligned}
&0 \le \varepsilon \le 1, \\
&\beta \ge 0, \\
&\alpha \ge 0.
\end{aligned} \tag{3. 103}$$

The $a-\varepsilon$ scheme can be considered as a particular case of the $a-\varepsilon-\alpha-\beta$ method for $\beta = 0$ or $\alpha = 0$, while the *a* scheme can be obtained when the supplementary condition $\varepsilon = 0$ is satisfied. The most computationally efficient scheme, as previously shown, is obtained for $\varepsilon = 0.5$ because in this case the method is purely (globally and locally) explicit; therefore only this case has been used to obtain the results shown in the next section.

Considering that at one half time step the values u, u_x, u_z have been calculated for point A', the values of the same dependent variables can be determined at the same half time step at any other point inside the hexagon *BECFDG* using the simplified Taylor

expansion, Eq. (3. 77), (without the time dependent term) and considering that u_x and u_z are constant over the surface of the hexagon.

Figure 3.20 shows a simple, uniform, grid. Over one half time step, the values of the dependent variables u, u_x, u_z are calculated for one set of triangular elements (centers), like those marked with solid points in the figure. Over the next half time step the other set of triangular elements are used - marked with hollow circles. Over the next time step the first set of elements are considered again, and so forth. In conclusion two half time steps are necessary to return to original set of elements.

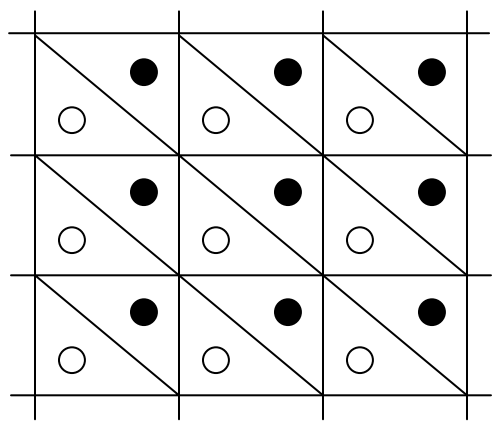

Fig. 3. 20 – Uniform triangular mesh

An alternative method of estimating u_x and u_z at the new time step has been proposed recently by Liu and Chen [2001]. This method requires, at each half time step, the calculation of new values for variable *u* for all triangular elements. In a manner similar to the development of the $a-\varepsilon-\alpha-\beta$ method, consider in the three-dimensional space (x,z,u) four points defined as $O\left(x_{A'}, z_{A'}, u_{A'}^{n+\frac{1}{2}}\right)$, $P_1\left(x_{E'}, z_{E'}, u_{E'}^{n+\frac{1}{2}}\right)$, $Q_1\left(x_{F'}, z_{F'}, u_{F'}^{n+\frac{1}{2}}\right)$ and

$R_1\left(x_{G'}, z_{G'}, u_{G'}^{n+\frac{1}{2}}\right)$. Three planes can be considered, each defined by a set of three points: OP_1Q_1, OQ_1R_1 and OR_1Q_1. Considering that function u is linear in both x and z directions over the domains defined by these planes, the partial derivatives can easily be calculated over the three domains (triangles OP_1Q_1, OQ_1R_1 and OR_1Q_1) using equations similar to Eqs. (3. 96) and (3. 97). Let $(u_x)_{OP_1Q_1}, (u_z)_{OP_1Q_1}$, $(u_x)_{OQ_1R_1}, (u_z)_{OQ_1R_1}$ and $(u_x)_{OR_1P_1}, (u_z)_{OR_1P_1}$ be these values, respectively. The partial derivatives at the new time step can now be estimated using equations similar to Eqs. (3. 99)-(3. 101). No ε-type artificial dissipation is introduced.

No significant differences between the results obtained using any of the above artificial dissipation schemes have been observed.

In conclusion, the unknowns at the new half time step $n+\frac{1}{2}$ are calculated as functions of the old half-time step n using explicit expressions, Eqs. (3. 89), and (3. 102). At this stage, the grid is shifted. For example, when at time step n the variables are known at solid nodes (see Fig. 3. 20), at the half-time step $n+\frac{1}{2}$ the unknowns are calculated at the hollow nodes (Fig. 3. 20). It takes another half-time step, $n+\frac{1}{2} \rightarrow n+1$, for the grid to return to the solid nodes. This peculiarity explains the half-time division. Also, the fact that the derivatives are not calculated directly from the conservation laws (which was the price paid for making the scheme fully explicit) does not diminish the value of the method: the conservation laws are still satisfied within the larger, hexagonal elements. The method is simultaneously accurate (the conservation is satisfied both in

space and time for the hexagonal elements) and explicit (computationally efficient). It is these characteristics that provide the strength of the CE/SE method.

3. 3. 2. Applications for circular bearings

In order to determine the performance of the method, several numerical examples are considered. The results are compared with the results obtained from other numerical methods, as well as with experimental data. Only the steady state solution, obtained by time integration until the state parameters stabilize, is presented.

A standard journal bearing with one inlet groove is first considered. The geometry and the fluid characteristics are presented in Table 3. 3.

The boundary conditions are directly related to the configuration considered. At the axial ends of the bearing, the pressure is set, equal to the atmospheric pressure, which also equals the cavitation pressure. The main unknown function, u, is related to the variable θ, which is the density in the full film region, and the fractional film content in the cavitated region, respectively. The boundary conditions at the axial ends must detect whether or not the considered elements on the boundary are within the cavitated region or the full film region. In the full film region, for $p = p_{at} = p_c$

$$\theta = 1, \tag{3. 104}$$

which means that

$$u = h\theta = h. \tag{3. 105}$$

In the cavitated region the only condition is

$$\theta < 1, \tag{3. 106}$$

so that the value of u is not known a priori, and it must be calculated from the field.

Table 3. 3.

Physical conditions for circular journal bearing

Parameter	Value	Units
Length	$26.0 \cdot 10^{-3}$	m
Diameter	$45.0 \cdot 10^{-3}$	m
Clearance	$15.0 \cdot 10^{-6}$	m
Relative eccentricity	0.8	-
Lub. supply position	120	deg
Supply pressure (gage)	$5.458 \cdot 10^{5}$	Pa
Velocity	3952	rot/min
Viscosity	0.00325	Pa s
Bulk Modulus (β')	$1.21 \cdot 10^{8}$	Pa
Cavitation Pressure (gage)	0	N/m^2

The boundary conditions must be imposed such that the conservation conditions are still satisfied for the elements on the boundaries. The conservation condition is not enough to determine the values of the unknowns (variable *u* and its spatial derivatives), since on the boundary the number of the unknowns is larger than the number of conservation conditions. For example, in Fig. 3. 17, suppose the element centered on A is on the boundary, and the element centered on F is a ghost element, situated outside the computational domain. In this case, the conservation conditions lead to the calculation of the unknowns at point A (or more precisely at point A'), using the procedure described

above. There are not enough conditions however to calculate the unknowns at point F. Only one condition can be imposed, i.e., the conservation on the volume formed by surface ACFD and over a half time step, while the number of unknowns is three (u, u_x and u_z). Even when the value of u is known, as in the cases for which Eq. (3. 105) can be imposed, there still are not enough conditions to uniquely determine the spatial derivatives. Therefore, the boundary conditions can be imposed in a number of ways [Chang, Zhang, Yu, and Jorgenson, 2000]. One very simple methodology has been used, which is described in following.

First, the computational domain is extended with a row of cells, see Fig. 3. 21. These cells are selected so that they have identical dimensions to the neighboring cells, and positioned anti-symmetrically relative to the boundary. For example, in Fig. 3. 21, the quadrilateral ACFD is actually a parallelogram because the elements centered on point A and on point F (the ghost element), respectively, have the same size and are positioned anti-symmetrically relative to the center of the segment CD. The centroid F' of the ghost element cannot be defined because no hexagonal conservation element can be formed around it. However, point F' is selected such that it is positioned anti-symmetrically with point A' relative to the center of the segment CD. The conservation condition over the volume ACFD and in time is satisfied considering that

$$u_F^{\,n+\frac{1}{2}} = u_A^{\,n},\ (u_x)_F^{\,n+\frac{1}{2}} = (u_x)_A^{\,n},\ (u_z)_F^{\,n+\frac{1}{2}} = (u_z)_A^{\,n}. \qquad (3.\ 107)$$

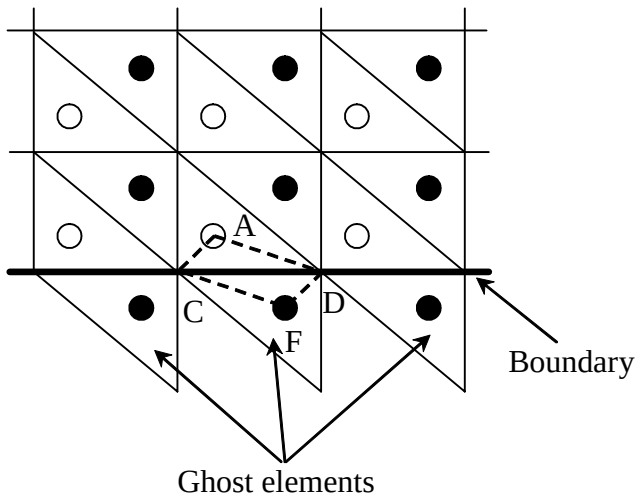

Fig. 3. 21 – Ghost elements for the boundary conditions

Indeed, the flux that crosses the boundary AC between two consecutive time steps is equal with the flux that crosses the boundary FD between two consecutive time steps, but with changed sign because the normal vectors $\vec{n}$ on the two surfaces have opposite directions. Similarly, the fluxes crossing surfaces DA and CF between time steps *n* and $n+\frac{1}{2}$ are also equal and have opposite signs. Also the fluxes crossing surfaces ACFD at between time steps *n* and $n+\frac{1}{2}$ are equal and have opposite signs. Therefore, the entire flux entering the conservation volume ACFD between time steps *n* and $n+\frac{1}{2}$ also leaves the same volume, without being reflected back into the computational domain. This shows that the boundary conditions (3. 107) are correctly imposed. The conditions given by Eq. (3. 107) are very simple to implement in the computer code, which is another advantage of the CE/SE method compared with other numerical methods. Note that, for the best geometric accuracy, the centroids of the elements which are similar with element

A should be on the actual boundary. In other words, the actual boundary should pass through the most southern row of hollow points, not the way it is shown in Fig. 3. 21.

Symmetry boundary conditions can be imposed at the center-plane of symmetric bearings, and thus only half of the full computational domain is analysed. In this case the ghost elements are chosen symmetric relative to the boundary, and the conditions are

$$u_F^{n+\frac{1}{2}} = u_A^{\ n},\ (u_x)_F^{\ n+\frac{1}{2}} = (u_x)_A^{\ n},\ (u_z)_F^{\ n+\frac{1}{2}} = (u_z)_A^{\ n} = 0\,. \qquad (3.\ 108)$$

Figures 3. 22 and 3. 23 show a comparison between the pressure distributions and the fluid film content θ obtained with CE/SE method and with the type difference method of Vijayaraghavan and Keith [1989]. Two transverse sections through the bearing at $z = 0$ and $z = \frac{L}{4}$ are presented for each method. Note that the bearing z coordinate ranges between the values $-L/2 \le z \le L/2$ so that $z = 0$ is the symmetry plane. The differences between the two methods are relatively small; the maximum pressure predicted using type differencing is 6.7% smaller than the maximum pressure calculated with the present method, while the total load is only 1.3% smaller. The difference between the attitude angles calculated with the two methods is 0.4^0. Two cavitated regions, $\theta < 1$, are visible. The larger one is located immediately before the lubricant supply position, and it will be given more detail shortly. The smaller cavitated region is located around 162^0 from the origin of the circumferential coordinate. Figure 3. 23 shows that for this second cavitated region, both methods predict $\theta \approx 1$ at the symmetry plane, $z = 0$, and $\theta < 1$ at $z = \frac{L}{4}$, which indicates that the cavitation is more pronounced toward the ends of the bearing that at the center.

In Fig. 3. 23, for the larger cavitated region, the type differencing method seems to be able to better handle the large discontinuity for the fractional film content than the CE/SE method. However, the discontinuity was not actually calculated in the type differencing results. Rather, two boundaries (the two sides of the lubricant supply pocket) are shown next to the other, so that the sharp discontinuity in the fractional film content distribution is only due to the representation. On the other hand, the computational domain used by CE/SE code is continuous (periodic boundary conditions are used at one circumferential position), so that the fractional film content discontinuity appears naturally in the field. This approach was possible only because this method is able to cope with large discontinuities without introducing significant numerical smearing and/or oscillations. The code developed using this method is thus more general and can be applied to bearings where the computational domain cannot be split at the lubricant location (when the supply pocket is inside the bearing, without reaching the bearing margins).

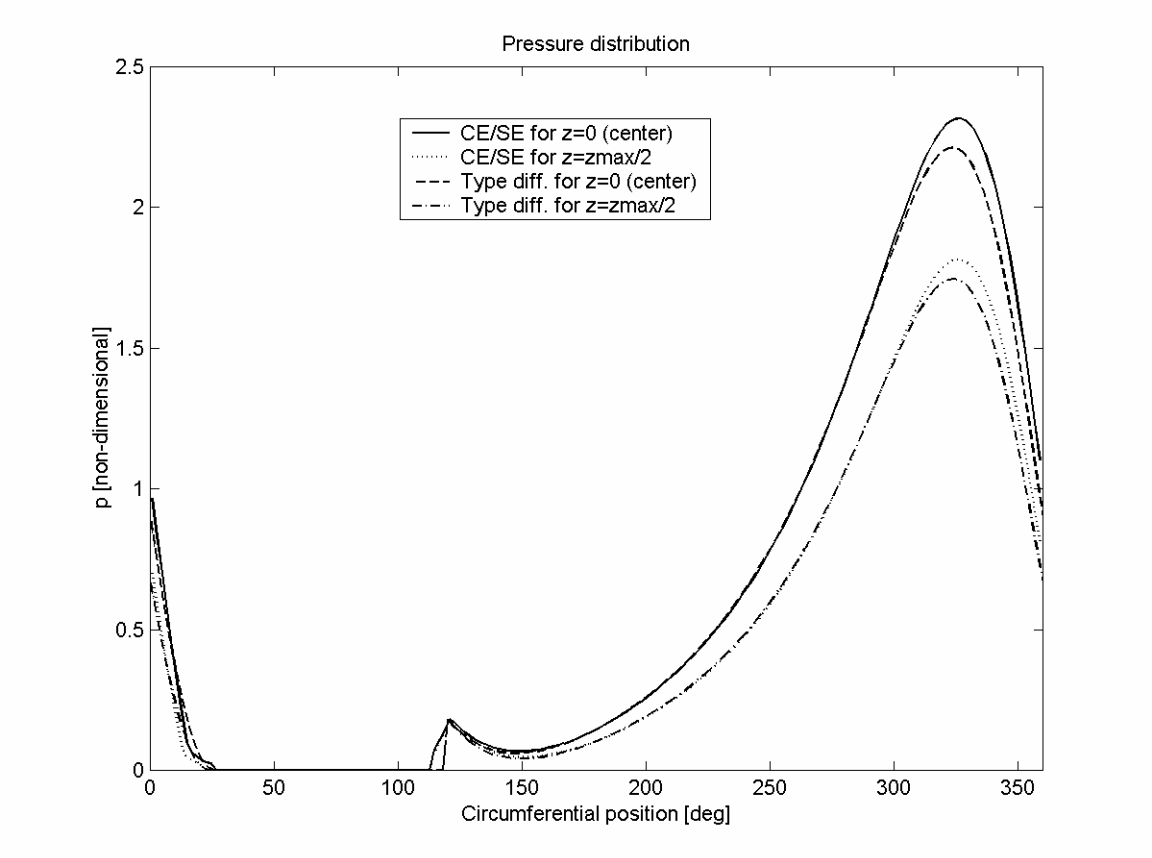

Fig. 3. 22 – Pressure distribution for a circular journal bearing with one inlet groove

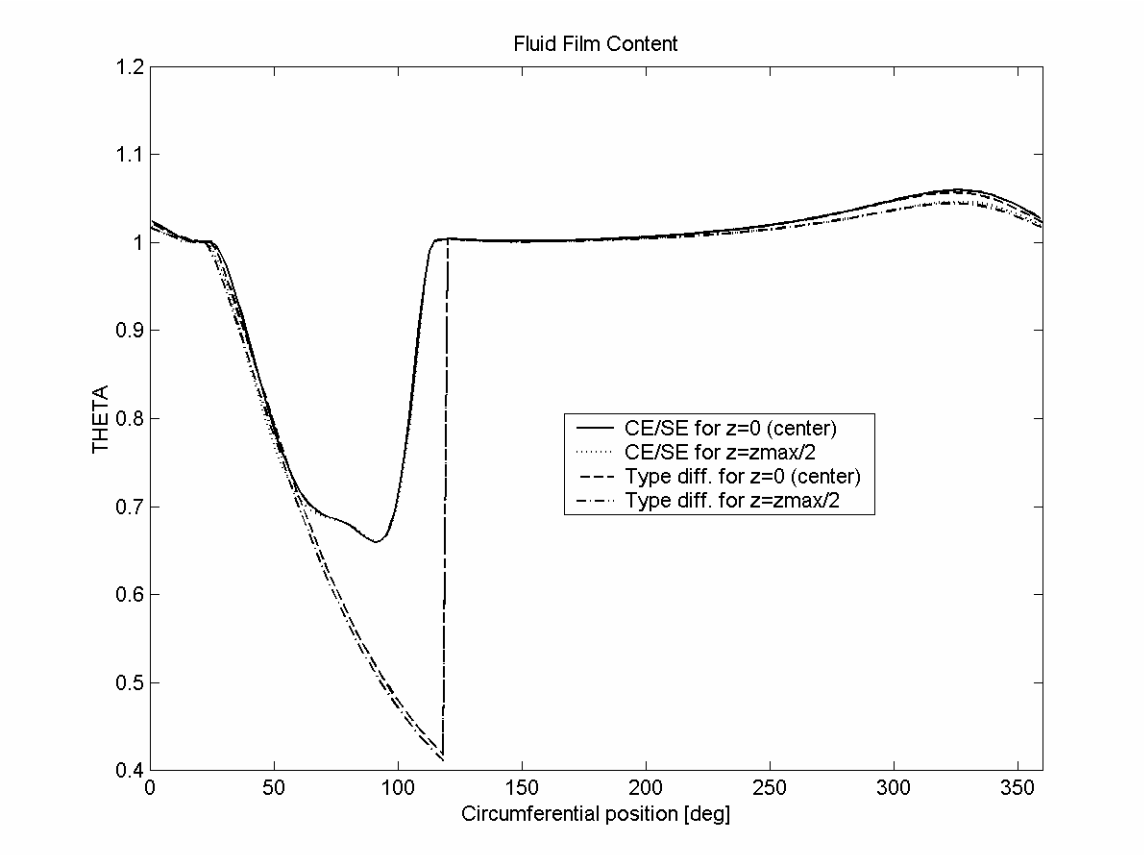

Fig. 3. 23 – Fractional film content distribution for a circular journal bearing with one inlet

3. 3. 3. Applications for wave bearings

The geometry of a wave bearing is more complex compared to the geometry of a standard journal bearing, [Dimofte, 1995]. The geometry is obtained by super-imposing a wave distribution on the fixed surface of a journal bearing. For example, considering that the shaft is rotating and the bearing sleeve is fixed, the sleeve is manufactured or deformed using exterior forces such that the interior surface is not circular, but it has a wavy shape. Figure 3. 24a shows a circular sleeve, and Fig. 3. 24b shows a wave bearing sleeve with three waves. The amplitude of the waves is greatly exaggerated in order to be visible. The circular sleeve shown has two rows of supply orifices. This configuration is

used in gas bearings, which will be discussed in the following chapter. Considering that there are n_w waves over the circumference of the bearing sleeve, the amplitude of the wave is $\varepsilon_w C$, where ε_w is the non-dimensional wave amplitude and C is the radial clearance of the bearing, and the wave starts at an angle θ_w relative to the circumferential coordinate θ, the wave shape can be written as

$$h_w = \varepsilon_w C \cos\left[n_w\left(\bar{x} - \bar{x}_w\right)\right] \tag{3. 109}$$

This distribution is added to the normal film thickness distribution of a journal bearing to get the final distribution

$$\frac{h}{C} = 1 + \varepsilon \cos\left(\bar{x} - \bar{x}_0\right) + \varepsilon_w C \cos\left[n_w\left(\bar{x} - \bar{x}_w\right)\right] \tag{3. 110}$$

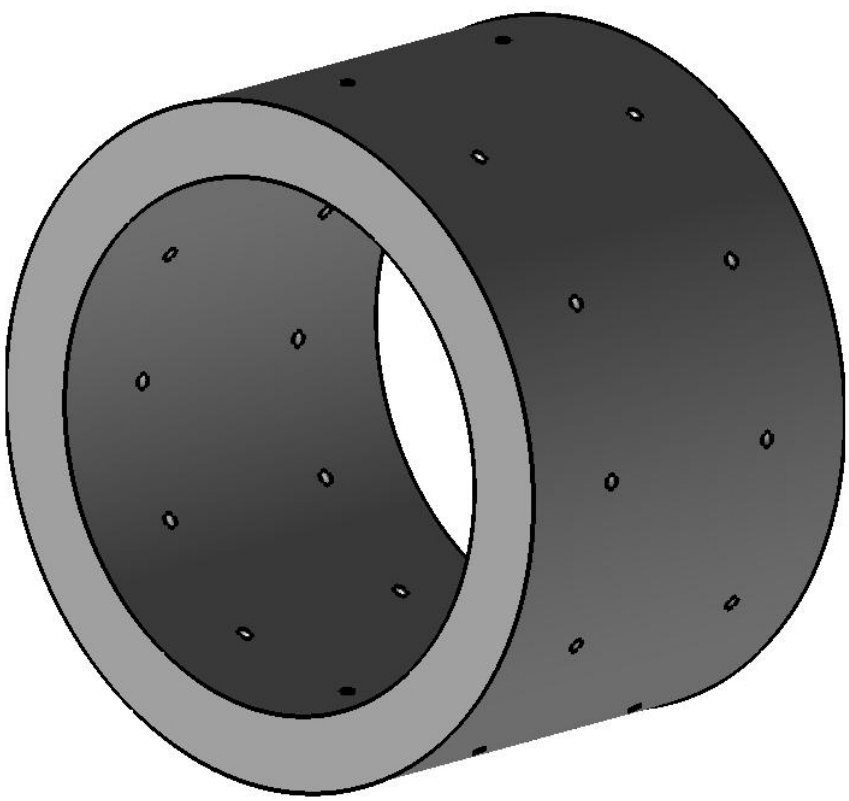

Fig. 3. 24a – Circular bearing sleeve

Fig. 3. 24b – Wave bearing sleeve

An example of the non-dimensional film thickness, $\frac{h}{C}$, distribution for a three-wave bearing as a function of the circumferential coordinate is shown in Fig. 3. 25. The physical conditions of the wave bearing considered in calculations are presented in Table 3. 4.

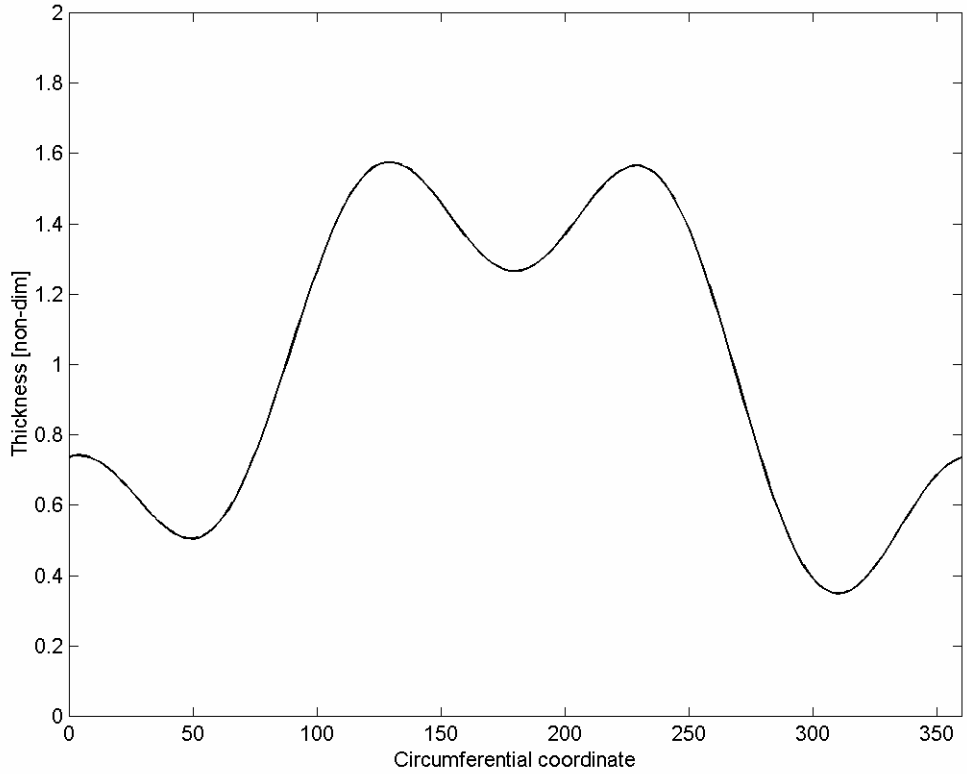

Fig. 3. 25 – Fluid film thickness distribution in a 3-wave bearing

Figure 3. 26 shows the pressure distribution obtained using the present method compared with the pressure calculated by Dimofte [1995], using a finite difference method to solve the steady form of the Reynolds equation with Gümbel (or half-Sommerfeld) boundary conditions. The results show similar variations, however the peak pressures differ. The total load predicted by the present method is 2039 N, 13.7% higher than the load predicted by Dimofte. The difference between the predicted load directions using the two codes is less than 1.6^0. These results have been obtained using a value $\beta' = 1.2105 \cdot 10^8$ Pa . The pressure distribution for a smaller value of the bulk modulus, $\beta' = 1.029 \cdot 10^7$ Pa , is presented in Fig. 3. 27. In this case, even though both peak

pressures predicted by the present method and Dimofte are almost the same, the total load compared with the previous case does not change significantly. The load directions however have a larger difference (5.5^0). In brief, the film compressibility effects reduce the pressure peaks in the bearing and also produce a change in the phase of the pressure distribution.

Table 3. 4.

Physical conditions for a wave bearing

Parameter	Value	Units
Length	$26.0 \cdot 10^{-3}$	m
Diameter	$45.0 \cdot 10^{-3}$	m
Clearance	$15.0 \cdot 10^{-6}$	m
Number of supply pockets	3	-
Lub. supply positions	86, 206, 326	deg
Supply pockets width	4.0	mm
Supply pressure (gage)	$5.458 \cdot 10^{5}$	Pa
Velocity	3952	rot/min
Viscosity	0.00325	Pa s
Density	902.0	Kg/m^3
Bulk Modulus β' $(\overline{\beta'})$	$1.2105 \cdot 10^{8}$ (40.0)	Pa
	$1.029 \cdot 10^{7}$ (3.4)	
Cavitation Pressure (gage)	0	N/m^2

Note that, although the bulk modulus value for the oil used by Dimofte is not known, the first case ($\beta' = 1.2105 \cdot 10^8$ Pa) probably is a more realistic value. Note as well that the code based on the present method uses a film thickness distribution calculated by Dimofte considering the elastic deformations of the shaft and bushing; this can also be a source of error.

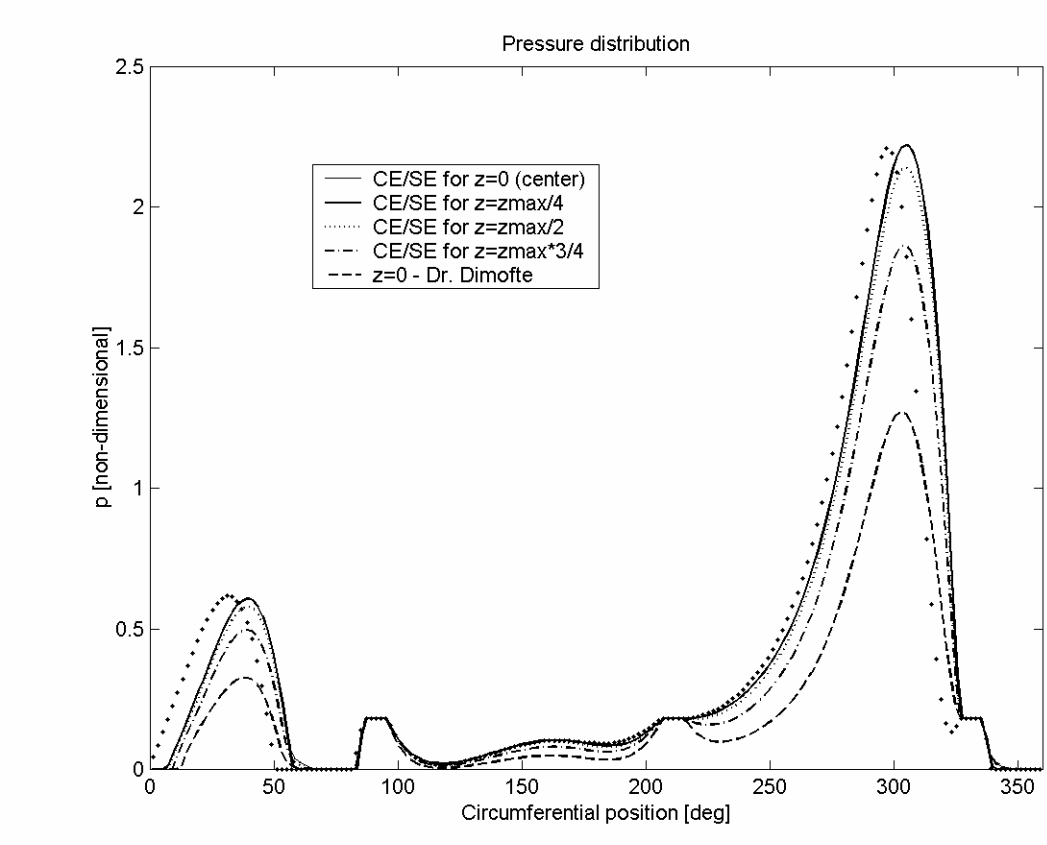

Fig. 3. 26 – Pressure distribution in a wave bearing $\overline{\beta}' = 3.4$

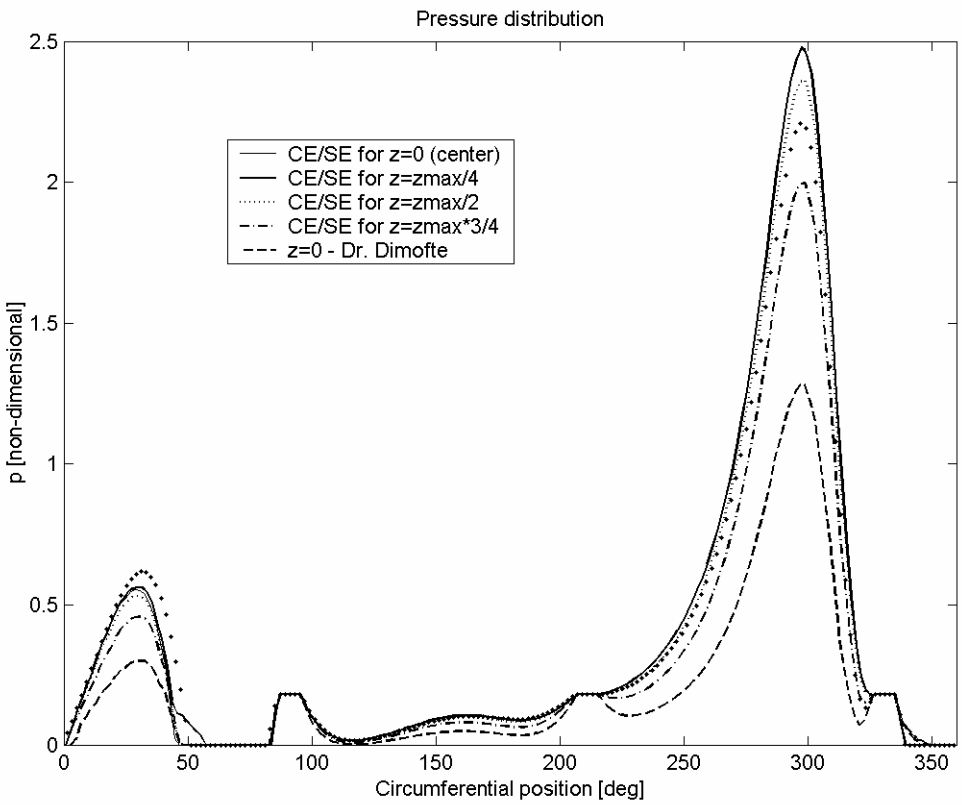

Fig. 3. 27 – Pressure distribution in a wave bearing $\overline{\beta}' = 40.0$

Consider now the case of a misaligned wave bearing. The misalignment of journal bearings can be defined using two parameters: the angle α between the centerline and the direction of the misalignment at the bearing center and the degree of misalignment d_m that represents the proportion of the actual misalignment from the maximum possible. The misalignment is restricted by the condition that at the axial ends of the bearing the film thickness reaches the value of zero. An aligned circular journal bearing is represented in Fig. 3. 28a, and a misaligned bearing in Fig. 3. 28b. In both figures the bearing radial clearance is greatly exaggerated in order to be visible. The physical conditions of the bearing are presented in Table 3. 5. Because of the misalignment, the fluid film thickness is a function of both the circumferential and axial coordinates, so that

for each value of the circumferential coordinate there exists a domain of thickness variation, represented in dark color in Fig. 3. 29.

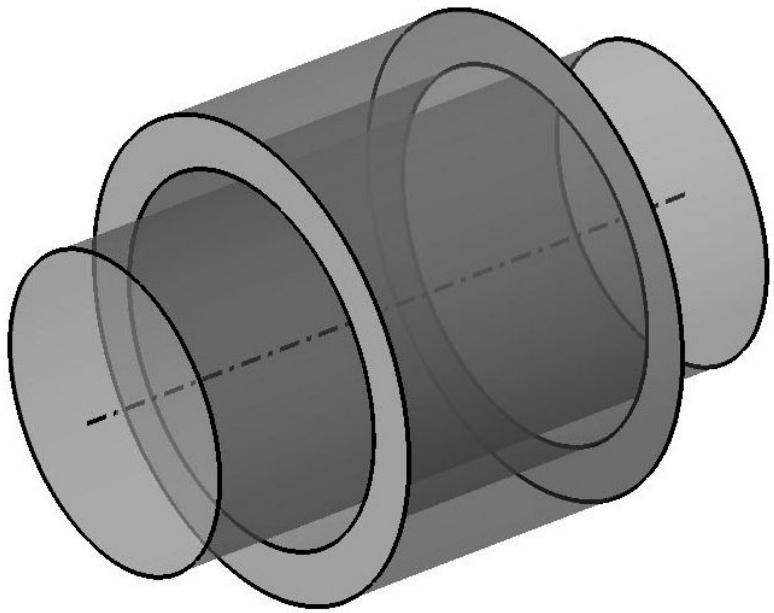

Fig. 3. 28a – Aligned journal bearing

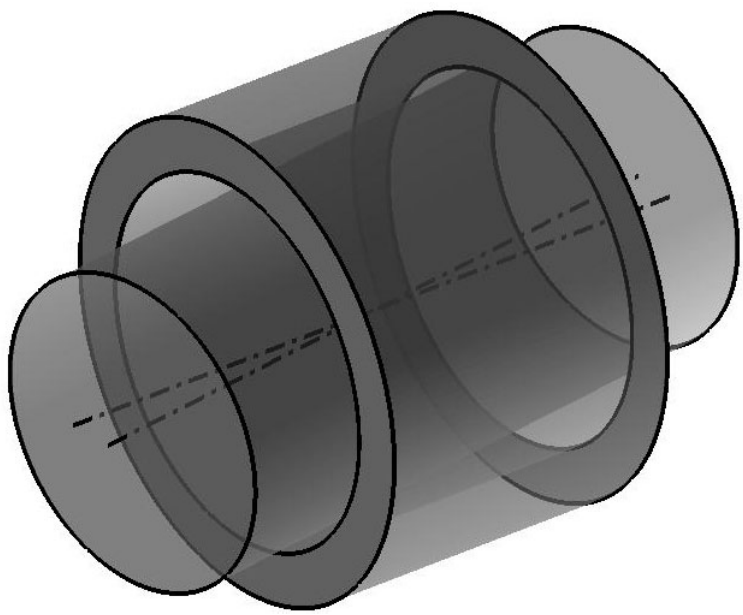

Fig. 3. 28b – Misaligned journal bearing

Table 3. 5

Physical Conditions for a Misaligned Wave Bearing

Parameter	Value	Units
Length	$45.0 \cdot 10^{-3}$	m
Diameter	$45.0 \cdot 10^{-3}$	m
Clearance	$15.0 \cdot 10^{-6}$	m
Angle of misalignment	90	deg
Degree of misalignment	0.5	-
Number of supply pockets	1	-
Lub. supply position	100	deg
Supply pocket width	4.0	mm
Supply pressure (gage)	$5.458 \cdot 10^{5}$	Pa
Velocity	3952	rot/min
Viscosity	0.00325	Pa s
Density	902.0	Kg/m^3
Bulk Modulus β' $(\overline{\beta}')$	$1.2105 \cdot 10^{8}$ (40.0)	Pa
Cavitation Pressure (gage)	0	N/m^2

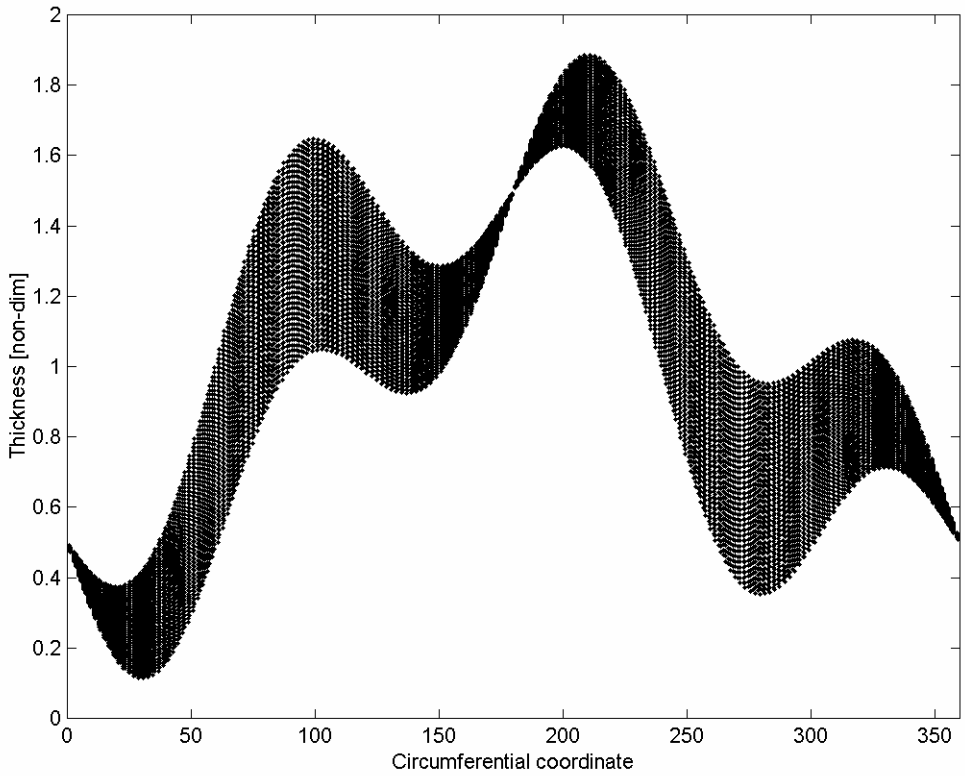

Fig. 3. 29 – Fluid film thickness domain in a misaligned 3-wave bearing

The pressure distribution in the bearing is presented in Figs. 3. 30a and 3. 31a, while the fractional fluid film content is presented in Fig. 3. 32a. The same bearing with the same physical conditions and without misalignment shows different values for the pressure distribution and fractional film content, as seen in Figs. 3. 30b, 3. 31b, and 3. 32b. The cavitation and the full film regions for the misaligned and the aligned 3-wave bearing are presented respectively in Figs. 3. 33a and 3. 33b. The load is 20,988 N for the aligned bearing and 36,100 N for the misaligned bearing, which shows that sometimes misalignment can have a positive impact on bearing performance. This effect is due to

the expanded full film region that permits the development of higher pressures inside the misaligned bearing.

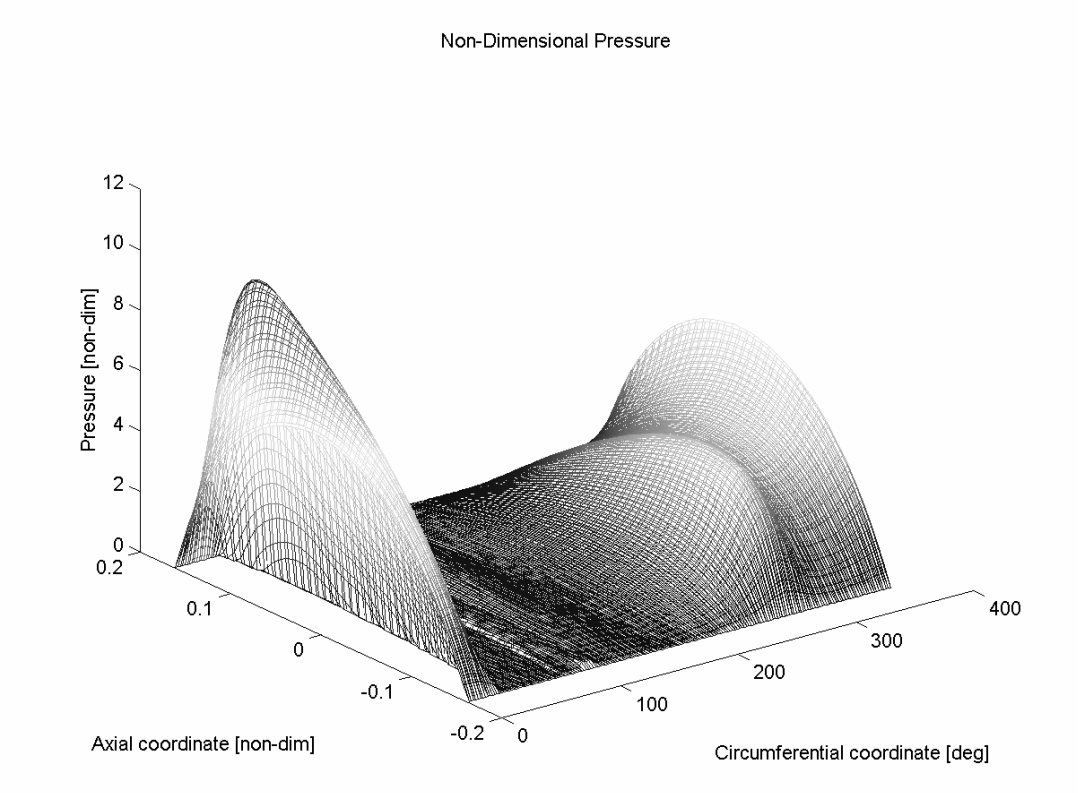

Fig. 3. 30a – Pressure distribution in a misaligned 3-wave bearing

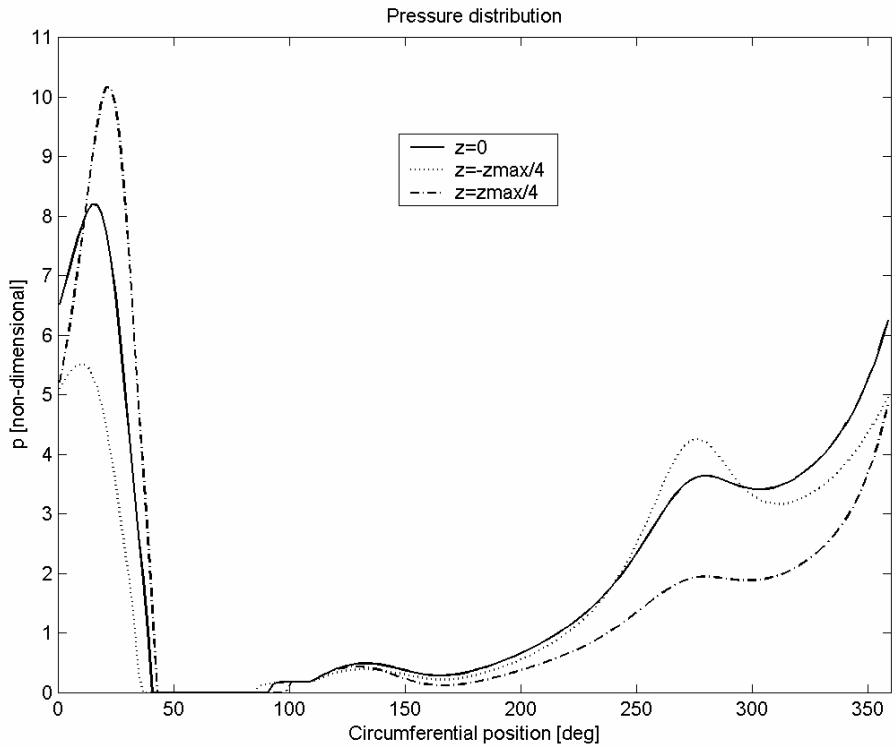

Fig. 3. 31a – Pressure distribution in a misaligned 3-wave bearing at different axial sections

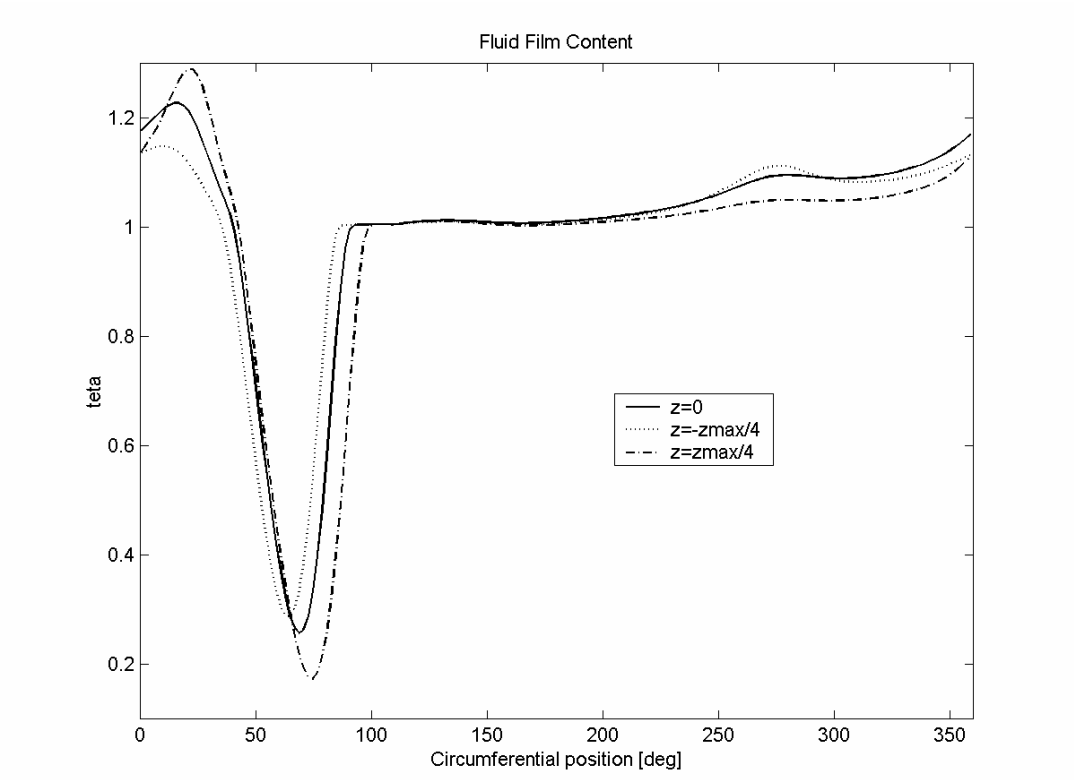

Fig. 3. 32a – Fractional film content distribution in a misaligned 3-wave bearing at different axial sections

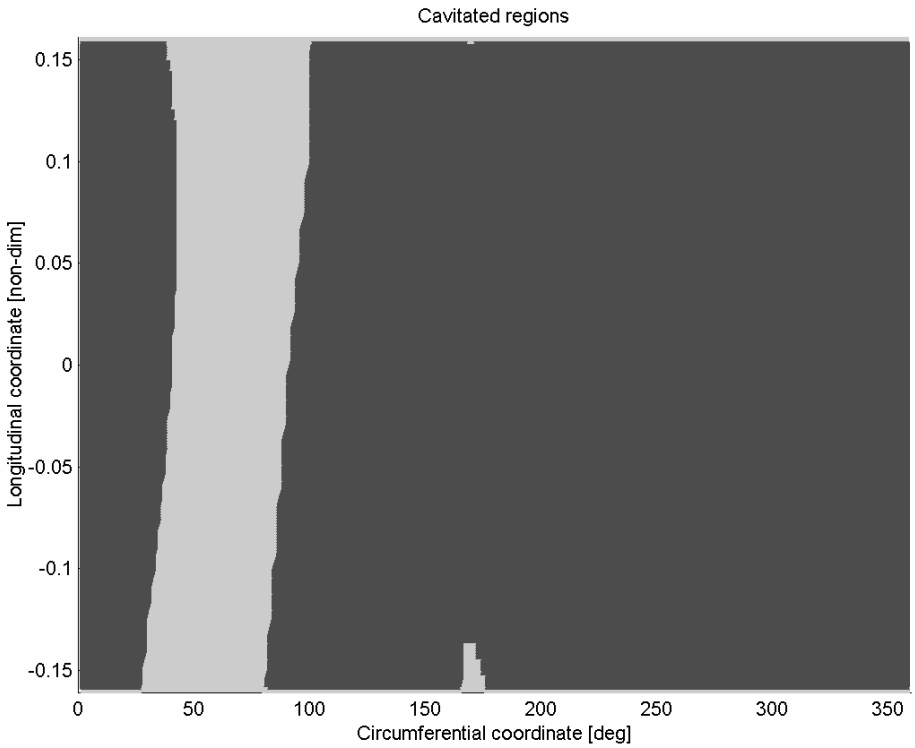

Fig. 3. 33a – Cavitation map in a misaligned 3-wave bearing

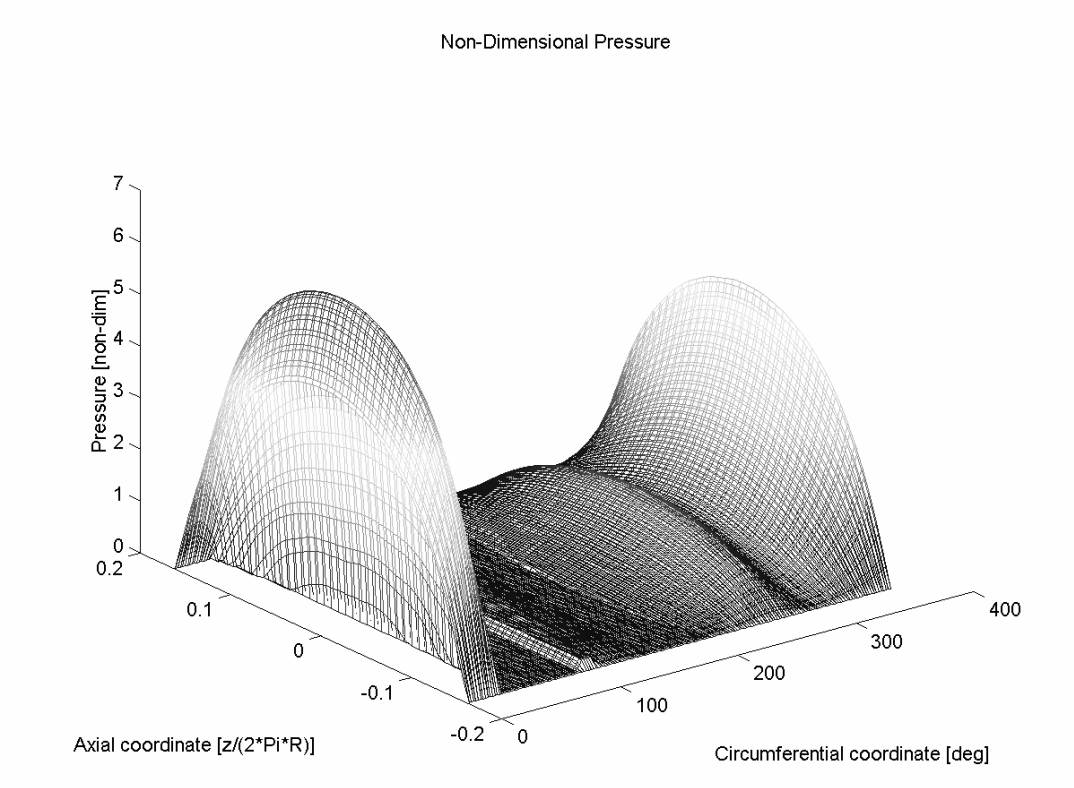

Fig. 3.30b – Pressure distribution in an aligned 3-wave bearing

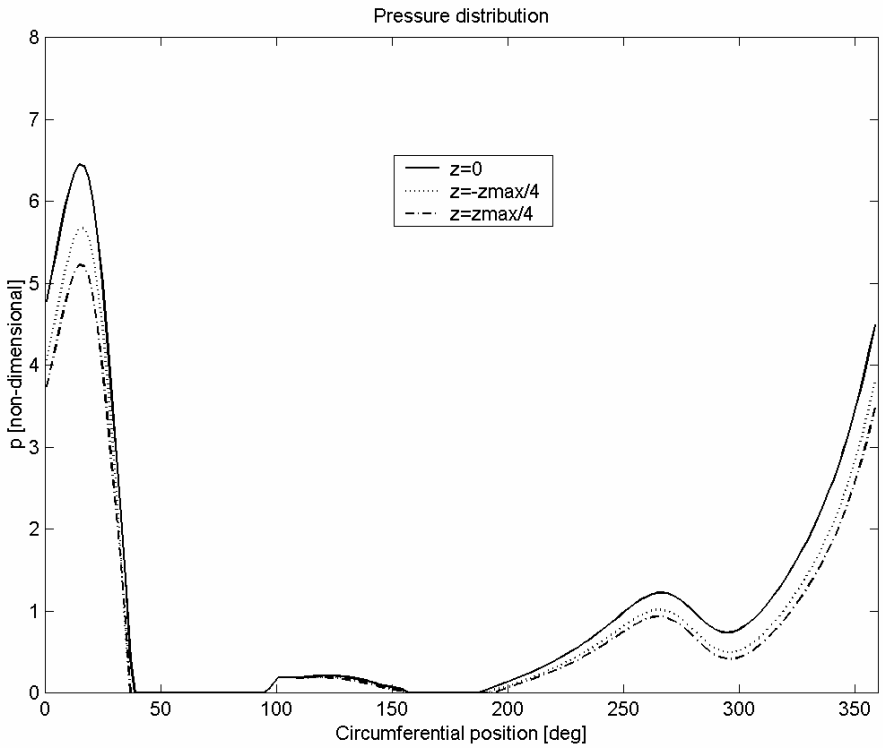

Fig. 3. 31b – Pressure distribution in an aligned 3-wave bearing at different axial sections

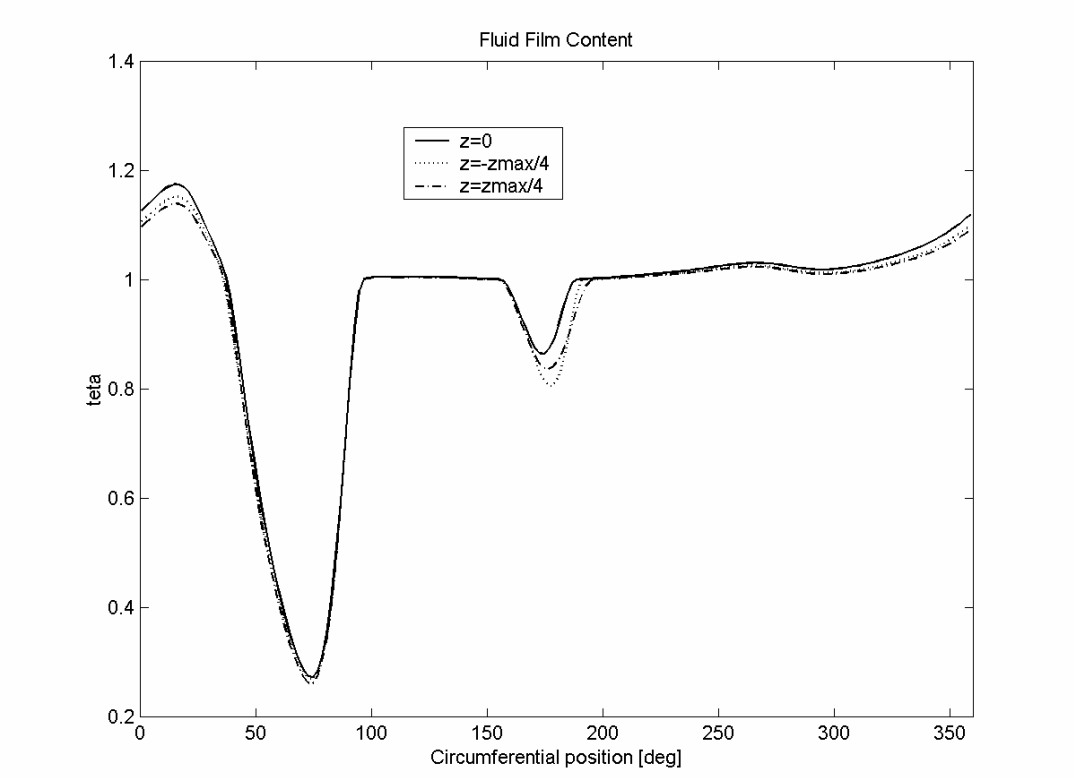

Fig. 3. 32b – Fractional film content distribution in an aligned 3-wave bearing at different axial sections

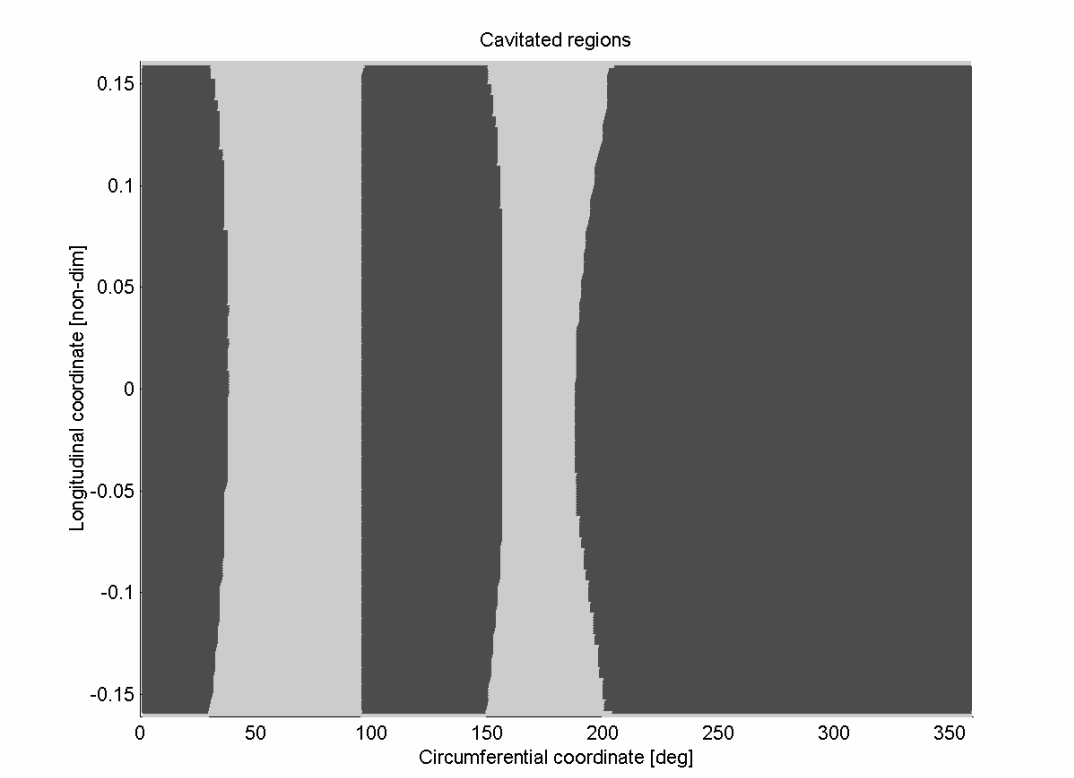

Fig. 3. 33b – Cavitation map in an aligned 3-wave bearing

Chapter Four

Application of the CE/SE Method to Pressurized Gas Bearings

4. 1. Introduction

Gas lubrication was preceded by occasional experimental work in the mid 19th century. This area of tribology experienced strong development in what has come to be known as the "Golden Era" of gas lubrication. This era started in the last years of World War II, and ended in the first part of the 70's [Pan, 1990]. In this period many fundamental studies were published, e.g., [Fuller, 1956], [Lund, 1964, 1967], [Castelli and Pirvics, 1968], [Constantinescu, 1969]. More recently, significant achievements were made in the prediction of dynamic behavior, [Miller and Green, 1998], gas film modeling including rarefaction effects, [Wu and Bogy, 2001], numerical methods applicable to more complex geometries, [Bonneau, Huitric, and Tournerie, 1993], [Faria and San Andrés, 2000], etc.

Compressible viscous flow in pressurized thin fluid films, with application in hybrid gas bearings, can encounter large pressure gradients due to the feeding system or to the large peripheral velocities of the bearing. For these conditions, many of the computational methods based on standard finite difference methods or classic finite volume methods have been found to be inadequate because of convergence problems or

because they induce oscillations into the solution. Thus, a method that is conceptually simple, second order accurate for the entire domain and able to naturally deal with large gradients and/or discontinuities in the solutions without introducing numerical oscillations or smearing, is welcomed.

4. 2. Equations

The two-dimensional, transient, Reynolds equation, written for a Newtonian compressible fluid in laminar flow is,

$$\frac{\partial \rho h}{\partial t} + \frac{\partial}{\partial x}\left(\frac{\rho h V}{2} - \frac{\rho h^3}{12\mu}\frac{\partial p}{\partial x}\right) + \frac{\partial}{\partial z}\left(-\frac{\rho h^3}{12\mu}\frac{\partial p}{\partial z}\right) = 0 \tag{4. 1}$$

The flow is considered polytropic, i.e.,

$$\frac{p}{\rho^k} = const., \tag{4. 2}$$

where the polytropic exponent can take various values. For example $k = 1$ for isothermal flow, $k = \gamma = 1.405$ for adiabatic flow, or can have other values for general polytropic flows.

A more suitable form of the Reynolds equation for numerical formulation is obtained using a new variable *u* that is the product of the non-dimensional film thickness and the non-dimensional density, i.e.,

$$u = \bar{h}\,\bar{\rho} \tag{4. 3}$$

In terms of *u*, in non-dimensional variables, the Reynolds equation can be written as

$$\frac{\partial u}{\partial \bar{t}} + \frac{\partial f}{\partial \bar{x}} + \frac{\partial g}{\partial \bar{z}} = 0, \tag{4. 4}$$

where the flux terms *f* and *g* are,

$$f = \frac{u\overline{V}}{2} - \frac{ku^k}{48\pi^2 \overline{h}^{k-1}}\left(u_x \overline{h} - u\overline{h}_x\right),$$
$$g = -\frac{ku^k}{48\pi^2 \overline{h}^{k-1}}\left(u_z \overline{h} - u\overline{h}_z\right). \tag{4. 5}$$

All partial derivatives considered in Eqs. (4. 4) and (4. 5) are carried out relative to non-dimensional variables $\bar{t}, \bar{x}, \bar{z}$, where $\bar{x}, \bar{z}$ are given by Eq. (3. 69), and

$$\bar{t} = t\frac{p_0}{\mu}\left(\frac{C}{R}\right)^2 \tag{4. 6}$$

Note that the definition of the non-dimensional time is still valid when the bearing has no rotation, i.e., when $\omega = 0$. This methodology, while less intuitive, must be used in this case because the pressurized bearings can also work in the hydrostatic (no relative velocity) regime. In the following, in order to simplify the expressions, the non-dimensional notation (upper bars) will be dropped, and all variables will be implicitly considered in non-dimensional form.

4. 3. Numerical formulation

The formulation is similar to the two-dimensional case described in section 3.3.1. First, consider a triangular mesh that covers the (x, z) spatial domain. One triangle *BCD* and its three neighboring elements are shown in Fig. 3. 18. Again, point *A* is located at the centroid of the triangle *BCD*, while points *E*, *F* and *G* are the centroids of the neighboring triangles *BCH*, *CDI* and *BDJ*, respectively. The CE/SE method calculates the values of the dependent variables u, u_x, u_z for point *A* at the time step $t = t^{n+\frac{1}{2}}$ using the corresponding values of the same variables for the points *E*, *F* and *G* at the time step

$t = t^n$. In order to calculate the three unknowns at the new time step, a system of three equations will be derived.

Consider the quadrilateral *ABEC*. Simultaneously integration of Eq. (4. 4) over the surface of this quadrilateral and in time, between time steps t^n and $t^{n+\frac{1}{2}}$ (see Fig. 3. 19), yields

$$\iint_{ABEC} \int_{t^n}^{t^{n+\frac{1}{2}}} \frac{\partial u}{\partial t} \mathrm{d}t\, \mathrm{d}\sigma + \int_{t^n}^{t^{n+\frac{1}{2}}} \iint_{ABEC} \left[\frac{\partial f}{\partial x} + \frac{\partial g}{\partial z} \right] \mathrm{d}\sigma\, \mathrm{d}t = 0 . \tag{4. 7}$$

Performing the time integration for the first term and transforming the surface integration of the second term (using divergence theorem) into a contour integration produces

$$\iint_{ABEC} \left(u^{n+\frac{1}{2}} - u^n \right) \mathrm{d}\sigma + \int_{t^n}^{t^{n+\frac{1}{2}}} \oint_{ABEC} \vec{\mathbf{F}} \cdot \vec{\mathbf{n}}\, \mathrm{d}s\, \mathrm{d}t = 0 , \tag{4. 8}$$

where $\vec{\mathbf{n}}$ is the unit vector normal to the contour, oriented outwards, and the two-dimensional function, $\vec{\mathbf{F}}$, is calculated using Eq. (3. 82). The flux functions *f* and *g* are in this case given by Eq. (4. 5). Equation (4. 8) implies conservation of flux in the three-dimensional space (x, z, t). Functions *u*, *f*, *g* are next written with linear approximations using first order Taylor expansions, i.e.,

$$u \cong u_0 + (u_x)_0 (x - x_0) + (u_z)_0 (z - z_0) + (u_t)_0 (t - t_0) , \tag{4. 9}$$

$$f \cong f_0 + \left(\frac{\partial f}{\partial u} \right)_0 (u - u_0) + \left(\frac{\partial f}{\partial u_x} \right)_0 \left[u_x - (u_x)_0 \right] + \left(\frac{\partial f}{\partial u_z} \right)_0 \left[u_z - (u_z)_0 \right] = a_F u + b_F u_x + c_F , \tag{4. 10}$$

$$g \cong g_0 + \left(\frac{\partial g}{\partial u} \right)_0 (u - u_0) + \left(\frac{\partial g}{\partial u_x} \right)_0 \left[u_x - (u_x)_0 \right] + \left(\frac{\partial g}{\partial u_z} \right)_0 \left[u_z - (u_z)_0 \right] = a_G u + b_G u_z + c_G . \tag{4. 11}$$

Substituting Eq. (4. 9) into Eqs. (4. 10) and (4. 11) yields linear expressions for *f*

and g as functions of (x,z,t). In Eqs. (4. 10) and (4. 11), the coefficients $a_F, b_F, c_F, a_G, b_G, c_G$ are considered constant when integrating Eq. (4. 8), and are known as functions of $u_0, (u_x)_0, (u_z)_0$. They are calculated using the following expressions,

$$a_F = \frac{V}{2} - \frac{k^2 h_0^{2-k}}{48\pi^2}(u_x)_0 u_0^{k-1} + \frac{k(k-1)(h_x)_0}{24\pi^2 h^{k-1}} u_0^k, \tag{4. 12}$$

$$b_F = b_G = -\frac{k h_0^{2-k}}{48\pi^2} u_0^k, \tag{4. 13}$$

$$c_F = \frac{V}{2} u_0 - \frac{k u_0^k}{48\pi^2 h_0^{n-1}}\left[(u_x)_0 h_0 - u_0 (h_x)_0\right] - a_F u_0 - b_F (u_x)_0, \tag{4. 14}$$

$$a_G = -\frac{k^2 h_0^{2-k}}{48\pi^2}(u_z)_0 u_0^{k-1} + \frac{k(k-1)(h_z)_0}{24\pi^2 h^{k-1}} u_0^k, \tag{4. 15}$$

$$c_G = -\frac{k u_0^k}{48\pi^2 h_0^{k-1}}\left[(u_z)_0 h_0 - u_0 (h_z)_0\right] - a_G u_0 - b_G (u_z)_0. \tag{4. 16}$$

In Eq. (4. 9), the time derivative can be calculated as function of the space derivatives using Eq. (4. 3), i.e.,

$$(u_t)_0 = -(f_x)_0 - (g_z)_0 \cong -a_F (u_x)_0 - a_G (u_z)_0. \tag{4. 17}$$

Equations (4. 9) – (4. 11) are then substituted into Eq. (4. 8). Point $\left(x_{A'}, z_{A'}, t^{n+\frac{1}{2}}\right)$ is used as the Taylor expansion point for the expressions of $u^{n+\frac{1}{2}}$, f and g on contour segments *AB* and *CA*, while point $\left(x_{E'}, z_{E'}, t^n\right)$ is used as the Taylor expansion point for the expressions of u^n, f and g on contour segments *BE* and *EC*. Thus, a first equation with three unknowns, the values u, u_x, u_z at the new half time step $\left(x_{A'}, z_{A'}, t^{n+\frac{1}{2}}\right)$, is

obtained. The coordinates of points A' and E' are selected similarly to the previously discussed case. Therefore, point A' is the centroid of the hexagonal surface *BECFDG*, while point E' is the centroid of the hexagonal element built around the element centered on point *E*. The equation is linear and has the general form,

$$a_1 u_{A'}^{n+\frac{1}{2}} + b_1 (u_x)_{A'}^{n+\frac{1}{2}} + c_1 (u_z)_{A'}^{n+\frac{1}{2}} + d_1 u_{E'}^{n} + e_1 (u_x)_{E'}^{n} + f_1 (u_z)_{E'}^{n} + g_1 = 0 . \quad (4.\ 18a)$$

Two similar equations are obtained using the same procedure for the conservation elements *ACFD* and *ADGB*. These equations have the general form

$$a_2 u_{A'}^{n+\frac{1}{2}} + b_2 (u_x)_{A'}^{n+\frac{1}{2}} + c_2 (u_z)_{A'}^{n+\frac{1}{2}} + d_2 u_{F'}^{n} + e_2 (u_x)_{F'}^{n} + f_2 (u_z)_{F'}^{n} + g_2 = 0 \ ,(4.\ 18b)$$

$$a_3 u_{A'}^{n+\frac{1}{2}} + b_3 (u_x)_{A'}^{n+\frac{1}{2}} + c_3 (u_z)_{A'}^{n+\frac{1}{2}} + d_3 u_{G'}^{n} + e_3 (u_x)_{G'}^{n} + f_3 (u_z)_{G'}^{n} + g_3 = 0 . \ (4.\ 18c)$$

Note that, compared to the cavitated bearing expressions, Eqs. (3. 88 a–c), the system obtained here also includes the free terms g_i, i = 1, 2, 3.

The linearized system formed by Eqs (4. 18a), (4. 18b), and (4. 18c) can be solved using an iterative method; note that the coefficients $a_i, b_i, c_i, i = 1,2,3$ are functions of the unknowns $u_{A'}^{n+\frac{1}{2}}, (u_x)_{A'}^{n+\frac{1}{2}}, (u_z)_{A'}^{n+\frac{1}{2}}$. As indicated, the expansion points are selected as shown above, i.e., point A' is the center of the hexagon *BECFDG*, and points E', F', G' are the centers of the corresponding hexagons formed around the neighboring triangular elements. Adding Eqs. (4. 18a), (4. 18b), and (4. 18c) yields a new equation that represents the flux conservation over the hexagon and over the half time step (hexagonal prism in the three dimensional (x, z, t) space). When point A' is the centroid of the hexagon *BECFDG*, this equation has a simpler form given by

$$a_{sum}u_{A'}^{n+\frac{1}{2}} + d_1 u_{E'}^n + e_1 (u_x)_{E'}^n + f_1 (u_z)_{E'}^n + d_2 u_{F'}^n + e_2 (u_x)_{F'}^n + f_2 (u_z)_{F'}^n \\ d_3 u_{G'}^n + e_3 (u_x)_{G'}^n + f_3 (u_z)_{G'}^n + g_{sum} = 0, \tag{4. 19}$$

where a_{sum} is

$$a_{sum} = A_{ABEC} + A_{ACFD} + A_{ADGB} = A_{BECFDG}\,. \tag{4. 20}$$

Equation (4. 19) has only one unknown, $u_{A'}^{n+\frac{1}{2}}$, and can easily be solved explicitly. It is also important to note that all the coefficients in Eq. (4. 19) depend only on the geometry (coordinates of the points) and the values of the dependent variables at the previous half time step so that an iterative method is not needed. After calculating the value $u_{A'}^{n+\frac{1}{2}}$, the values of the other two dependent variables $(u_x)_{A'}^{n+\frac{1}{2}}$ and $(u_z)_{A'}^{n+\frac{1}{2}}$ can be calculated using any two of the expressions Eqs. (4. 18a), (4. 18b), and (4. 18c). This is also called the *a* scheme.

The scheme can be simplified and simultaneously stabilized by calculating the space derivatives in a different way. The scheme thus obtained is called the $a-\varepsilon-\alpha-\beta$ scheme. In this scheme, the derivatives are calculated as weighted averages between the derivatives calculated from the governing equations, as shown above (the *a* scheme), the derivatives calculated using 2-D central difference finite difference formulae (with weight parameter ε) and the derivatives using 2-D side finite differencing (with weight parameter β). Parameter α is the power index used in the computation of the non-linear weighted average that employs 2-D one sided finite differencing. It is important to note that, for a certain value of the weighting parameter ε $(\varepsilon = 0.5)$, the $a-\varepsilon-\alpha-\beta$ scheme eliminates the necessity of calculating the space derivatives from the governing equations, thus the method becomes purely explicit. More details regarding the

computation of the spatial derivatives have been described in section 3. 3. 1.

The feeding system, formed by *ns* orifices, where *ns* equals the number of feeding holes, with the general geometry shown in Fig. 4. 1, can be modeled using a generally accepted formula [Lund, 1964 and 1967] that links the mass flow ratio to the feeding system geometry and the pressures at the ends of the feeding system considering both effects of the orifice restrictor and the inherent restrictor, i.e.,

$$Q_m = \frac{\pi r_{orif}^{\ 2} \sqrt{p_s \rho_s}}{\sqrt{1+\left(\frac{r_{orif}^{\ 2}}{2 r_p\, h}\right)^2}} \overline{Q}_m , \tag{4. 21}$$

where the non-dimensional mass flow $\overline{Q}$ is a fraction C_D of the ideal mass flow,

$$\overline{Q}_m = C_D \begin{cases} \sqrt{\gamma\left(\frac{2}{\gamma+1}\right)^{\frac{\gamma+1}{\gamma-1}}} & for\ \frac{p_i}{p_s} \le \left(\frac{2}{\gamma+1}\right)^{\frac{\gamma}{\gamma-1}}, \\ \sqrt{\frac{2\gamma}{\gamma-1}\left(\frac{p_i}{p_s}\right)^{\frac{2}{\gamma}}\left[1-\left(\frac{p_i}{p_s}\right)^{\frac{\gamma-1}{\gamma}}\right]} & for\ \left(\frac{2}{\gamma+1}\right)^{\frac{\gamma}{\gamma-1}} < \frac{p_i}{p_s} \le 1. \end{cases} \tag{4. 22}$$

When no restricting orifice is present, i.e., an inherent restrictor, see Fig. 4. 2, Eq. (4. 21) becomes

$$Q_m = 2\pi r \sqrt{p_s \rho_s}\, \overline{Q} \tag{4. 23}$$

The restriction characteristic of the feeding system is given by the property that, for a given supply system geometry and supply pressure,

$$p_i = p_i(h) \neq p_s , \tag{4. 24}$$

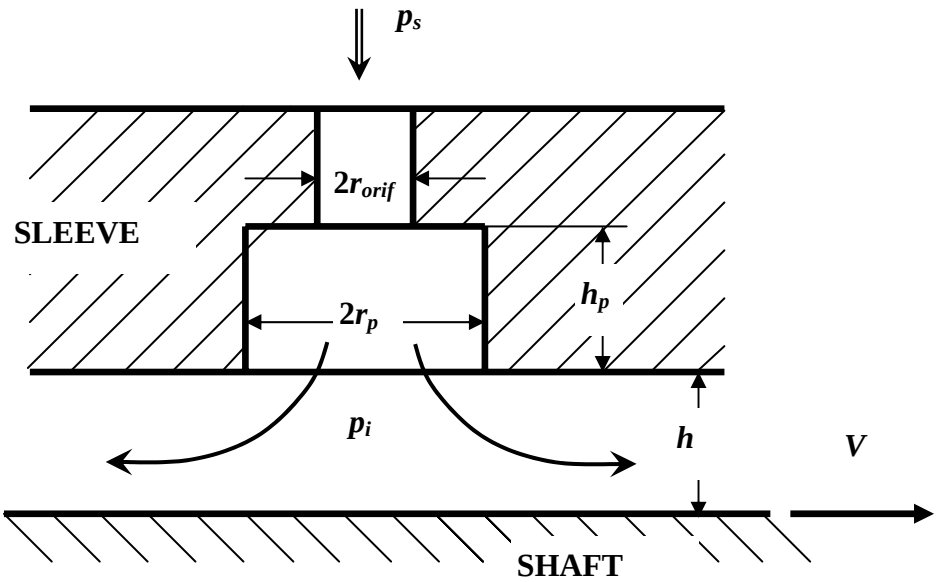

Fig. 4. 1 – Feeding orifice geometry; orifice restrictor

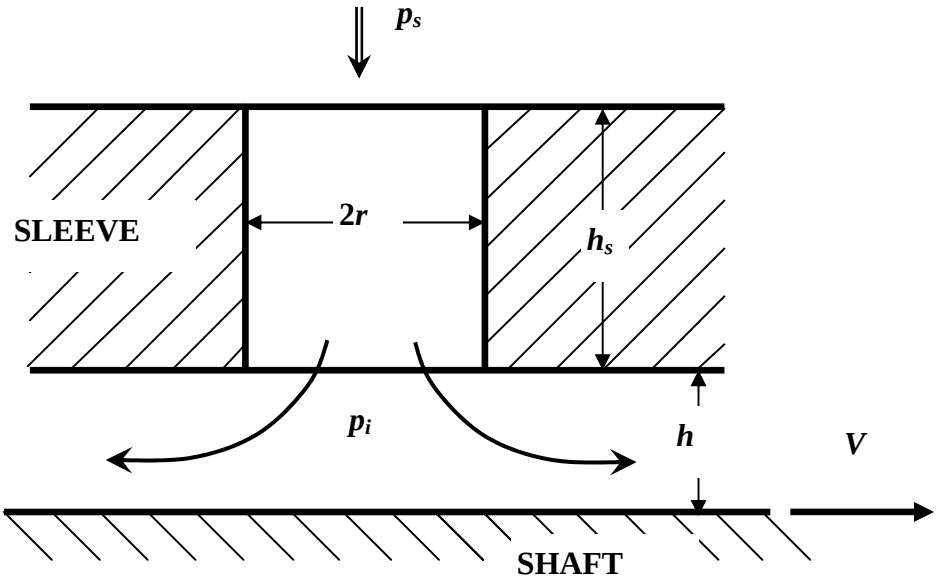

Fig. 4. 2 – Feeding orifice geometry; inherent restrictor

This property is essential in order for the bearing to have rigidity, i.e., the resulting pressure force inside the bearing is a function of the shaft position.

An important feature is given by the fact that the supply holes are relatively small, i.e., too small to be discretized and therefore their surface may be eliminated from the computational domain. For example, a characteristic size of the diameter of the supply holes is 1 mm, for a bearing having the circumference of 100 mm. Consequently, the shape of a supply hole is approximated with the shape of a conservation element, and the pressure is calculated not from the conservation equation, Eq. (4. 4), but using the flow rates through the supply holes given by Eq. (4. 21) or Eq. (4. 23). Thus, on each feeding pocket contour, the mass flow rates calculated from the bearing equations and from the feeding system, respectively, must be equal

$$\left(Q_{m\,i}\right)_{bearing} = \left(Q_{m\,i}\right)_{feeding}\,,\; i = 1, 2, \cdots, ns\,. \tag{4. 25}$$

Equation (4. 25) represents a nonlinear set of *ns* equations, where the pressures in the bearing at the feeding holes are the unknowns $p_i\,, i = 1, 2, \cdots, ns$. This system is solved iteratively using Newton's method. The Jacobian of the system is calculated numerically using first order finite difference approximations.

Another way to introduce the feeding system is to include the feeding flow rates $\left(Q_{m\,i}\right)_{feeding}$ into the governing (Reynolds) equation. In this case, for the mesh elements covering the supply holes, the governing equation, Eq. (4. 4), includes a source term [Wilde and San Andrés, 2003]. While this approach eliminates the need of solving the system given by Eqs. (4. 25), since the pressures p_i are calculated as part of the pressure distribution inside the bearing, it does not improve the convergence of the solution. Indeed, the values of the pressure inside the bearing at the position of the supply holes

have the tendency to oscillate. This tendency is acute especially when the supply flows Q_{mi} are not sensitive enough to the change of the pressures p_i. One example of such case appears when at least some supply holes are choked, i.e., the flow in the supply holes becomes supersonic, and therefore the mass flow rate is not affected by any change of the pressure inside the bearing,

$$\overline{Q}_m = C_D \sqrt{\gamma \left(\frac{2}{\gamma+1} \right)^{\frac{\gamma+1}{\gamma-1}}} = const. \text{ for } \frac{p_i}{p_s} \le \left(\frac{2}{\gamma+1} \right)^{\frac{\gamma}{\gamma-1}} \tag{4. 26}$$

The convergence can be better controlled by using an approach involving the system of equations (4. 25) since this system is solved outside the Reynolds equation solver. For example, the Jacobian of Eq. (4. 25) can be approximated with a diagonal matrix. This is equivalent to considering only the influence of pressure p_i on the flow rate Q_{mi}, and not on other flow rates $Q_{mj}, j \neq i$. Note that this approximation does not influence in any way the accuracy of the converged pressure distribution $p_i, i = 1, \cdots, ns$. This approach was coupled with a variable factor under-relaxation scheme. The method yielded good results in terms of convergence speed and computational effort.

A practical example of the supply system distribution for gas bearings is shown in Figs. 3. 24a and 3. 24b. In these examples, 24 equally spaced supply holes are located within two rows. The two rows are placed symmetrically relative to the bearing center-plane. Outside the bearing sleeve the pressure is equal to the supply pressure p_s, while inside the bearing the pressure is calculated by solving the Reynolds equation, Eq. (4. 4), coupled with the conditions given by Eqs. (4. 25).

4. 4. Applications

A computer code has been developed based on the described method, using the $a-\varepsilon-\alpha-\beta$ scheme with $\varepsilon = 0.5$. This code has been tested for some simple cases where experimental data were available, considering isothermal flow $(k=1)$.

The first case considered was the circular gas bearing without any feeding system. The results are shown in Figs. 4.3a and 4.3b, where the same bearing with an aspect ratio $\frac{L}{2R} = 2.0$ is examined for two bearing numbers $\Lambda = \frac{6\mu\omega R^2}{p_0 C^2}$ and for two eccentricities. There are no significant differences between the experimental and calculated pressure distributions, at least at the middle plane where experimental results are available. The relative differences between the experimental and calculated non-dimensional loads $\zeta = \frac{Load}{p_0 2LR}$ are 3.5% and 4.0%; both of these results represent improvements over the theoretical results of Cooper [1961] as shown by Constantinescu (1969).

The second case considered is the wave journal bearing without any feeding system. The fluid film thickness in an aligned wave bearing has the expression given by Eq. (3. 110). The results are compared with a finite difference based code built by Dimofte (1995). Different bearing positions have been tested and the results (calculated load magnitude and position) are presented in Table 4. 1. The results show very good agreement between the two methods.

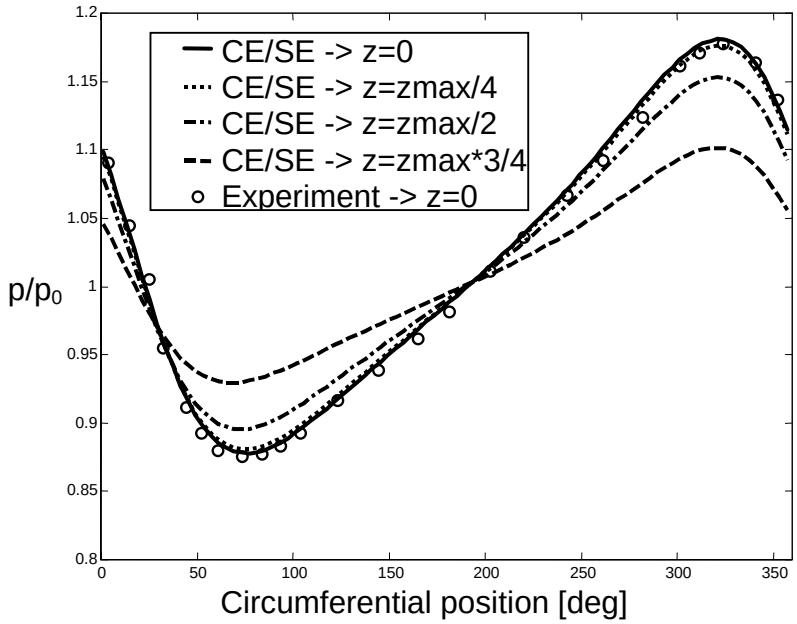

a) $\Lambda = 0.45, \varepsilon_{\exp} = 0.41, \zeta_{\exp} = 0.1496, \theta_{\exp} = 65^0, \varepsilon_{comp} = 0.40, \zeta_{comp} = 0.1548, \theta_{comp} = 69^0$

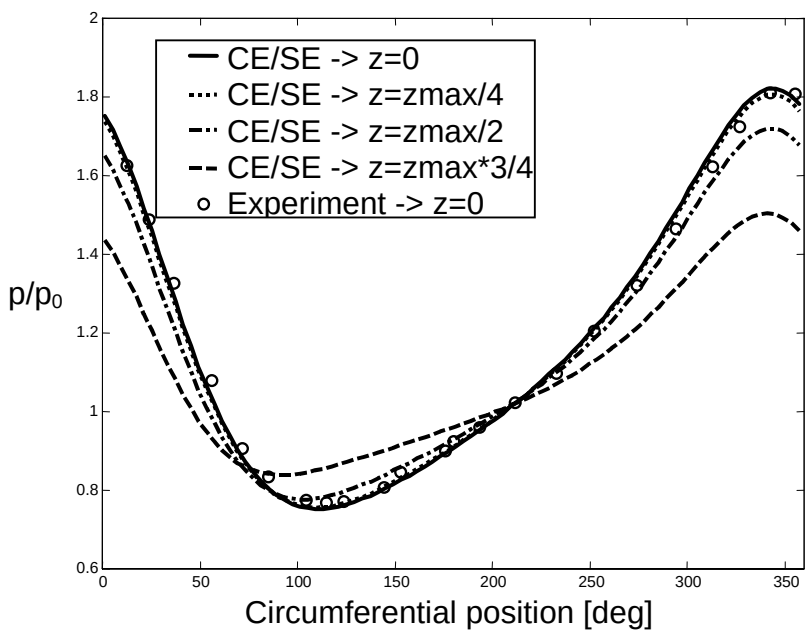

b) $\Lambda = 1.569, \varepsilon_{\exp} = 0.51, \zeta_{\exp} = 0.545, \theta_{\exp} = 37.5^0, \varepsilon_{comp} = 0.51, \zeta_{comp} = 0.567, \theta_{comp} = 38.0^0$

Fig. 4. 3 – Comparison between numerical and experimental results for the pressure distribution in a gas journal bearing

Table 4. 1 – Comparison between calculated data with CE/SE method and with finite difference method

Eccentricity	α_w **(deg)**	**Load CE/SE (N)**	**Load FD (N)**	**Load angle CE/SE (deg)**	**Load angle FD (deg)**
0.502	40	177	177	40.49	40.18
0.460	32	170	170	39.09	38.8
0.433	24	166	165	36.37	36.11
0.416	16	163	162	32.94	32.69
0.404	8	158	158	29.30	29.06
0.400	0	154	154	25.61	25.38
0.404	-8	151	151	22.08	21.86
0.416	-16	149	148	18.95	18.75

The load and load attitude angle shown in Table 4. 1 are also presented in Fig. 4. 4 in order to better compare the two sets of results. Again, very good agreement between the results of the two methods is observed.

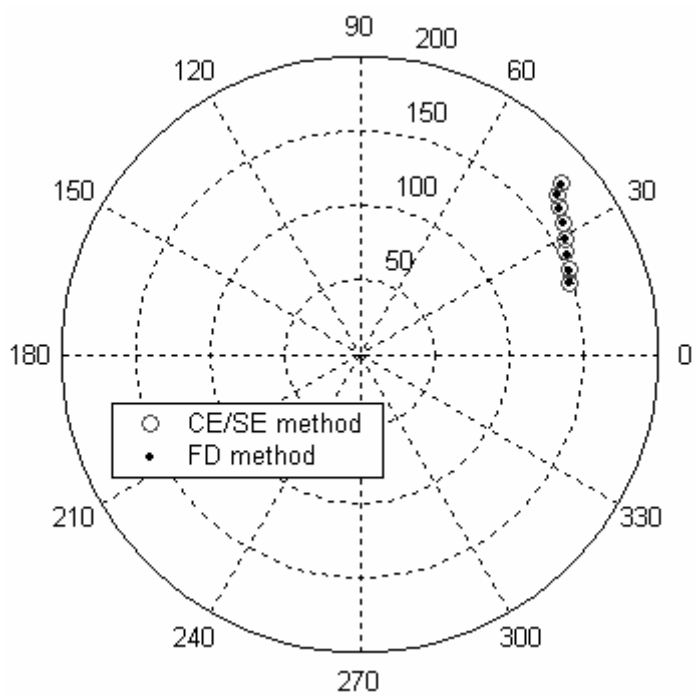

Fig. 4. 4 – Load vs. attitude angle comparison between the present (CE/SE) and finite difference (FD) methods for a gas wave bearing

The third case considered is the pressurized gas bearing without rotation and with zero eccentricity. Details of the bearing geometry and working conditions are presented in Table 4. 2. Figures 4. 5a and 4. 5b show the calculated and experimental pressure distributions for two values of the radial clearance. These cases correspond to the subsonic flow regime (obtained when $C = 12.7\mu m$), and the choked flow regime (obtained when $C = 31.75\mu m$) in the feeding system. Two longitudinal planes situated at the jet position (Fig. 4. 5a) and at half distance between jets (Fig. 4. 5b) are shown; pressure peaks are visible at the jet positions; also a nearly constant pressure is obtained between the supply planes. The predicted pressure peaks at the position of jet are higher than the experimental values (this difference is more visible for the subsonic inlet flow, however it is present in both cases). This is due to the difficulty of measuring the local

pressure at the feeding orifice position. The value for the correction factor C_D is 0.8 for the subsonic inlet flow, and 0.85 for the choked flow.

Table 4. 2 – Pressurized gas bearing geometry and working conditions

Bearing length	117.5 mm
Bearing diameter	60.4 mm
Supply planes	2
Supply plane position	12.7 mm
Holes/supply plane	14
Orifice diameter	0.16 mm
Pocket diameter	0.9 mm
Supply pressure	5.514×10^5 Pa
Injection angle	90^0

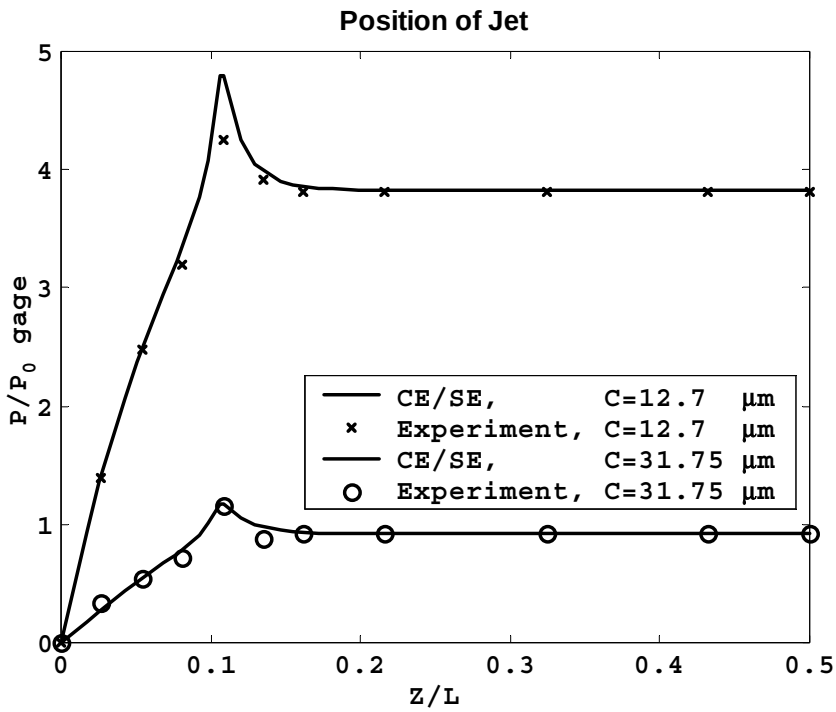

Fig. 4. 5a – Comparison between the calculated and experimental pressure distributions at jet position

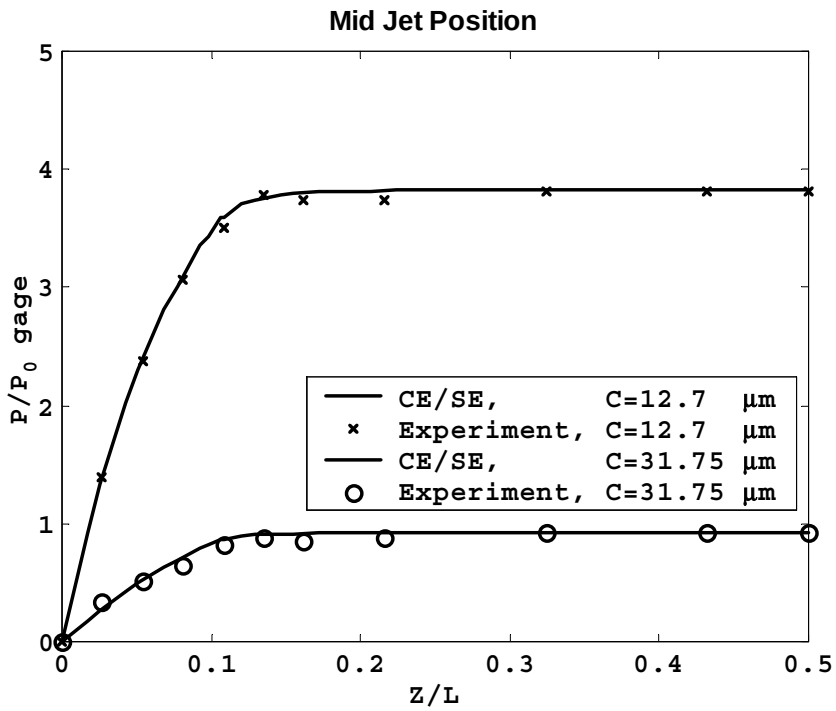

Fig. 4. 5b – Comparison between the calculated and experimental pressure distributions at mid-jet position

Finally, the code was tested for different configurations, where experimental or computed data were not available.

Figure 4. 6 shows the pressure distribution (sections at the jet and at the mid-jet positions) obtained for five supply planes for the same bearing as in the previous case $C = 12.7\mu m$. It is visible that, although the external pressure is the same for all supply holes, the pressure that develops in the pockets (inside the bearing) is not the same for all supply planes. The pressure distribution between two consecutive feeding planes has an almost linear form. Furthermore, at the central supply plane, the peak pressures are not as visible as the peak pressures at the other supply planes; this suggests that the central supply plane does not make an important contribution to the general pressure distribution inside the bearing.

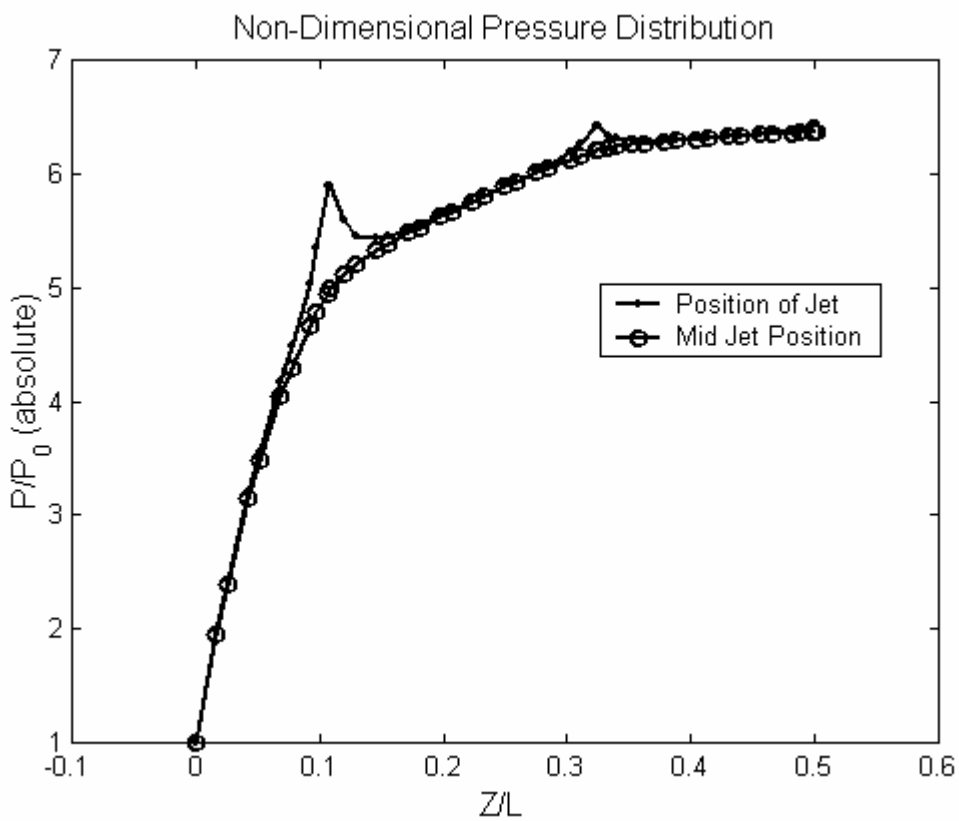

Fig. 4. 6 – Pressure distribution for a circular bearing without eccentricity, with five supply planes

Figure 4. 7 presents the pressure distribution for the same bearing geometry as in the previous two cases, but for a running condition (20,000 *RPM*), at a relative eccentricity $\varepsilon = 0.5$. The pressure distribution is very complex. It may be seen that for some feeding holes the flow is inverted, i.e., it is directed from the bearing towards the feeding system, because the pressure in the bearing is higher than the supply pressure.

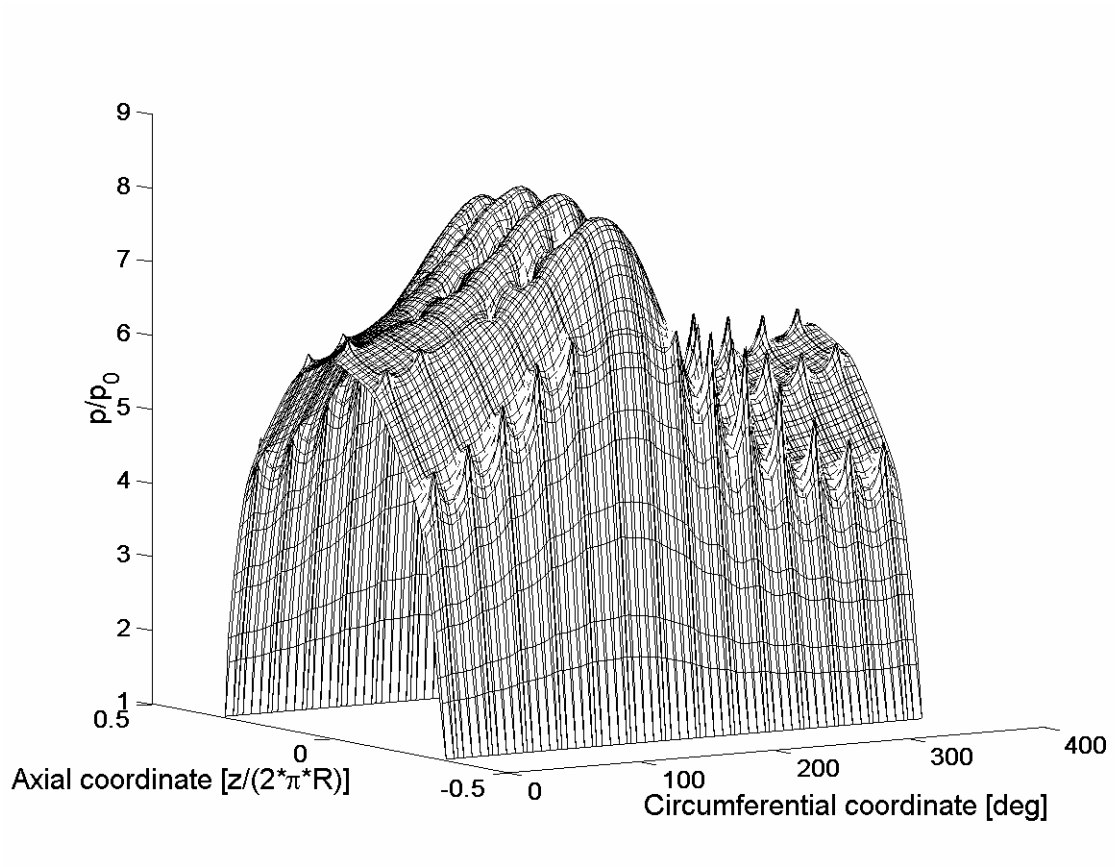

Fig. 4. 7 – Pressure distribution for a circular bearing with eccentricity,

with five supply planes

Chapter Five

Inertial Effects in Gas Bearings

5. 1. Introduction.

As shown in the previous chapter, the computation of the flow in gas bearings is generally accomplished by solving Reynolds equation for compressible flows, and considering the flow as either isothermal or polytropic, or calculating the temperature distribution by using the conservation of energy equation. However, at very high velocities, some of the hypotheses upon which the Reynolds equation have been derived may no longer be valid. Phenomena that do not occur at smaller velocities, such as flow discontinuities, increase the importance of inertial effects, while the characteristic time of heat diffusion can become large compared to the characteristic time of the flow.

This chapter concentrates on the evaluation of inertial effects on steady flow at very high speeds in gas bearings. Some of these effects have been studied in the past. For example, Constantinescu [1995], developed an approximate set of equations that govern the flow in thin fluid films including inertial effects. Szeri et. al., [Dai, Dong, and Szeri, 1992], [Szeri and Al-Sharif, 1995], [Kim and Szeri, 1997], investigated the influence of inertial effects on bearing performance of long oil bearings, with and without cavitation. They showed that for long oil bearings the lubricant inertia has a negligible effect on the

load capacity, and the stability characteristics are slightly influenced by the inertial effects. These conclusions are also substantiated by Constantinescu and Galetuse [1982]. However, You and Lu [1988] indicated that the cavitation boundaries, and consequently the load capacity, can be significantly influenced by the lubricant inertia. Also, Sestieri and Piva [1982] found an important increase in load capacity for non-cavitated bearings when the inertia effects were included. Belforte, Raparelli and Victorov [1999] investigated the dynamic characteristics of gas bearings, including inertial terms, through direct time integration. They concluded that the effects of these terms are negligible when the modified Reynolds number, Re^*, is smaller than unity. An analysis of the inertia effects in fluid film lubrication can be found in Szeri [1998]. Arghir and Frêne, [2001], used a finite volume method to solve the bulk-flow model equations [Childs, 1993]. Shyu, Talmage and Carpino, [2000], showed the limitations of the Reynolds equation and the bulk-flow model. Later, Shyu and Jeng, [2002], proposed a new model, which they called the efficient general fluid-film lubrication model, using the Legendre collocation method [Canuto et. al., 1988] in the cross-film direction, and a finite difference method in the other two directions.

In order to predict the occurrence of discontinuities in the flow, shock-capturing techniques are the most widely used. These methods, opposed to shock fitting techniques, compute the discontinuities as part of the solution for the governing equations, which must be written in conservation form. However, most of the methods have the disadvantage that they can distort the solution when strong shocks are encountered, or even fail in these cases. The authors know of no published results containing flow discontinuities (shock waves) for hydrodynamic gas bearings.

Inertial effects were not included in the application of the space-time conservation element and solution element (CE/SE) method has been successfully applied to calculate the flow in one-dimensional and two-dimensional flows in cavitated oil bearings (Chapter Three), as well as in hybrid (aerodynamic and pressurized) gas bearings (Chapter Four),. Therefore, an objective of the current chapter is to extend the method to include inertial effects for the case of high-speed gas bearings.

5. 2. Governing equations

In order to include the inertial effects, a method by Constantinescu, [1969] and [1995] is used. Consider the continuity and momentum equations written for compressible flows in thin films [Constantinescu, 1995]. Using the continuity equation to rewrite the inertial terms from the momentum equations in conservative form, these equations can be expressed as,

$$\begin{aligned}
&\frac{\partial \rho}{\partial t}+\frac{\partial(\rho u)}{\partial x}+\frac{\partial(\rho v)}{\partial y}+\frac{\partial(\rho w)}{\partial z}=0\\
&\frac{\partial(\rho u)}{\partial t}+\frac{\partial(\rho u^2)}{\partial x}+\frac{\partial(\rho uv)}{\partial y}+\frac{\partial(\rho uw)}{\partial z}=-\frac{\partial p}{\partial x}+\frac{\partial}{\partial y}\left(\mu\frac{\partial u}{\partial y}\right),\\
&0=-\frac{\partial p}{\partial y},\\
&\frac{\partial(\rho w)}{\partial t}+\frac{\partial(\rho uw)}{\partial x}+\frac{\partial(\rho vw)}{\partial y}+\frac{\partial(\rho w^2)}{\partial z}=-\frac{\partial p}{\partial z}+\frac{\partial}{\partial y}\left(\mu\frac{\partial w}{\partial y}\right).
\end{aligned} \tag{5. 1}$$

In Eqs. (5. 1), u, v, w are the gas velocity components in x, y, and z directions, respectively. Let the x velocity component be the sum of a linear and parabolic profile, i.e.,

$$u=V\left(1-\frac{y}{h}\right)+\frac{6U}{h^2}y(h-y). \tag{5. 2}$$

This distribution assumes that the inertia forces do not alter the shape of the velocity profile, i.e., the laminar profile. It is easily seen that the linear component is the Couette distribution, with one surface $(y = h)$ being fixed, and the other surface $(y = 0)$ having a translation motion with the velocity *V*, where $V = \omega R$ for journal bearings. The parabolic component is symmetric, with the volumetric flow rate per unit of length in the *z* direction given by,

$$Flow = \int_0^h \frac{6U}{h^2} y(h - y)\mathrm{d}y = Uh\,. \tag{5. 3}$$

This equation shows that the velocity $U(x, z)$ is in fact the average parabolic velocity in the *x* direction. The total velocity in *x* direction (after adding the Couette component), averaged on the film thickness, is,

$$U_m = U + \frac{V}{2}\,. \tag{5. 4}$$

The *z* velocity component is assumed to have only a parabolic profile,

$$w = \frac{6W}{h^2} y(h - y)\,. \tag{5. 5}$$

The system of equations Eq. (5. 1), can be integrated across the film, i.e., from $y = 0$ to $y = h(x, z, t)$, assuming that *p*, ρ, and μ do not vary with *y*, and utilizing the assumed velocity profiles given by Eqs. (5. 2) and (5. 5). This yields,

$$\frac{\partial(\rho h)}{\partial t} + \frac{\partial}{\partial x}\left[\rho h\left(\frac{V}{2} + U\right)\right] + \frac{\partial}{\partial z}(\rho h W) = 0\,, \tag{5. 6a}$$

$$\frac{\partial}{\partial t}\left[\rho h\left(U + \frac{V}{2}\right)\right] + \frac{\partial}{\partial x}\left[\rho h\left(\frac{6}{5}U^2 + UV + \frac{1}{3}V^2\right)\right] + \frac{\partial}{\partial z}\left[\rho h W\left(\frac{6}{5}U + \frac{1}{2}V\right)\right] = -h\frac{\partial p}{\partial x} - \frac{12\mu}{h}U\,, \tag{5. 6b}$$

$$\frac{\partial}{\partial t}(\rho h W)+\frac{\partial}{\partial x}\left[\rho h W\left(\frac{6}{5}U+\frac{1}{2}V\right)\right]+\frac{\partial}{\partial z}\left(\frac{6}{5}\rho h W^{2}\right)=-h\frac{\partial p}{\partial z}-\frac{12\mu}{h}W\,. \tag{5. 6c}$$

For turbulent flows the velocity profile is usually considered flat, as in the bulk-flow analysis, [Childs, 1993]. This yields a set of equations with the same structure as given by Eqs. (5. 6a-c), but with slightly different numerical coefficients. Consequently, the results obtained are close to the laminar flow results, except for the variables strongly influenced by the velocity profile, as the shear stress at the wall. Since this work only deals with the pressure and average velocity distributions, the laminar flow assumption is not critical in this phase. In addition, using the laminar velocity profile allows comparison with the non-inertial computations. Also, in the literature the system of equations, Eqs. (5. 6a-c), is usually, [Constantinescu, 1995], [Szeri, 1998], written in terms of velocity U_m given by Eq. (5. 4) instead of U. There are absolutely no conceptual differences between the two forms, but here the use of U has been preferred because only this component in the total velocity in x direction carries the information regarding inertial effects. Indeed, assuming that the left hand sides of the momentum equations, i.e., Eqs. (5. 6b) and (5. 6c) are zero (negligible), which is equivalent to considering that the inertial effects are negligible, the momentum equations become,

$$U=-\frac{h^{2}}{12\mu}\frac{\partial p}{\partial x}\,, \tag{5. 7a}$$

$$V=-\frac{h^{2}}{12\mu}\frac{\partial p}{\partial z}\,. \tag{5. 7b}$$

These values correspond to the Poiseuille flow, and are used in the Reynolds equation. When including the inertial effects, Eqs. (5. 7a) and (5. 7b) are no longer valid.

Keeping the conservative form, and using non-dimensional variables, the system described by Eqs. (5. 6a-c) can be written as,

$$\frac{\partial Q}{\partial \bar{t}} + \frac{\partial F}{\partial \bar{x}} + \frac{\partial G}{\partial \bar{z}} = H \,, \tag{5. 8}$$

where the unknown vector Q has the components,

$$\begin{aligned} Q_1 &= \bar{\rho}\bar{h}, \\ Q_2 &= \bar{\rho}\bar{h}\left(\bar{U} + 1\right), \\ Q_3 &= \bar{\rho}\bar{h}\bar{W}. \end{aligned} \tag{5. 9}$$

The flux vector in the x-direction has the components,

$$\begin{aligned} F_1 &= Q_2, \\ F_2 &= 1.2\frac{Q_2^2}{Q_1} - 0.4Q_2 + \frac{8}{15}Q_1, \\ F_3 &= Q_3\left(1.2\frac{Q_2}{Q_1} - 0.2\right). \end{aligned} \tag{5. 10}$$

The flux vector in the z-direction has the components,

$$\begin{aligned} G_1 &= Q_3, \\ G_2 &= F_3, \\ G_3 &= 1.2\frac{Q_3^2}{Q_1}, \end{aligned} \tag{5. 11}$$

Instead of the energy equation, the polytropic equation is utilized

$$\bar{p} = \frac{p}{p_0} = \left(\frac{\rho}{\rho_0}\right)^k = \bar{\rho}^k = \left(\frac{Q_1}{\bar{h}}\right)^k . \tag{5. 12}$$

This enables the source terms to be written as,

$$H_1 = 0,$$
$$H_2 = -C_A h \frac{\partial}{\partial \bar{x}} \left(\frac{Q_1}{\bar{h}} \right)^k - \frac{C_B}{\bar{h}} \left(\frac{Q_2}{Q_1} - 1 \right), \tag{5. 13}$$
$$H_3 = -C_A h \frac{\partial}{\partial \bar{z}} \left(\frac{Q_1}{\bar{h}} \right)^k - \frac{C_B}{\bar{h}} \frac{Q_3}{Q_1}.$$

In the following, the non-dimensional notation (upper bar) is dropped for convenience. The constants C_A, C_B are

$$C_A = \frac{4 p_0}{\rho_0 \omega^2 R^2}, \; C_B = \frac{48 \pi \mu}{\omega \rho_0 C^2} \tag{5. 14a}$$

Unlike the case of the classic Reynolds equation, the steady form of the governing equation is influenced not only by one parameter, the bearing number, but instead by two parameters: C_A and C_B. These two parameters can be written in terms of the bearing number Λ and modified Reynolds number Re* as

$$C_A = \frac{24}{\mathrm{Re}^* \Lambda}, \; C_B = \frac{48\pi}{\mathrm{Re}^*} \tag{5. 14b}$$

5. 3. Numerical formulation

The numerical formulation is in many ways similar to the procedures described in sections 3.3.1. and 5.3. There are some notable differences however. The first difference is related to the fact that in this case (with the inclusion of the inertial effects) the governing equations are a system of equations, instead of only a single equation, and the unknowns are vectorial variables, instead of scalar variables. Therefore, in the numerical procedure, variable u from the previous cases is now replaced by vector Q, and fluxes f and g are replaced by three dimensional fluxes F and G. Also, the spatial derivatives, Q_x, Q_z, F_x, F_z, etc., are in this case vectorial variables, instead of scalar variables, as before.

While the appearance of the formulation is virtually identical, the meaning of the notations is now different, i. e., the unknowns are multidimensional.

The second difference is related to the fact that this is the first case considered in this thesis when a source term, vector *H*, is present. However, a source term is present in the axial-symmetric formulations which have not been discussed here. The source term is evaluated using only information from the previous time step. For stiff problems, it would be necessary to evaluate the source term using an iterative procedure, i.e., an implicit formulation. This is not the situation for the case studied. In addition, only the transient solution could be different using the two procedures, while the steady state solution is the same.

As with the development of previous cases, consider a triangular grid that covers the computational domain $x=[0,1]$, $z=[-L/(4\pi R), L/(4\pi R)]$. The domain can be divided in half in the case of symmetric bearings $z=[0, L/(4\pi R)]$. As shown in Fig. 3.18, consider a triangular element *BCD* and its three neighbors *BHC*, *CID*, and *DJB*. Let *A* be the centroid of element *BCD*, and *E*, *F* and *G* be the respective centers of the neighbor elements. Also let *A'* (not shown in the figure) be the centroid of the hexagon *BECFDG*, and *E'*, *F'* and *G'* be the centers of the hexagons formed around the neighbor elements (not shown in the figure). In order to solve the governing equation, Eq. (5. 8), using the CE/SE numerical scheme, the following steps have been followed:

(a) The governing equation is integrated over the surface of the hexagon *BECFDG* and in time between two consecutive time steps t^n and t^{n+1}, i.e.,

$$\iint_{BECFDG} \int_{t^n}^{t^{n+1}} \frac{\partial Q}{\partial t} \mathrm{d}t\,\mathrm{d}x\mathrm{d}z + \int_{t^n}^{t^{n+1}} \iint_{BECFDG} \left(\frac{\partial F}{\partial x} + \frac{\partial G}{\partial z} \right) \mathrm{d}x\mathrm{d}z\,\mathrm{d}t = \iint_{BECFDG} \int_{t^n}^{t^{n+1}} H\,\mathrm{d}t\,\mathrm{d}x\mathrm{d}z \qquad (5.\ 15)$$

(b) The volume integrals in Eq. (5. 15) are changed into surface integrals, assuming linear dependence with time for functions *F*, *G*, and *H*, i.e.,

$$\iint_{BECFDG}\left(Q^{n+1}-Q^{n}\right)\mathrm{d}x\mathrm{d}z+\Delta t\iint_{BECFDG}\left(\frac{\partial F}{\partial x}+\frac{\partial G}{\partial z}\right)^{n+1/2}\mathrm{d}x\mathrm{d}z=\Delta t\iint_{BECFDG}H^{n+1/2}\,\mathrm{d}x\mathrm{d}z \quad (5.\ 16)$$

(c) The second integral in the left hand side of Eq. (5. 16) is changed into a contour integral using Green's theorem. Thus, Eq. (5. 17) becomes

$$\iint_{BECFDG}\left(Q^{n+1}-Q^{n}\right)\mathrm{d}x\mathrm{d}z+\Delta t\oint_{BECFDG}\vec{\mathrm{F}}\cdot\vec{\mathrm{n}}\,\mathrm{d}s=\Delta t\iint_{BECFDG}H^{n+1/2}\,\mathrm{d}x\mathrm{d}z\,, \quad (5.\ 17)$$

(d) The unknown vector *Q*, the flux functions *F* and *G*, and the source term *H* are written in linear form in terms of *x*, *z*, and *t* using Taylor series expansions. For example, the unknown vector *Q* is approximated as,

$$\begin{aligned}Q_i&=\left(\frac{\partial Q_i}{\partial x}\right)_0(x-x_0)+\left(\frac{\partial Q_i}{\partial z}\right)_0(z-z_0)+\left(\frac{\partial Q_i}{\partial t}\right)_0(t-t_0)\\&=\left(\frac{\partial Q_i}{\partial x}\right)_0(x-x_0)+\left(\frac{\partial Q_i}{\partial z}\right)_0(z-z_0)+\left[(H_i)_0-\left(\frac{\partial F_i}{\partial x}\right)_0-\left(\frac{\partial G_i}{\partial z}\right)_0\right](t-t_0).\end{aligned} \quad (5.\ 18)$$

where $(i=1,2,3)$, and the expansion point (x_0,z_0,t_0) is chosen in a suitable way, as shown later. Also for illustration, component *i* of the flux function *F* is approximated as

$$F_i\cong\left(\frac{\partial F_i}{\partial x}\right)_0(x-x_0)+\left(\frac{\partial F_i}{\partial z}\right)_0(z-z_0)+\left(\frac{\partial F_i}{\partial t}\right)_0(t-t_0), \quad (5.\ 19)$$

where the partial derivatives can be written in terms of the partial derivatives of the unknown *Q*, or they can be evaluated numerically using a finite difference scheme. For example, in terms of the *Q* gradient components,

$$\left(\frac{\partial F_i}{\partial x}\right)_0=\sum_{j=1}^{3}\left(\frac{\partial F_i}{\partial Q_j}\right)_0\left(\frac{\partial Q_j}{\partial x}\right)_0. \quad (5.\ 20)$$

Equations (5. 20), and those similar to them, provide relatively simple analytical forms for the gradient components of the fluxes (written in terms of the *Q* gradient components), but they may neglect some terms related to the film thickness gradients, as in the case of the source term, *H*. In these cases, this approximation is equivalent to the assumption that the film thickness is constant on the surface of each conservation element. In practice, no differences have been found between using the approximations given by Eqs. (5. 20) and the numerical evaluation of these gradient components.

The integrals that appear in Eq. (5. 17) are evaluated dividing the contour integral into a sum of six segment integrations, and dividing the surface integrals at time steps t^n or $t^{n+1/2}$ into a sum of three surface integrals over the areas *ABEC*, *ACFD*, and *ADGB*. Note that the integral $\iint_{BECFDG} Q^{n+1}\mathrm{d}x\mathrm{d}z$ is not divided, rather it is approximated as,

$$\iint_{BECFDG} Q^{n+1}\mathrm{d}x\mathrm{d}z = Q_{A'}^{n+1} S_{BECFDG} \tag{5. 21}$$

This approximation is in accordance to the linear approximation of the unknown *Q*, considering that point *A'*, the centroid of the hexagon *BECFDG*, coincides with the expansion point.

(e) The remaining expansion points are selected as follows

- For all integrals that contain segments *BE* or *EC* at the time t^n or $t^{n+1/2}$, the expansion point is *E'* for all evaluates and the corresponding time is t^n.

- Similarly, when segments *CF* or *FD* are part of either surface or contour integrations, point is *F'* is used as the expansion point, and when segments *DG* or *GB* are part of the surface or contour integrations, point is *G'* is used as the expansion point.

(f) The discrete equation obtained is entirely explicit, so that the unknown vector at the new time step Q^{n+1} can be readily evaluated for all hexagon centroids. The space derivatives at the new time step can then be evaluated using the procedure described in the previous cases.

The boundary conditions consist of periodic conditions for all variables at one circumferential position, the symmetry condition for all variables at the axial center plane, and imposed pressure, that is equal to atmospheric pressure, at the edge of the bearing. At the bearing edge, the velocities *U* and *W*, and also the spatial derivatives, are calculated from the field, satisfying the conservation condition, non-reflective boundary conditions [Chang et. al, 1997]. In essence, the computational domain is extended to include a row of ghost elements equal to their pair (neighboring) elements. The unknowns at the ghost elements (Q_2, Q_3 and the spatial derivatives) can, for example, be considered to be equal to the values from their neighboring pair elements. This insures that the fluxes which cross each interior element situated near the boundary leave the computational domain through the boundary of the ghost elements, and thus are not reflected.

5. 4. Applications

A computer code has been developed based on the described method. This code has been tested for some simple isothermal flow cases where experimental data or theoretical data were available. Also, the results obtained with this code for low velocities, where inertia effects are small, have been compared with the results obtained

with the code that solves the classic Reynolds equation, presented in Chapter Four, [Cioc, Keith, Dimofte and Fleming, 2003].

The first case considered is the circular journal bearing. The results are shown in Figs. 5. 1 and 5. 2, where the same bearing with an aspect ratio $L/2R = 2$ is examined for two bearing numbers, Λ, and for two relative eccentricities, ε.

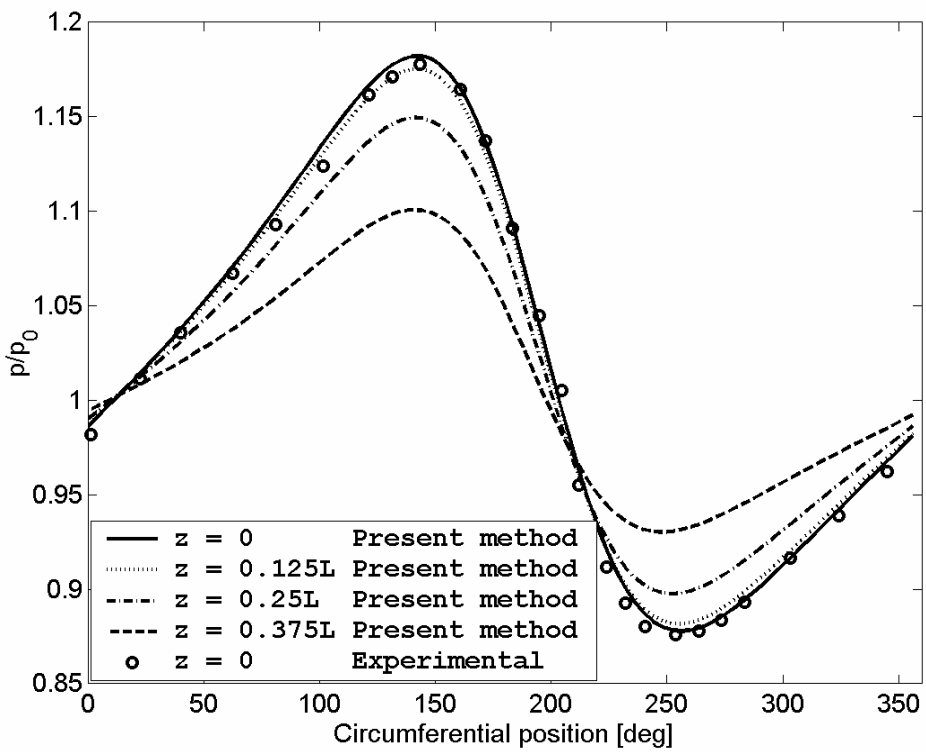

Fig. 5. 1 – Comparison between numerical and experimental results for the pressure distribution in a gas journal bearing
$\Lambda = 0.45, \varepsilon_{\exp} = 0.41, \zeta_{\exp} = 0.1496, \theta_{\exp} = 65^0, \varepsilon_{comp} = 0.40, \zeta_{comp} = 0.1540, \theta_{comp} = 69^0$

As may be observed, there are no significant differences between the experimental and calculated pressure distributions at the middle-plane where experimental data are available [Constantinescu, 1969], [Cooper, 1961]. The relative differences between the experimental (denoted with subscript exp) and calculated (subscript comp) non-

dimensional loads ζ are 3% and 4%, and are in very good agreement with the results obtained using the code discussed in the previous chapter, that was developed for cases without including inertia effects.

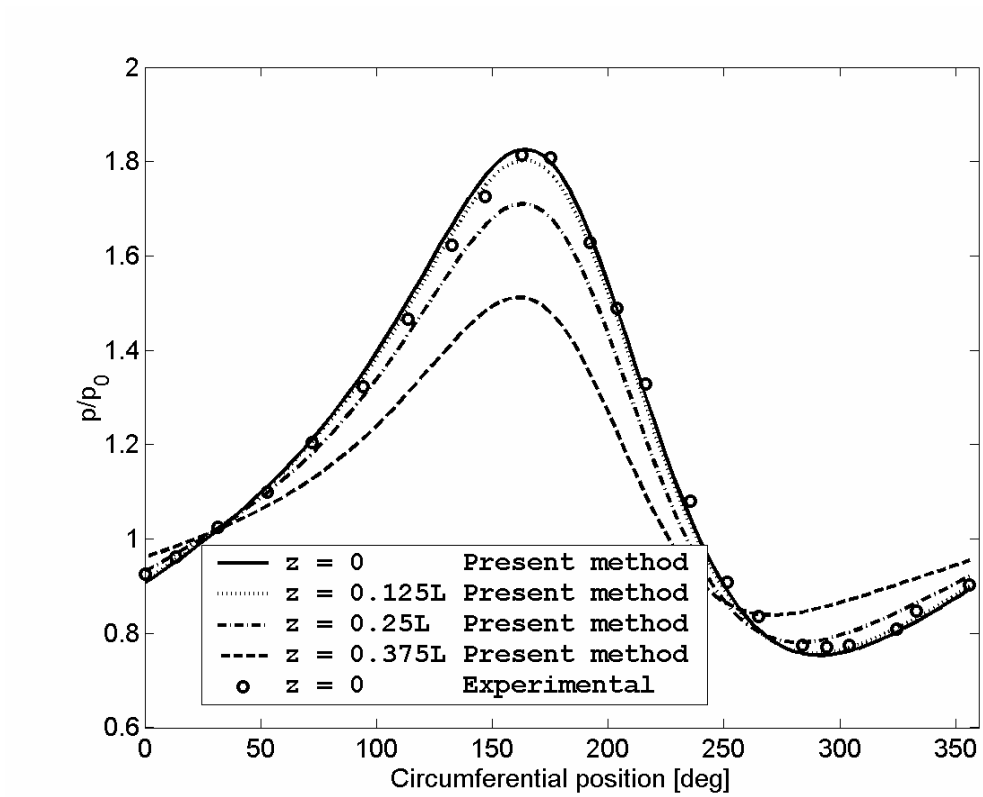

Fig. 5. 2 – Comparison between numerical and experimental results for the pressure distribution in a gas journal bearing
$\Lambda = 1.569, \varepsilon_{\exp} = 0.51, \zeta_{\exp} = 0.545, \theta_{\exp} = 37.5^0, \varepsilon_{comp} = 0.51, \zeta_{comp} = 0.5676, \theta_{comp} = 38.0^0$

The second validation case considered is a plane slider with $\Lambda = \dfrac{6\mu VL}{p_0 h_1^2} = 1$, where V is the velocity of the lower surface and h_1 is the fluid film thickness at the entrance. The slope of the slider is small, $\varepsilon = 0.01$ because the results are compared to results of the small perturbations theory of Constantinescu, [1995]. The one-dimensional gage

pressure distributions along the slider, for different values of the parameter

$\alpha' M = \sqrt{\frac{2}{3}} \frac{V}{2\sqrt{p_0/\rho_0}}$, are shown in Fig. 5. 3.

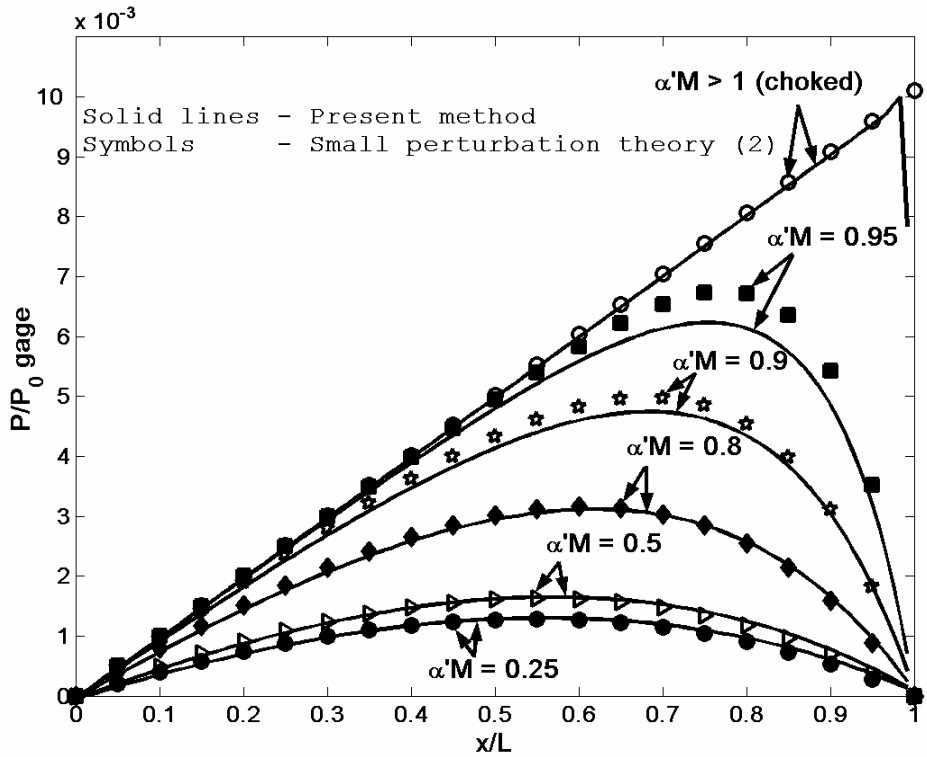

Fig. 5. 3 – Comparison between numerical and small perturbation theory [Constantinescu, 1995] results for a plane slider,

$$\Lambda = \frac{6\mu VL}{p_0 h_1^2} = 1.0\,,\ \alpha' M = \sqrt{\frac{2}{3}} \frac{V}{2\sqrt{p_0/\rho_0}}\,.$$

For small values of the parameter, $\alpha' M = 0.25$, the flow is almost non-inertial, and the theoretical results agree very well with the numerical values. As $\alpha' M$ increases, the peak pressure increases and moves towards the slider exit because the inertial effects become more important. Indeed, keeping the value of the bearing number constant, $\Lambda = C_A / C_B = 1$ and changing the value of the "Mach" number $M = \frac{V}{2\sqrt{p_0/\rho_0}} = \frac{1}{\sqrt{C_A}}$ is

equivalent to changing the weight of the inertial effects, but not the relative proportion between the pressure gradient and viscous forces in the momentum equations. Therefore, when $\alpha' M$ increases, both coefficients C_A and C_B decrease at the same rate, so that the right hand sides of the momentum equations, Eqs. (5. 6b, c), decrease at the same rate, and the left hand sides (which include only the inertial effects) become relatively more important. The numerical and theoretical results continue to agree very well to $\alpha' M = 0.8$. For higher values, $\alpha' M > 0.9$, there is an increased difference between the two sets of results. At $\alpha' M = 0.95$ for example, the peak gage pressure differs by about 7.5%, but the position of the peak pressure remains in very good agreement. It is surmised that these differences are due mostly to the limitations of the small perturbations theory, which cancels some terms in the governing equations. These terms can become important when the inertial effects increase. For choked flows, $\alpha' M > 1$, the results agree again very well, since this case is treated separately by the small perturbations theory as a limiting case. For choked flows the pressure is discontinuous at the bearing exit, as seen in Fig. 5. 3, and is not influenced by the value of the parameter $\alpha' M$. Based on the results of this analysis, it may be concluded that the capability of the CE/SE method to accommodate a discontinuity on the boundary is outstanding.

In order to show the impact of the inertial effects on the pressure distribution at very high speeds in journal bearings, a series of cases were run starting from a fixed bearing geometry, i.e., $L = 2R = 35\,\text{mm}$, $C = 40 \cdots 100\,\mu m$,

$\dot{n} = 2{,}094 \cdots 41{,}890\, s^{-1} = (20 \cdots 400) \cdot 10^3\,\text{rev/min}$.

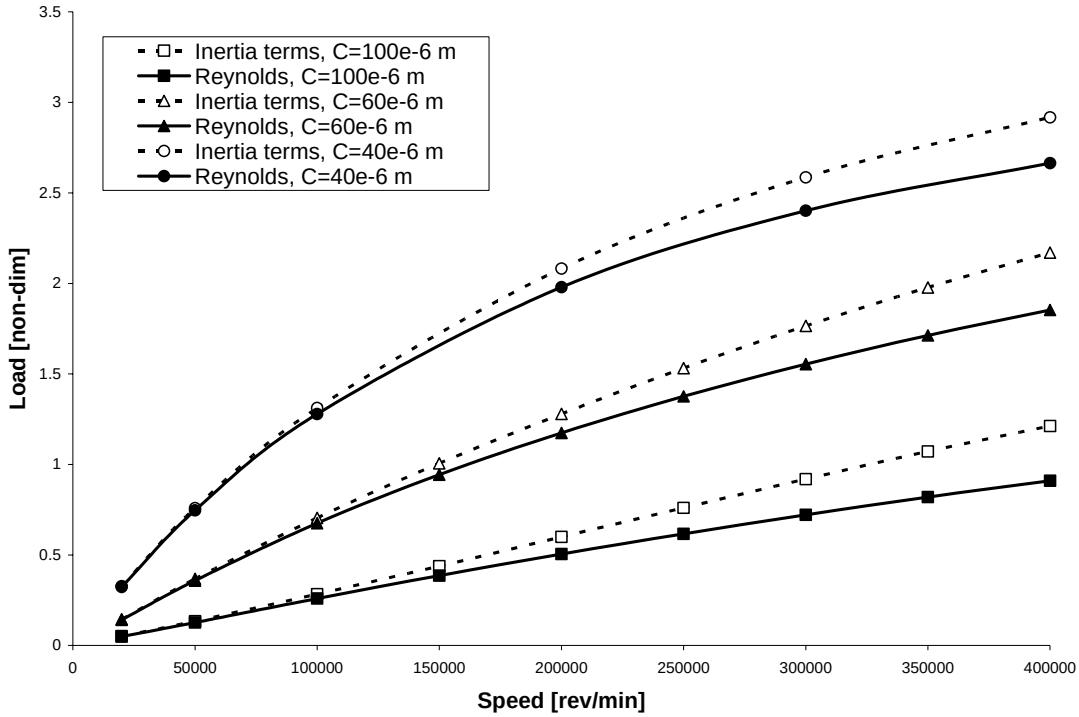

Fig. 5. 4 – Comparison between the non-dimensional loads vs. shaft speed with and without inertial effects for three radial clearances $\varepsilon = 0.8$

Figure 5. 4 shows the non-dimensional load distribution, $\zeta = \dfrac{Load}{p_0 2LR}$, as function of the bearing speed at constant eccentricity ratio $\varepsilon = 0.8$ for three values of the bearing clearance, with and without inertial effects. It may be observed that the inertial effects become more important when the speed is increased, while for low speeds the differences become negligible. This conclusion was expected. Also, Fig. 5. 4 reveals that the difference between the two methods is more significant for larger radial clearances. At the same time, predictions of the attitude angle (the angle between the direction of the load and the centerline axis) using the two methods does not yield much difference, as shown in Fig. 5. 5.

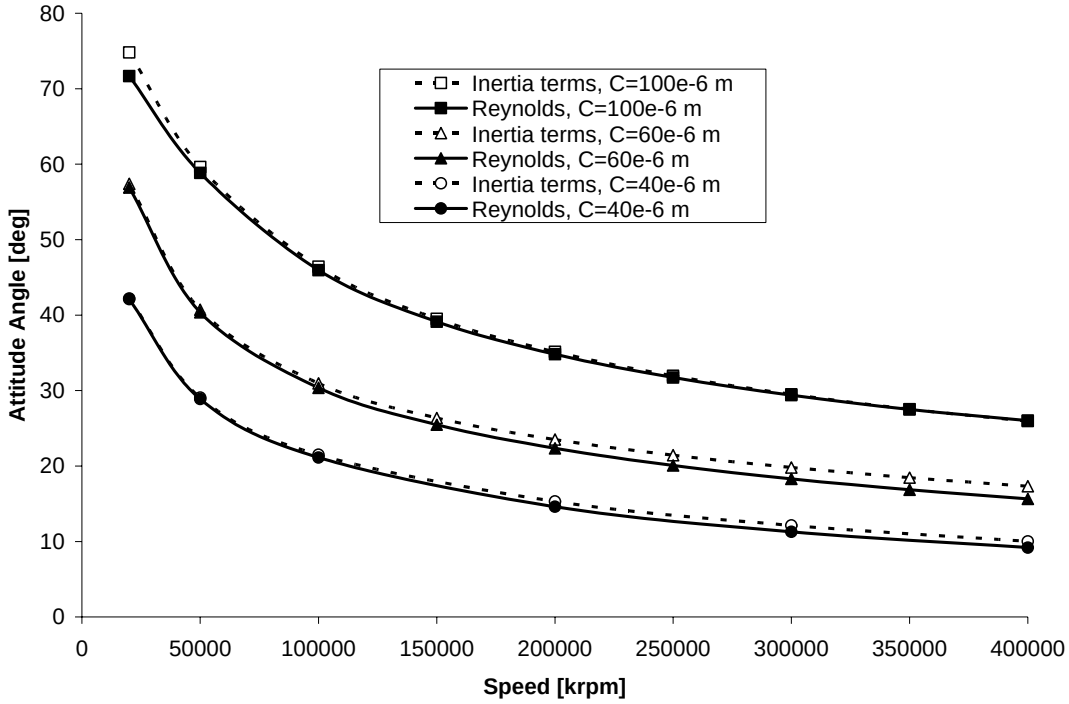

Fig. 5. 5 – Comparison between the attitude angles vs. shaft speed with and without inertial effects for three radial clearances, $\varepsilon = 0.8$

A better sense of the differences between the two cases (with and without inertial effects), is offered by Fig. 5. 6, which presents the relative error in the load evaluation between the two methods. The error is minimal (under 1.3%) for low speeds and low clearances, and it increases both with speed and the value of the radial clearance. For $C = 100\mu m$ the error is higher than 4% for a shaft speed of 20,000 rev/min $\left(\mathrm{Re}^* = 1.39, \Lambda = 0.0699\right)$, and it increases up to almost 25% at 400,000 rev/min $\left(\mathrm{Re}^* = 27.9, \Lambda = 1.398\right)$. This observation indicates that the increase of the bearing clearance leads to an increase of the inertial effects, which can become fairly important.

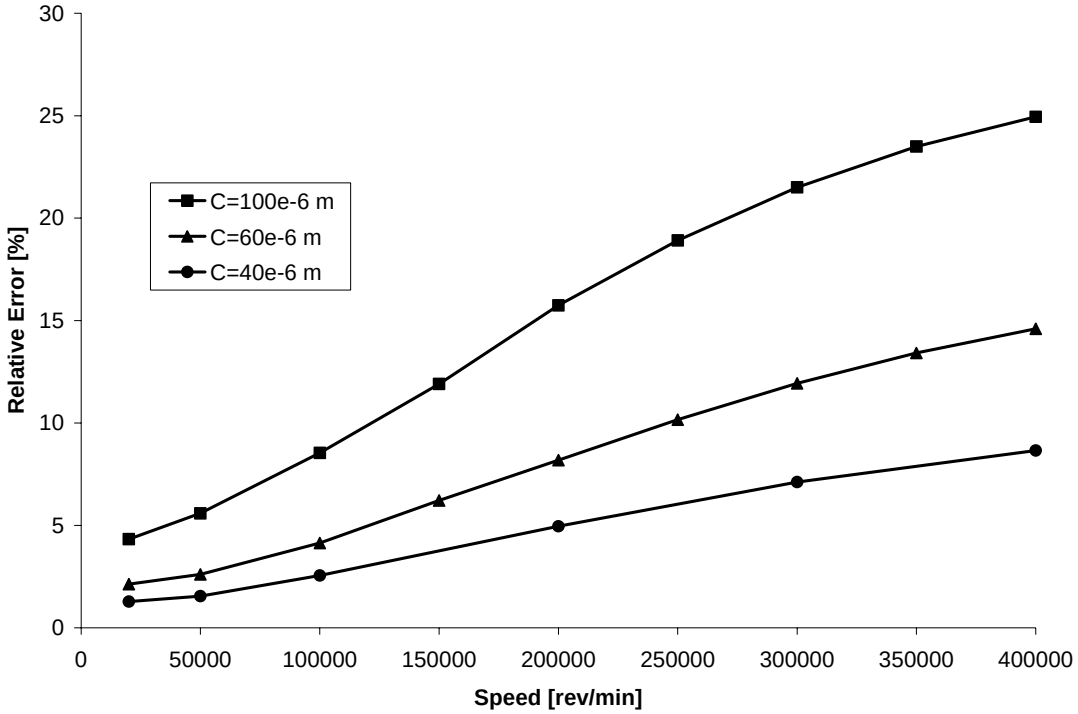

Fig. 5. 6 – Comparison between the relative difference of the loads with and without inertial effects vs. shaft speed for three radial clearances; $\varepsilon = 0.8$

Figure 5. 7 shows a comparison between the loads calculated with the two methods for a fixed clearance of 100μm and shaft speed 350,000 rev/min $\left(\mathrm{Re}^{*} = 24.4, \Lambda = 1.223\right)$. The absolute difference between the loads increases with an increase of the bearing eccentricity ratio. However, the relative difference does not change much, having values of about 23% over most of the range of eccentricities considered.

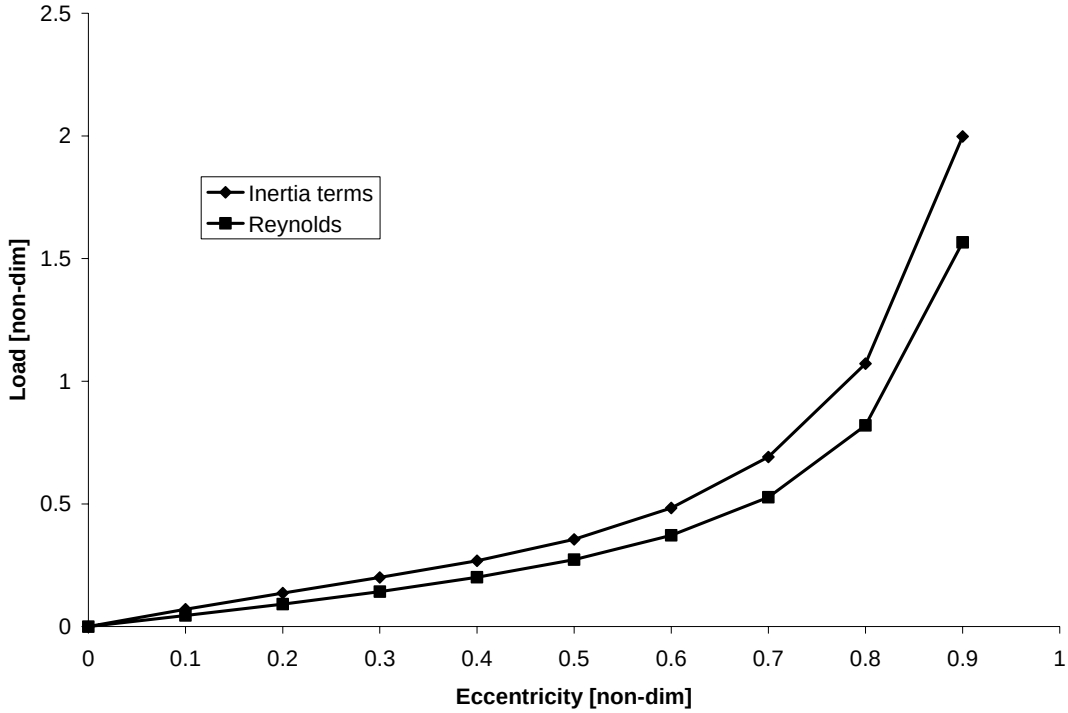

Fig. 5. 7 – Comparison between the loads with and without inertial effects vs. eccentricity ratio; $\Lambda = 1.223$ and $\mathrm{Re}^* = 24.4$, $C = 100\mu m$, $\dot{n} = 350{,}000\,\mathrm{rev/min} = 36{,}652\,\mathrm{s}^{-1}$

It is well known that the steady state solution of the Reynolds equation is a function of one parameter only, which is the bearing number, Λ. This is not the case when the inertial effects are included. Figure 5. 8 shows the same load values as in Fig. 5. 4, but this time presented in terms of the bearing number. It may be observed that all results calculated with the classic Reynolds equation are located on the same curve. When considering the inertial effects however, three different curves are obtained, correspondent to the three values of the clearance considered. Again it is seen that an increase of the clearance produces larger disparities from the non-inertial case.

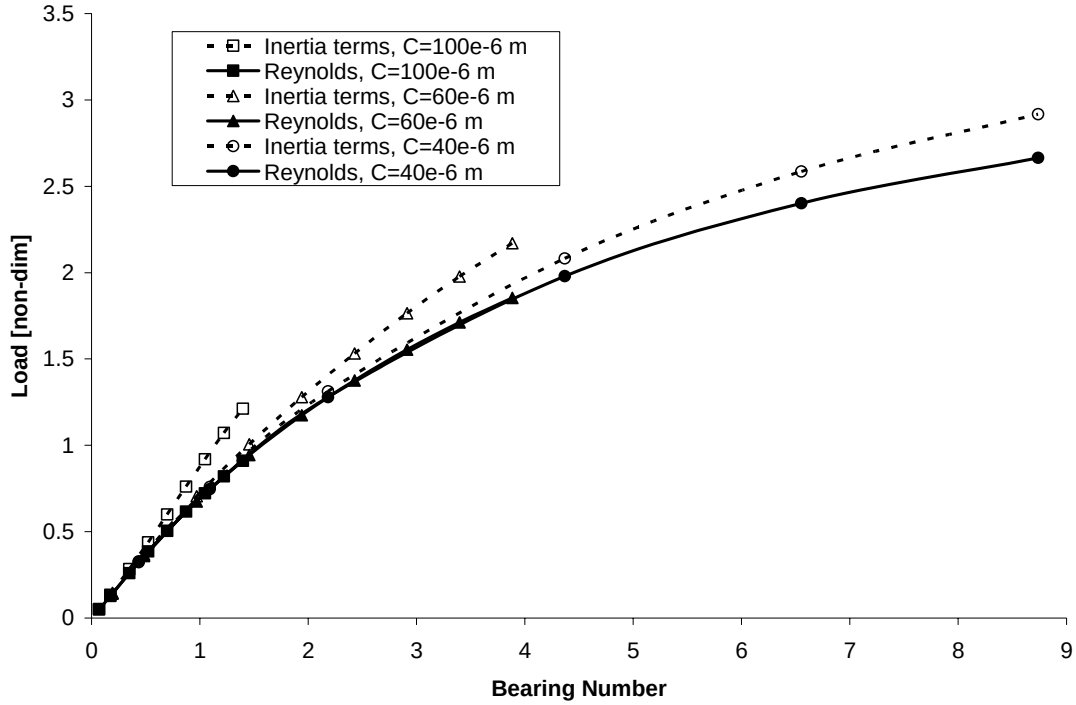

Fig. 5. 8 – Comparison between the non-dimensional loads vs. bearing number with and without inertial effects for three radial clearances; $\varepsilon = 0.8$

The governing equations, Eqs. (5. 6a-c), have certain similarities in structure with the Euler equations, which describe the flow of inviscid, compressible fluids. This is the reason that the occurrence of flow discontinuities is expected when the velocity is very high, which corresponds to shock waves in compressible supersonic flow. The average velocity in the Poiseuille flow, Eq. (5. 7a) shows that high values for the pressure driven circumferential velocity U are obtained when the pressure gradient in the x direction is important (high shaft speed and high eccentricity ratio), and also the fluid film thickness is large. Figure 5. 9 shows a comparison between the pressure distributions obtained without (Fig. 5. 9a) and with (Fig. 5. 9b) the inertial effects included. The shaft speed is

$\dot{n} = 350{,}000\,\text{rev/min} = 36{,}652\,\text{s}^{-1}$, the clearance $C = 100\,\mu m$, and the eccentricity ratio $\varepsilon = 0.8$, which correspond to the bearing and modified Reynolds numbers of $\Lambda = 1.223$ and $\text{Re}^* = 24.4$. Four cross sections through the pressure distributions are presented: at the symmetry plane and at three other equidistant axial locations. Also, the pressure distributions in the vicinity of the region of deceleration of the flow after the minimum film thickness are presented in more detail in Figs. 5. 9c and 5. 9d. The differences between the two flows are evident. Compared with the classic Reynolds equation, the inclusion of the inertial effects leads not only to a higher maximum pressure and a lower minimum pressure, but also to the occurrence of a discontinuity. It appears that the flow is accelerated too strongly in the negative pressure gradient region, and then it adapts to the periodic boundary conditions through a discontinuity. The surface plot of the pressure distribution including inertial effects is shown in Fig. 5. 10. The sharp discontinuity in the distribution of velocity *U* is visible in Fig. 5. 11.

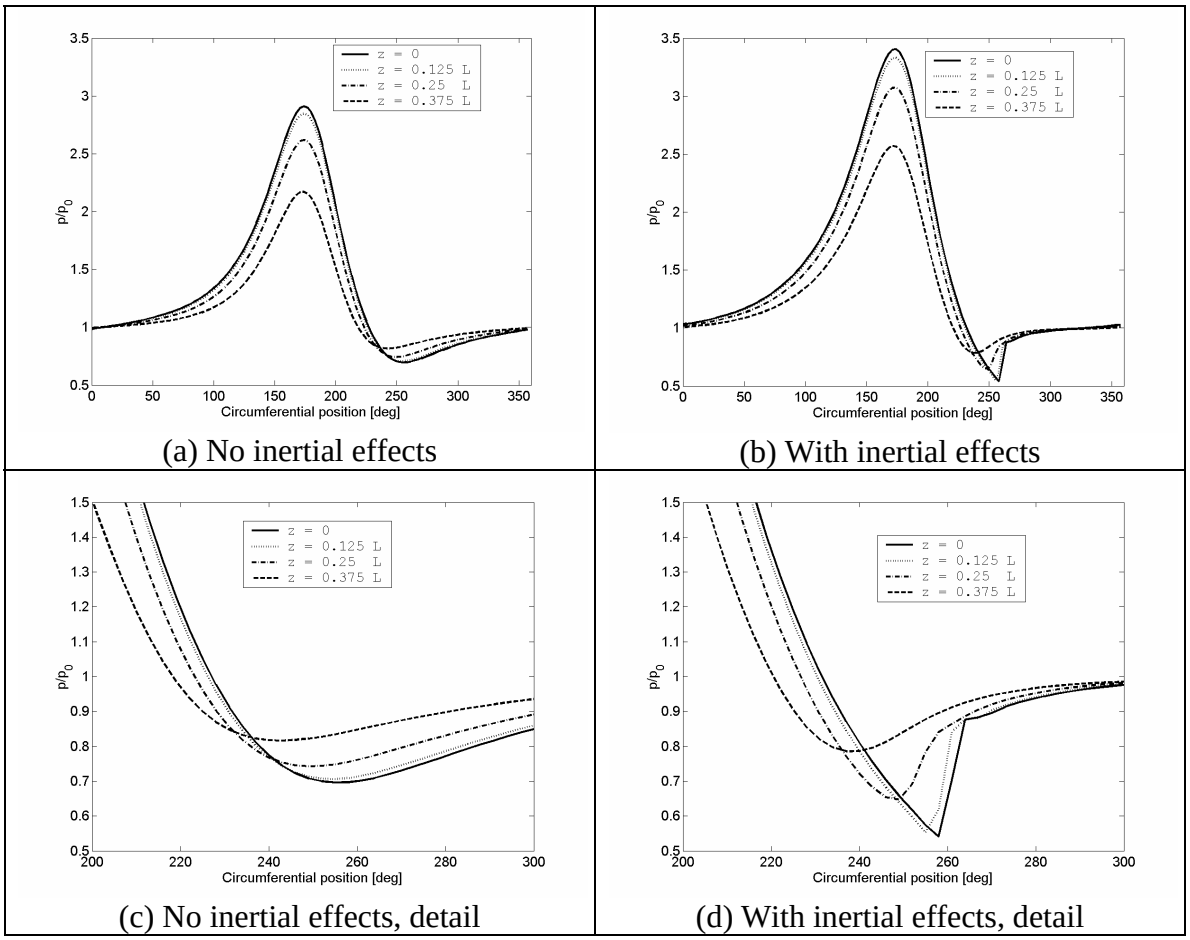

(a) No inertial effects

(b) With inertial effects

(c) No inertial effects, detail

(d) With inertial effects, detail

Fig. 5. 9 – Comparison between the pressure distributions with and without inertial effects vs. circumferential position for four axial positions;
$\Lambda = 1.223$, $\mathrm{Re}^* = 24.4$, $C = 100\,\mu m$, $\varepsilon = 0.8$, $\dot{n} = 350{,}000\,\mathrm{rev/min} = 36{,}652\,\mathrm{s}^{-1}$

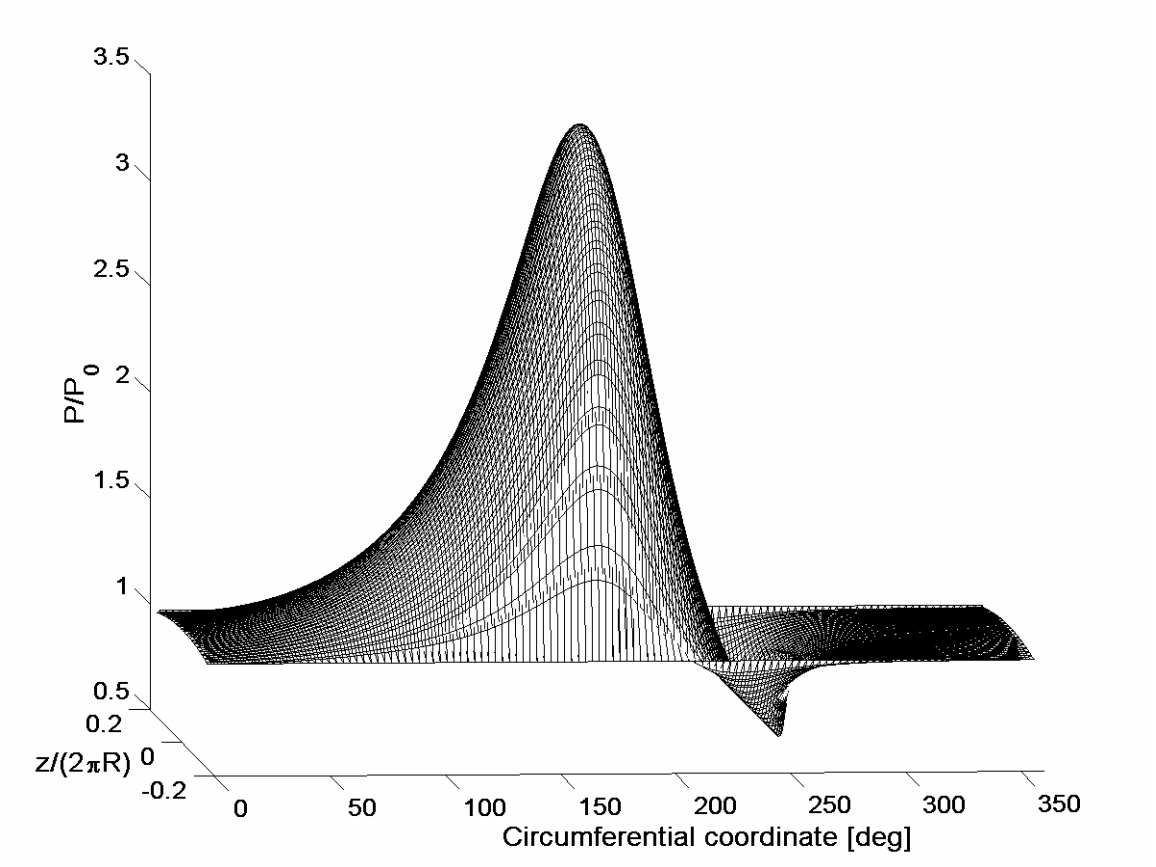

Fig. 5. 10 – Surface plot of the steady-state pressure distribution
$\Lambda = 1.223$, $\mathrm{Re}^* = 24.4$, $C = 100\mu m$, $\varepsilon = 0.8$, $\dot{n} = 350{,}000\,\mathrm{rev/min} = 36{,}652\,\mathrm{s}^{-1}$

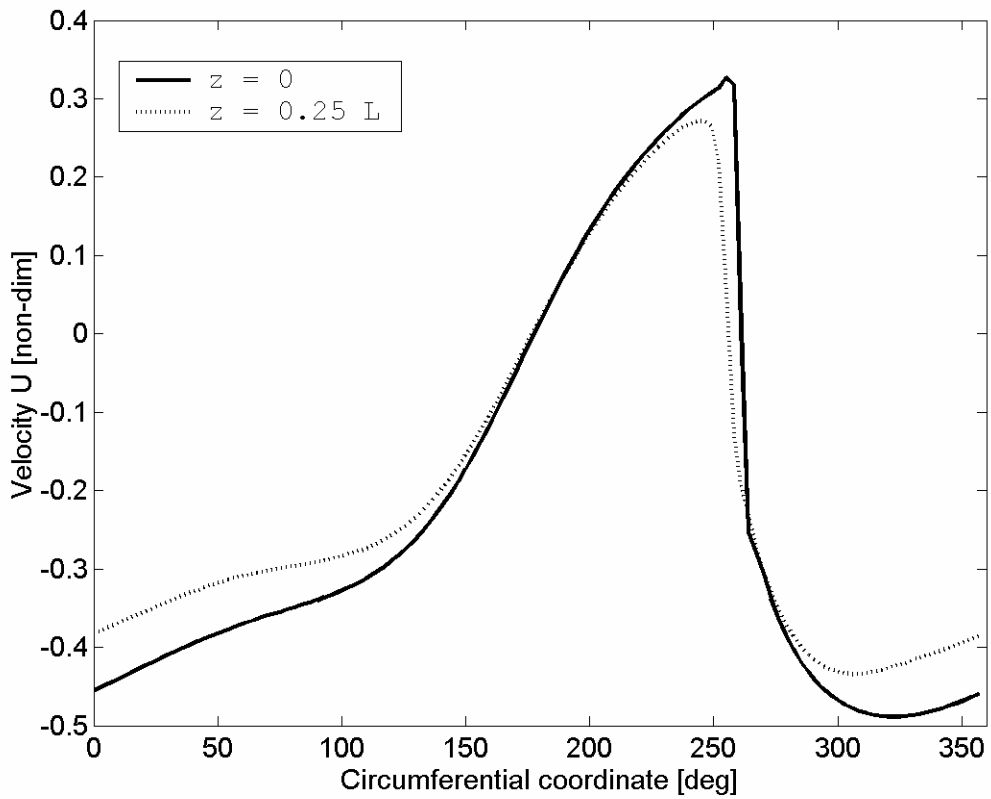

Fig. 5. 11 – Circumferential velocity distribution vs. circumferential coordinate; $C = 100\,\mu m$, $\varepsilon = 0.8$, $\dot{n} = 350{,}000\,\text{rev/min} = 36{,}652\,\text{s}^{-1}$

Flow discontinuities have been observed for the same bearing speed and clearance at eccentricities larger than $\varepsilon = 0.3$. For a lower value of the clearance, $C = 60\,\mu m$ and $\varepsilon = 0.8$, a flow discontinuity was detected starting at the speed $\dot{n} = 350{,}000\,\text{rev/min} = 36{,}652\,\text{s}^{-1}$ $\left(\text{Re}^* = 8.79, \Lambda = 3.40\right)$. When the clearance is even smaller, $C = 40\,\mu m$, no discontinuities were detected for speeds up to the maximum value considered (400,000 rev/min).

Chapter Six

Conclusions

This work is the first application of a relatively new numerical method, the space-time conservation element – solution element [Chang et. al., 1991] to flows in thin films. Therefore, this work is situated at the confluence between CFD and tribology, and is part of a long term ongoing research effort at the Department of Mechanical Engineering from the University of Toledo in this particular field.

The thesis has been structured into five main parts. After a brief introduction and motivation, in the second chapter the concept of fluid film bearings was presented, together with the formulation of the governing equations and correspondent boundary conditions. Gaseous cavitation and Elrod's formulation were also shown there, since they are used as a starting point (model) for the numerical formulation. The possibility of a flow discontinuity at the fluid film reformation front was presented and proven analytically.

Chapter Three started with a general presentation of the space-time conservation element / solution element method. Its main features, as shown in the literature by its original authors, were highlighted. The one-dimensional formulation of the method, as applied to cavitated fluid film bearings, was then presented in detail, both for uniform and

non-uniform grids. The results were compared with the results obtained using both Elrod's and type-differencing algorithms. The comparison shows that the CE/SE method, when contrasted to the previous numerical algorithms, has the ability to naturally predict the discontinuities that can appear at the film reformation boundary. The differences between the results obtained with the CE/SE method and with previous methods are significant when the position of the full film reformation point is not imposed through the boundary conditions.

The two-dimensional formulation applied to cavitated bearings was also described in detail in Chapter Three, followed by some representative results obtained for aligned and misaligned, both for journal and wave bearings. The results were compared with the results obtained using other numerical algorithms. The comparison showed that the CE/SE method, when contrasted to previous numerical algorithms, can successfully predict the pressure distribution within bearings, including cases with discontinuities in the lubricant film, without any special treatment. However, the computational time was higher than for the steady solvers, which can produce the results in seconds on modern personal computers, but it was comparable with other transient solvers (this statement is based on the comparison with a transient, type difference, code, which also uses the Elrod's formulation). The conclusion is that the method is a strong candidate to solve applications that require more precise results, such as accurate, robust computation of the cavitation boundaries, as well as to solve transient problems.

Chapter Four was dedicated to gas bearings. After a short introduction to describe some of the special features of gas bearings as contrasted to liquid bearings, the numerical formulation was presented, with emphasis on the differences relative to the

previous cases. The applications concentrated on the pressurized, or hybrid, bearings. Special consideration was given to the modeling of the supply system through the boundary conditions. Numerical results obtained for both non-pressurized and pressurized bearings were shown and compared to existing experimental and computed data. The results demonstrated the ability of the method to accurately predict the pressure distributions in such flows. However, using the standard Reynolds equation, no discontinuities were obtained. Therefore, compared with previous methods the CE/SE scheme does not bring any significant advantages in this particular case.

Chapter Five presented the application of a model to include the inertial forces in the governing equation of the flow in gas bearings. The Reynolds equation requires the solution of a single differential equation. The inclusion of the inertial effects, in the two dimensional space, adds two more equations that need to be solved simultaneously with the continuity equation. This fact added more complexity to the problem, including the possibility of the occurrence of flow discontinuities. The analytical and numerical formulations of the problem for this case were presented, followed by a comparison between the results obtained with and without inertial effects for a given geometry. The occurrence of flow discontinuities was also shown. Results demonstrated that the inclusion of inertial effects for the computation of the flow in gas bearings becomes necessary when the bearing speed is very high and/or the film clearance is large. Inclusion of inertial effects resulted in an increase of the predicted overall load capacity of the bearing, especially for high values of the clearance; the difference reached as much as 25% for the configuration studied. The bearing attitude angle was found to be less sensitive to this influence. At high speeds and relatively high clearances, flow

discontinuities can occur, similar to shock waves in supersonic flows. Also for this case the space-time conservation element and solution element method is capable of capturing these discontinuities without any special treatment, and without introducing distortion and/or excessive dissipation into the solution.

Parts of this work have been published, [Cioc and Keith, 2002 and 2003], [Cioc, Dimofte, Keith, and Fleming, 2003], [Cioc, Dimofte, and Keith, 2003]. Another paper related to the inertial effects has been submitted and approved for publication in the STLE Tribology Transactions.

Three directions for which this work can be continued are briefly described as follows.

1) Improvements of the modeling of the supply system. The modeling used in this work, which is widely used today, considers the supply system flow one-dimensional, with the flow rate characterized by the pressure ratio across the supply hole and by one parameter, the discharge coefficient, C_D. This coefficient is calculated using a semi-empirical formula. No consideration is given to the relative motion between the shaft and bearing, and for a given geometry, the discharge coefficient is assumed constant for all flow rates. Some formulations that are aimed at correcting the value of C_D with the flow rate are sometimes used, but still the approach is empirical and yields mixed results. Efforts have been made to improve the modeling of the supply system [Braun and Dzodzo, 1997], but the problem is far from being satisfactorily solved, so that the solution it is both accurate and practically obtainable. The CE/SE method is a good candidate to be used to calculate this flow, especially since flow discontinuities can occur, as in the case of choked (supersonic) regimes.

2) Improvements of the modeling of the inertial flows. The methodology used is a good start towards a more accurate modeling that includes heat transfer and turbulence effects. These improvements can be made without fundamentally changing the general structure of the simplified model that has been used in this thesis.

3) Improvements related to the formulation of the numerical modeling. The CE/SE method is continuously evolving and adapting to the problems encountered in applications. One of the problems which has been recently addressed [Chang, 2003] is related to the excessive diffusivity of the scheme for low values of the Courant number. This problem is common to explicit numerical schemes. Excessive dissipation cannot be avoided when the velocity of the transmission of information (in the governing equation) changes between different regions of the computational domain, or when the grid contains elements with relatively large size disparities. Further research work is needed in order to incorporate some of these newer methodologies in the modeling of flows in thin fluid films.

References

A

Arghir, M., Frêne, J. (2001), "A Triangle Based Finite Volume Method for the Integration of Lubrication's Incompressible Bulk Flow Equations", *Transaction of ASME*, **123**, 1, pp. 118-124.

Ayasoufi, A., Keith, T.G. (2003), “Application of the Conservation Element and Solution Element Method in Numerical Modeling of Axisymmetric Heat Conduction with Melting and / or Freezing”, 6th ASME-JSME Thermal Engineering Joint Conference, March 16-20

B

Belforte, G., Raparelli, T., Viktorov, V. (1999), "Theoretical Investigation of Fluid Inertia Effects and Stability of Self-Acting Gas Journal Bearings", *Transactions of the ASME*, **121**, Oct., pp. 836-843.

Bird, B.R., Stewart, W.E., Lightfoot, E.N. (1960) “Transport Phenomena”, John Wiley & Sons, Inc., New York, pp. 34-122.

Bonneau, D., Huitric, J., Tournerie, B. (1993), “Finite Element Analysis of Grooved Gas Thrust Bearings and Grooved Gas Face Seals”, *ASME Journal of Tribology*, **115**, pp. 348-354

Braun, M.J., Dzodzo, M.B. (1997) “Three-Dimensional Flow and Pressure Patterns in a Hydrostatic Journal Bearing Pocket”, *Journal of Tribology*, **119**, pp. 711-719.

C

Canuto, C., Hussaini, M.Y., Quarteroni , A., Zang, T.A. (1988), “Spectral Method in Fluid Dynamics”, Springer Verlag, New York.

Castelli, V., Pirvics, J. (1968), “Review of Numerical Methods in Gas Bearing Film Analysis”, J. of Lubrication Technology, *Trans. of ASME*, **90**, October, pp. 777-792.

Chang, S.C., To, W.M. (1991), “A New Numerical Framework for Solving Conservation Laws – The Method of Space-Time Conservation Element and Solution Element”, NASA TM **104495**, NASA, Cleveland, OH.

Chang, S.C., Loh, C.Y., Yu, S.T., Himansu, A., Wang, X.Y., Jorgenson, P.C.E. (1997), “Robust and Simple Non-Reflecting Boundary Conditions for the Space-Time Conservation Element and Solution Element Method”, AIAA Paper, No. **97-2077**, pp. 1172-1205.

Chang, S.C., Wang, X.Y., Chow, C.Y. (1998), “The Space–Time Conservation Element and Solution Element Method—A New High–Resolution and Genuinely Multidimensional Paradigm for Solving Conservation Laws I. The Two Dimensional Time Marching Schemes”, NASA TM – **1998-208843**, pp. 1-124.

Chang, S.C., Wang, X.Y., Chow, C.Y. (1998), “The Space–Time Conservation Element and Solution Element Method—A New High–Resolution and Genuinely Multidimensional Paradigm for Solving Conservation Laws I. Numerical

Simulation of Shock Waves and Contact Discontinuities", NASA/TM – 1998-**208844**, pp. 1-61.

Chang, S.C., Wang, X.Y., Chow, C.Y., (1999), "The Space-Time Conservation Element and Solution Element Method –A New High-Resolution and Genuinely Multidimensional Paradigm for Solving Conservation Laws", *Journal of Computation Physics*, **156**, pp. 89-136

Chang, S.C., Wu, Y., Wang, X.Y., Yang, V. (2000), "Local Mesh refinement in the Space-Time CE/SE Method", NASA TM-**2000-210516**

Chang, S.C., Zhang, Z.C., Yu, S.T.J., Jorgenson, P.C.E. (2000), "A Unified Wall Boundary Treatment for Viscous and Inviscid Flows in the CE/SE Method", NASA TM-**2000-210517.**

Chang, I.S. (2002-1), "Unsteady-State Rocket Nozzle Flows", AIAA 2**002-3884**

Chang, I.S. (2002-2), "Unsteady-State Underexpanded Jet Flows", AIAA 2**002-3885**

Chang, S.C. (2002-3), "Courant Number Insensitive CE/SE Schemes", AIAA 2**002-3890**.

Chang, S.C., Himansu, A., Loh, C.Y., Wang, X.Y., Yu, S.T. (2003), "Robust and Simple Non-Reflecting Boundary Conditions for the Euler Equations -A New Approach Based on the Space-Time CE/SE Method", NASA/TM—**2003-212495**.

Chang, S.C., Wang, X.Y. (2003), "Multi-dimensional Courant Number Insensitive CE/SE Euler Solvers for Applications Involving Highly Non-uniform Meshes", AIAA Paper **2003-5285**, presented at the 39th AIAA/ASME/SAE/ASEE Joint Propulsion Conference and Exhibit, July 20-23, Huntsville, AL.

Childs, D. (1993), "Turbomachinery Rotordynamics", John Wiley & Sons Inc., New York.

Childs, D.W. (1991), "Fluid-Structure Interaction Forces at Pump-Impeller-Shroud Surfaces for axial Vibration Analysis", *Trans. of the ASME*, **113**, 1, pp. 108-115

Cioc, C., Cioc, S., Kahraman, A., Keith, T.G., Moraru, L., (2002) “A Deterministic Elastohydrodynamic Lubrication Model of High-Speed Transmission Components", *STLE Tribology Transactions*, **45**, 4, pp. 556-562.

Cioc, S., Keith, T.G. (2002), “Application of the CE/SE Method to One-Dimensional Flow in Fluid Film Bearings”, *STLE Tribology Transactions*, **45**, pp. 167-176.

Cioc, S., Keith, T.G., (2003) "Application of the CE/SE method to Two-Dimensional Flow in Fluid Film Bearings", *International Journal of Numerical Methods for Heat & Fluid Flow*, vol. **13**, no. 2, pp. 216 - 243.

Cioc, S., Dimofte, F., Keith, T.G., Fleming, D.P., (2003), "Computation of Pressurized Gas Bearings Using the CE/SE Method", *STLE Tribology Transactions*, Vol. **46**, 1, pp. 128-133.

Cioc, S., Dimofte, F., Keith, T.G., (2003), "Application of the CE/SE Method to Wave Journal Bearings", *STLE Tribology Transactions*, Vol. **46**, 2, pp. 179-186.

Constantinescu, V.N. (1969), “Gas Lubrication”, American Society of Mechanical Engineers, Ed. Robert L. Wehe, New York.

Constantinescu, V.N., and Galetuse, S. (1982), “Operating Characteristics of Journal Bearing in Turbulent Inertial Flow”, *Journal of Lubrication Technology*, *Trans. of the ASME*, Vol. **104**, 2, pp. 173-179.

Constantinescu, V.N., 1995, “Laminar Viscous Flow”, Springer, New York, pp. 279-280, 403-417.

Cooper, S.A. (1961), "An Assessment of the Value of Theory in Predicting Gas Bearings Performance", *Trans. of the ASME*, Series D, J. of Basic Engineering, **83**, 2, pp. 195-200.

Czolczynski, K., "Rotordynamics of Gas-Lubricated Journal Bearing Systems", *Springer Pub*. pp. 11-67

D

Dai, R.X., Dong, Q., and Szeri, A.Z. (1992), "Bifurcation and Stability of Flow Between Eccentric Cylinders", Int. Journal of Eng. Science, Vol. **30**, 10, pp. 1323-1340.

Dimofte, F., Proctor, M.P., Fleming, D.P., Keith, T.G. (2000), "Wave Fluid Bearing Tests for an Aviation Gearbox", NASA TM-**2000-209766**

Dimofte, F. (1995), "Wave Journal Bearing with Compressible Lubricant – Part I: The Wave Bearing Concept and a Comparison to the Plain Circular Bearing", *STLE Tribology Transactions*, **38**, pp. 153-160

Dimofte, F. (1995), "Wave Journal Bearing with Compressible Lubricant – Part II: A Comparison of the Wave Bearing with a Wave-Groove Bearing and a Lobe Bearing", *STLE Tribology Transactions*, **38**, pp. 364-372.

E

Elrod, H.G. (1981), "A Cavitation Algorithm", *ASME J. of Lubr. Tech.*, **103**, 3, pp 350-354.

Elrod, H.G. and Ng, C.W. (1967), "A Theory for Turbulent Films and Its Application to Bearings", *ASME Trans.*, **89**, pp. 347-362.

F

Faria, M.T.C., Andres, L.S. (2000), “On the Numerical Modeling of High-Speed Hydrodynamic Gas Bearings”, *ASME Journal of Tribology*, **122**, pp. 124-130

Faria, M.T.C. (2001), “Some Performance Characteristics of High Speed Gas Lubicated Harringbone Groove Journal Bearings”, *JSME International Journal*, **44**, pp.775-781.

Ferziger, J.H., Perić, M., (1999) “Computational Methods for Fluid Dynamics”, Second Edition, Springer-Verlag Berlin Heidelberg.

Frêne, J., Nicolas, D., Degueurce, B., Godet, M. (1997), "Hydrodynamic Lubrication: Bearings and Thrust Bearings", Elsevier, Amsterdam, New York.

Fuller, D.D., (1984), "Theory and Practice of Lubrication for Engineers", Second Edition, A Wiley-Interscience Publication, John Wiley and Sons, New York.

G

Gero, L.R., McC.Ettles, C.M. (1985), "An Evaluation of Finite difference and Finite Element Methods for the Solution of the Reynolds Equation", *ASLE Transactions*, **29**, 2, pp. 166-172.

Groper, M., Etsion, I., (2001), "The Effect of Shear Flow and Dissolved Gas Diffusion on the Cavitation in a Submerged Journal Bearing", *ASME Journal of Tribology*, Vol. **123**, 3 (July), pp. 494-500.

Gross, W.A., Matsch, L.A., Castelli, V., Eshel, A., Vohr, J.H., Wildmann, M., (1980), "Fluid Film Lubrication", A Wiley-Interscience Publication, John Wiley and Sons, New York.

Guo, Y., Hsu, A.T. (2000), “Extension of the CE/SE Method to 2D Viscous Flows”, AIAA **2000-3385**, pp. 1-8.

H

Himansu, A., Jorgensen, P.C.E., Wang, X.Y., Chang, S.C. (2000), “Parallel CE/SE Computations via Domain Decomposition”, NASA/TM-2000-210480, pp. 1-11.

Hirs, G.G. (1974), “A Systematic Study of Turbulent Film Flow”, *ASME Trans.*, Ser. F, **96**, pp. 118-126.

I

Im, K.S., Yu, S.T. (2002), “Simulation of Direct Initiation of Detonation Using Realistic Finite-Rate Models”, AIAA 2**002-3886**.

J

Jakobsson, B., Floberg, L. (1957), "The Finite Journal Bearing Considering Vaporization", Transactions of Chalmers University of Technology, Gothenburg, Sweden, 190.

Jang, G.H., Chang, D.I. (2000), "Analysis of a Hydrodynamic Herringbone Grooved Journal Bearing Considering Cavitation", *ASME Journal of Tribology*, vol. **122,** 1, pp. 103-109.

Jorgenson, P.C.E., Loh, C.Y. (2002), "Computation Axisymmetric Jet Screech Tones using Unstructured Grids", AIAA 2**002-3889,** pp. 1-11

K

Kazimierski, Z., Trojnarski, J. (1980), "Investigations of Externally Pressurized Gas Bearings with Different Feeding Systems", *ASME Journal of Lubrication Technology*, **102**, pp. 59-64

Kim, C.K., Im, K.S., Yu, S.T. (2002), "Numerical Simulation of the Unsteady Flows in a Scramjet Engine by CESE Method", AIAA 2**002-3887**, pp. 1-13.

Kim, E., and Szeri, A.Z. (1997), "On the Combined Effects of Lubricant Inertia and Viscous Dissipation in Long Bearings", *Journal of Tribology, Trans. of the ASME*, Vol. **119**, 1, pp. 76-84.

L

Liu, N.S., Chen, K.H. (2001), "An Alternative Flow Solver for the NCC – The Flux Code and its Algorithm", AIAA **2001-0973**, pp. 1-17

Lund, J.W. (1964), "The Hydrostatic Gas Journal Bearing with Journal Rotation and Vibration", *ASME Journal of Lubrication Technology*, pp. 328-336.

Lund, J.W. (1967), "A Theoretical Analysis of Whirl Instability and Pneumatic Hammer for a Rigid Rotor in Pressurized Gas Journal Bearings", *ASME Journal of Lubrication Technology*, pp. 154-166.

Lund, J.W. (1968), "Calculation of Stiffness and Damping Properties of Gas Bearings", *ASME Journal of Lubrication Technology*, pp. 793-803

Lund, J.W. (1987), "Review of the Concept of Dynamic Coefficients for Fluid Film Journal Bearings", *Transactions of the ASME, Journal of Tribology*, Vol. **109**, pp. 37-41.

M

Mistry, K., Biswas, S., Athre, K. (1997), “A New Theoretical Model for Analysis of the Fluid Film in the Cavitation Zone of a Journal Bearing”, *ASME Journal of Tribology*, **119**, pp. 741-746.

Moraru L., Keith T.G., Dimofte F., Cioc S., Fleming D.P. (2003), “Dynamic Modeling of a Dual Clearance Squeeze Film Damper - Part I: Test rig and Dynamic Model with one Damper”, *Lubrication Engineering*, **59**, 8, pp. 16-24.

N

Ng, C.W. and Pan, C.H.T. (1965), “A linearized Turbulent Lubrication Model”, *ASME Trans.*, **87**, pp. 675-688.

O

Olsson, K.O. (1965), "Cavitation in Dynamically Loaded Bearings", Transactions of Chalmers University of Technology, Gothenburg, Sweden, 308.

P

Pan, C.H.T. (1990), “Gas Lubrication (1915-1990)”, Achievements in Tribology: on the 75th Anniversary of the *ASME Research Committee on Tribology*, Trib-Vol.**1**, pp. 31-55.

Pink, E.G. (1976), “An Experimental Investigation of Externally Pressurized Gas Journal Bearings and Comparison with Design Method Predictions”, 7th Internal Gas Bearing Symposium, July 13-15, pp. G3/41-59

Pink, E.G. and Stout, K.J. (1981), "Characteristics of Orifice Compensated Hybrid Journal Bearings", 8th International Gas Bearing Simposium, April 8-10, Leicester Polytechnic, BHRA Fluid Engineering, Cranfield, Bedford, U.K., pp. 29-44.

Pinkus, O., Sternlicht, B. (1961), "Theory of Hydrodynamic Lubrication", McGraw-Hill Book Company, New York, Toronto, London.

Q

Qin, J.R., Yu, S.T.J., Zhang, Z.C., Lai, M.C. (2001), “Simulation of the Cavitating Flows by the Space-Time CE/SE Method”, Eleventh International Multidimensional Engine Modeling User’s Group Meeting, Detroit, MI, http://www.erc.wisc.edu/multi_dimensional/ModelingMtng2001/Yu_Lai.pdf

R

Reynolds, O. (1886), “On the Theory of Lubrication and its Application to Mr. Beauchamp Tower’s Experiment Including an Experimental Determination of the Viscosity of Olive Oil”, *Philosophical Transactions of the Royal Society*, A, 177,

pp. 157-234; reprinted in *Fluid Film Lubrication*: A Century of Progress, Ed. Rhode, S.M., ASME publication, 1983.

Rozeanu, L., Tipei, N. (1980), “Slippage Phenomena at the Interface Between the Adsorbed Layer and the Bulk of the Lubricant: Theory and Experiment”, *Wear*, **64**, pp. 245-257.

S

Sestieri, A., and Piva, R. (1982), “The Influence of Fluid Inertia in Unsteady Lubrication Films”, *Journal of Lubrication Technology, Trans. of the ASME*, Vol. **104**, 2, pp. 180-186.

Shyu, S.H., Talmage, G., Carpino, M. (2000), “Comparison of Lubrication Models for Plane Slider Bearings”, *STLE Tribology Transactions*, **43**, 1, pp. 74-81.

Shyu, S.H., Jeng, Y.R. (2002), “An Efficient General Fluid-Film Lubrication Model for Plane Slider Bearings”, *STLE Tribology Transactions*, **45**, 2, pp. 161-168.

Szeri, A.Z., and Al-Sharif, A. (1995), “Flow Between Finite Steady Rotating Eccentric Cylinders”, *Theoretical and Computational Fluid Dynamics*, Vol. **7**, 1, pp. 1-28.

Szeri, A.Z. (1998), "Fluid Film Lubrication : Theory and Design", Cambridge University Press, Cambridge.

T

Tannehill, J.C., Anderson, D.A., Pletcher, R.H., (1997), "Computational Fluid Mechanics and Heat Transfer", Second Edition, Taylor & Francis

Tipei, N. (1980), “Slippage Phenomena at the Interface between the Adsorbed Layer and the Bulk of the Lubricant: Theory and Experiment”, *Wear*, **64**, pp. 245-257.

V

Vaidyanathan K., Keith T.G. (1991), “Performance-Characteristics of Cavitated Noncircular Journal Bearings in the Turbulent-Flow Regime”, *STLE Tribology Transactions*, **34**, 1, pp. 35-44.

Vijayaraghavan, D. (1989), “New Concepts in Numerical Prediction of Cavitation in Bearings”, Ph. D. Dissertation, The University of Toledo, Toledo, OH.

Vijayaraghavan, D., Keith, T.G., (1989), "Development and Evaluation of a Cavitation Algorithm", *STLE Tribology Transactions*, **32**, 2, pp. 225-233.

Vijayaraghavan, D., Keith, T.G. Jr., Brewe, D.E. (1990), “Extension of Transonic Flow Computational Concepts in the Analysis of Cavitated Bearings”, NASA TM-**103214**, NASA, Cleveland, OH.

Vijayaraghavan D., Keith T.G., Brewe D.E. (1996), “Effect of lubricant supply starvation on the thermohydrodynamic performance of a journal bearing”, *STLE Tribology Transactions*, **39**, 3, pp. 645-653.

W

Wang P., Keith T.G., Vaidyanathan K. (2001), “Non-Newtonian Effects on the Performance of Dynamically Loaded Elliptical Journal Bearings Using a Mass-Conserving Finite Element Cavitation Algorithm”, *STLE Tribology Transactions*, **44**, 4, pp. 533-542.

Wang P., Keith T.G., Vaidyanathan K. (2002), “Combined Surface Roughness Pattern and Non-Newtonian Effects on the Performance of Dynamically Loaded Journal Bearings”, *STLE Tribology Transactions*, **45**, 1, pp. 1-10.

Wang, X.Y., Chow, C.Y., Chang, S.C., (1998), “The Space-Time Conservation Element and Solution Element Method –A New High-Resolution and Genuinely Multidimensional Paradigm for Solving Conservation Laws, Part II. Numerical Simulation of Shock Waves and Contact Discontinuities” NASA **TM-1998-208844**

Wang, X.Y., Chow, C.Y., Chang, S.C., (1999), “Application of the Space-Time Conservation Element and Solution Element to One-Dimensional Advection-Diffusion Problems”, NASA TM-**1999-209068**.

Wang, X.Y., Chang, S.C., Jorgenson, P.C.E. (2000) “Prediction of Sound Waves Propagating Through a Nozzle Without/With a Shock Wave Using the Space-Time CE/SE Method”, NASA TM – **2000-209937**.

Wang, X.Y., Chang, S.C., Jorgenson, P.C.E. (2000) “Accuracy Study of the Space-Time CE/SE Method for Computational Aeroacoustics Problems Involving Shock Waves”, AIAA Paper **2000-0474**.

Wilde, D.A., San Andrés, L., (2003), "Comparison of Rotordynamic Analysis Predictions with the Test Response of Simple Gas Hybrid Bearings for Oil Free Turbomachinery", *Proc. of ASME Turbo Expo 2003 Power for Land, Sea and Air, June 16-19, 2003*, GT-2003-38859, Atlanta, GA

Wu, L., Bogy, D.B. (2001), “Numerical Simulation of the Slider Air Bearing Problem of Hard Disk Drives by Two Multidimensional Upwind Residual Distribution

Schemes over Unstructured Triangular Meshes", *Journal of Computational Physics*, **172**, pp. 640-657

Y

Yang, D., Yu, S., Zhao, J. (2001), "Convergence and Error Bound Analysis for the Space-Time CESE Method", *Numerical Methods Partial Differential Eqs.*, **17**, pp. 64-78.

Yang Q.M., Keith T.G. (1996-1), "Two-dimensional Piston Ring Lubrication. Part 1. Rigid Ring and Liner Solution", *STLE Tribology Transactions*, **39**, 4, pp. 757-768.

Yang Q.M., Keith T.G. (1996-2), "Two-dimensional Piston Ring Lubrication. Part 2. Elastic Ring Consideration", *STLE Tribology Transactions*, **39**, 4, pp. 870-880.

You, H.I., and Lu, S.S. (1988), "The Effect of Fluid Inertia on the Operating Characteristics of a Journal Bearing", *Journal of Tribology, Transactions of the ASME*, Vol. **110**, 3, pp. 499-502.

Yu Q.L., Keith T.G. (1995), "Prediction of Cavitation in Journal Bearings Using a Boundary-Element Method", *Journal of Tribology*, **117**, 3, pp. 411-421.

Yu, S.T., Chang, S.C. (1997), "Treatments of Stiff Source Terms in Conservation Laws by the Method of Space-Time Conservation Element and Solution Element", AIAA **97-0435**.

Yu, S.T., Chang, S.C. (1997), "Application of the Space-Time Conservation Element / Solution Element Method to Unsteady Chemically Reactive Flows", AIAA Paper **97-2099**.

Z

Zhang, Z.C., Yu, S.T.J., He, H., Chang,S.C. (2001) “Direct Calculations of Two- and Three-Dimensional Detonations by n Extented CE/SE Method”, AIAA **2001-0476**, pp. 1-9

Zhang, Z.C., Yu, S.T.J. (2001), “A Generalized Space-Time CE/SE Method for the Euler Equations on Quadrilateral and Hexagonal Meshes”, AIAA 2001-2592, pp. 1-11.

Zhang, M., Lin, H., Yu, S.T.J., Chang, S.C., Blankson, I. (2002), “Application of the Space-Time Conservation Element and Solution Element Method to the Ideal Magnetohydrodynamic equation”, AIAA **2002-3888**, pp. 1-17.

Zhang, Z.C., Yu, S.T.J., Chang, S.C. (2002) “A Space-Time Conservation Element and Solution Element Method for Solving the Two- and Three-Dimensional Unsteady Euler Equations Using Quadrilateral and Hexahedral Meshes”, Journal of Computational Physics, 175, pp. 168–199.